NOVEL ALUMINUM ALLOYS CONTAINING CERIUM AND LANTHANUM

PHYSICAL METALLURGY AND THERMODYNAMICS OF ALUMINUM ALLOYS CONTAINING CERIUM AND LANTHANUM

By

MEHDI HOSSEINIFAR

B.Sc.

Sharif University of Technology, Tehran, Iran, 2001

M.Sc.

Sharif University of Technology, Tehran, Iran, 2004

A Thesis

Submitted to the School of Graduate Studies

in partial fulfillment of the requirements

for the degree

Doctor of Philosophy

McMaster University

DOCTOR OF PHILOSOPHY (2009)
(Material Science and Engineering)

MCMASTER UNIVERSITY
Hamilton, Ontario, Canada

TITLE: **Physical Metallurgy and Thermodynamics of Aluminum Alloys Containing Cerium and Lanthanum**

AUTHOR: **Mehdi Hosseinifar**

B.Sc.

Sharif University of Technology

Tehran, Iran, 2001

M.Sc.

Sharif University of Technology

Tehran, Iran, 2004

SUPERVISOR: **Dr. Dmitri V. Malakhov**

NUMBER OF PAGES: xvi, 184.

Abstract

The development of highly formable aluminum alloy sheets is of great interest to the automotive industry, because they provide a lightweight alternative to steel sheet for structural panels. Finding ways to improve the formability of Al alloys is the main subject of the present investigation. This issue is tackled from two angles. First, a possibility of fabricating a two-phase material containing newly discovered ductile intermetallic compounds is considered. The Al-La-Mg system is thermodynamically optimized accompanied with a differential thermal analysis (DTA) experiment to validate the optimization results. A new approach is introduced to deal with the incompatibility of phase models in binary Al-La and La-Mg systems. This approach is successfully applied to the Laves and B2 phases in the binary La-Mg system. A utilization of the thermodynamic description of the Al-La-Mg system to model solidification at low and high cooling rates shows that it is impossible to fabricate such a two-phase material by casting.

Second, the effect of small additions of cerium and lanthanum on Fe-bearing intermetallics in a wrought heat-treatable Al alloy is examined. Fe-containing intermetallics are known to deteriorate the formability of Al alloys by acting as void nucleation sites. It is found that in alloys containing 0.1-0.2 wt. % of lanthanum, the fraction of less harmful Chinese script particles is pronouncedly higher than that in the reference alloy. In addition to this advantage, much smaller grains are seen in the alloy with 0.2 wt. % La. Despite similarities between La and Ce, the latter metal neither

modifies the microstructure nor noticeably affects the grain size. Hot rolling and solutionizing nullifies the beneficial effect of small La additions resulting in no improvement in the formability of the alloy.

In order to understand how lanthanum affects the phase portrait of the alloy, a so-called direct thermal analysis experiment is performed. Solidification paths are derived for slowly cooled alloys by coupling the results of this investigation with microstructural observations. The likelihood of two modification mechanisms is speculated using these solidification paths.

Acknowledgements

First and foremost, I would like to thank my supervisor Dr. Dmitri V. Malakhov for giving me the opportunity to explore new scientific horizons. His support and guidance throughout the entire length of this work is greatly appreciated. I would also like to thank my supervisory committee members Professors Anthony Petric and Nikolas Provatas for their invaluable comments and suggestions.

Financial support of AUTO21 research initiative and in kind support of Novelis Inc. is greatly acknowledged.

A sincere appreciation goes to those who helped me perform various experimental investigations of this work: Mr. Ed McCaffery, Mr. John Rodda and Mr. Doug Culley from materials science department and Mr. Chris Butcher from BIMR for metallographic examinations, Dr. Steve Koprich for SEM analysis and Mr. Pierre Marois from Novelis Inc. for performing intermetallic phase extraction and XRD investigation.

Special thanks to the staff and fellow graduate students of materials science department who made my PhD studies at McMaster a pleasurable experience.

I wouldn't reach this height in my life without unconditional love and support of my parents. I owe a great deal to them. Finally, my deepest gratitude goes to my love Maryam for her patience and encouragements without which this thesis could not have been completed. This work is dedicated to her.

Table of contents

List of figures

1 Introduction

An increasing demand for weight reduction in automobiles has led to a growing interest in parts made from aluminum alloys. So far, most aluminum usage has come in the form of castings and forgings in transmissions, engine blocks, wheel rims, etc. Further significant weight reduction can be achieved if aluminum sheet replaces steel as the primary material in the body panels of the car (doors, hood, roof, etc.). 6xxx series aluminum alloys (wrought heat treatable Al-Mg-Si alloys) with a high strength/density ratio and a good corrosion resistance are an attractive alternative for steel in the production of outer body panels. This substitution is hindered mainly by a high cost of production of such components from aluminum alloys - aluminum sheets are approximately five times more expensive than steel ones.

A large percentage of this higher price comes from the cost of converting large cast ingots, traditionally prepared by direct chill (DC) casting, into aluminum sheets. In the commercial production of 6xxx series sheets, the material goes through a sequence shown in Figure 1-1. It starts with casting ingots which can be as large as $0.6\times2\times9$ m^3. Then ingots are homogenized, hot rolled and cold rolled to a prescribed thickness. Finally, sheets are annealed and sent out for final forming process such as stamping etc.

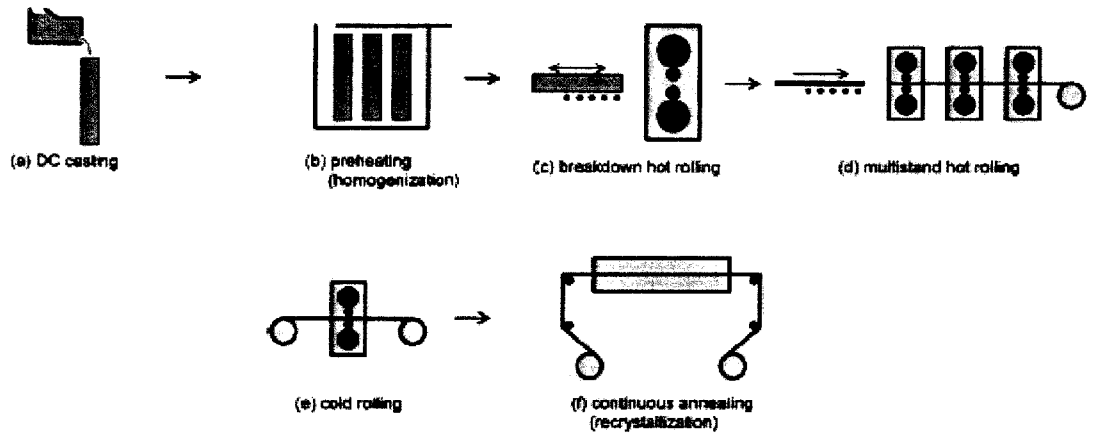

Figure 1-1 Schematic diagram illustrating the typical steps of thermo-mechanical processing of 6xxx series Al sheet alloys [Engler & Hirsch 2002]

The fabrication costs can be reduced if the DC casting is replaced by a near-net shape casting process such as strip casting (SC). Typically, SC produces plates with 6-15 mm thickness which need a dramatically less extensive thermo-mechanical processing (hot and cold rolling steps) to reach the final gauge. This translates into a reduced cost of production. On the other hand, by decreasing the extent of thermo-mechanical treatment, the benefits associated with this step will be diminished. The presence of brittle intermetallic particles containing iron is a major threat to the formability of Al alloys. These particles can induce damage and premature failure in a wide variety of forming and bending processes [Sarkar *et al.* 2000]. During thermo-mechanical processing of DC products, these intermetallics break, redistribute and some of them even dissolve into the matrix which effectively reduces their harmful effect. Since the rolling steps are cut off for SC products, the detrimental effect of Fe-containing particles is especially acute in these alloys [Lievre *et al.* 2003, Spencer *et al.* 2002].

Secondary Al is the main source of iron and with the ever increasing use of the recycled aluminum not only the presence of these intermetallics is unavoidable, but also a greater fraction of intermetallic particles must be dealt with. Since the modification of these particles by thermo-mechanical processes is not an operative in SC alloys, attempts must be focused on modifying them during the initial casting step. As an approach to do this, small amount additions of certain elements are investigated. Strontium is a well-studied example of such elements [Mulazimoglu *et al.* 1996, Paray *et al.* 1996, Shabestari *et al.* 1995, Samuel *et al.* 2001]. It is found that the addition of as low as 300 ppm of Sr to wrought and cast Al alloys favors the formation of a less harmful morphology of Fe-containing intermetallics. However, a high price of Sr restricts its usage in practice. Finding effective modifying elements with lower cost is of a great industrial interest. Ashtari *et al.* [2004, 2005] pursued this goal by adding lithium and potassium to an Al-Si-Fe-Cu cast alloy. Their results showed that these elements are less effective than Sr.

In the absence of an adequate theory on the modification mechanisms, a suitable modifying element may be found via an Edisonian approach. However, it is inadmissible to pick the element(s) randomly. Instead, promising candidates can be found by considering what they have done in other alloying systems. For instance, it is found in the literature that small additions of rare-earth metals (R metals) to magnesium alloys [Bakke *et al.* 2003, Pekguleryuz & Kaya *et al.* 2003], lead-free solders [Xia *et al.* 2002, Lawrence *et al.* 2002], iron aluminides [Morris *et al.* 2003, Salazar *et al.* 2003], and Fe-V-W-Mo alloys [Fu *et al.* 2005] enhanced the ductility of the alloys. Moreover, a beneficial effect of mischmetal (a mixture of R metals mainly composed of Ce and La)

addition on the ductility of cast Al alloys [Cao *et al.* 1990, Ravi *et al.* 2002] is reported. In these investigations, an improved ductility of the Al alloy is attributed to the formation of finer Fe-bearing intermetallic particles.

These findings render the R metals as promising candidates for the purpose of modification of intermetallics in wrought Al alloys. Among the seventeen members of the rare-earth metals family, the preference is given to cerium and lanthanum since they are the cheapest. Before engaging in a full fledged study of Ce and La additions to the commercial SC products, the modification effect of them has to be validated. The present investigation seeks to provide this validation by adding these elements to a heat-treatable alloy whose composition resembles 6xxx series alloys in a laboratory scale casting experiment.

Although the addition of Ce and La is considered from the view point of their effect on already existibg intermetallics in the system, a possibility of formation of new intermetallic particles containing Ce and La (*e. g.* aluminides) shall not be forgotten. While these new intermetallics, similar to almost all other intermetallics, are brittle and hence harmful to the formability, the situation is dramatically different if the newly formed intermetallic particles are ductile. Such ductile intermetallic phases are not fictional. In 2003, Gschneidner *et al.* [2003] introduced a family of R-bearing intermetallics which were relatively ductile. An aluminum alloy containing ductile intermetallics as the second phase may show extraordinary mechanical properties if both

phases maintain severe deformations simultaneously (co-deformation) [Sinclair *et al.* 1999].

In Chapter 2 a possibility of developing a new type of Al alloys containing Ce- or La-bearing ductile intermetallics is examined. Computational thermodynamics is employed to predict whether ductile intermetallics may form along with the FCC (Al) phase during casting. Chapters 3 and 4 deal with the small additions of Ce and La. In chapter 3, the effect of these elements on the microstructure and properties of a typical 6xxx series Al alloy is investigated, and in Chapter 4 it is attempted to clarify the mechanism of modification by these elements.

2 A two-phase Al alloy containing ductile intermetallics

2.1 A family of ductile intermetallics

In 2003, a discovery of a family of ductile intermetallic compounds was reported by Gschneidner *et al.* [2003]. This family encompasses binary stoichiometric compounds RM, where R is a rare-earth metal and M is a transitional metal or a metal belonging to a main group. These intermetallics have the BCC_B2 (CsCl type, $Pm\bar{3}m$) crystal structure (Figure 2-1). To have an idea about the ductility of these RM intermetallics, Gschneidner *et al.* [2003] measured that the fracture toughness (K_{IC}) of DyCu was 23-28 $MPa\sqrt{m}$ compared to 5-6 $MPa\sqrt{m}$ for NiAl intermetallic with the same B2 structure at the same condition. They also reported a high elongation at fracture of 27% at room temperature for YAg compound comparable to that of common commercial Al alloys.

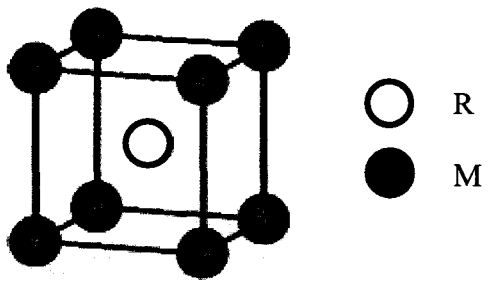

Figure 2-1 Schematic crystallographic structure of the RM ductile intermetallic phase

High ductility of intermetallic compounds at room temperature is not an unprecedented phenomenon. Several studies showed that special conditions such as non-stoichiometry, metastable disorder, doping or controlled atmosphere resulted in improved ductility of intermetallic compounds [Russell 2003]. However, none of these was required in the RM compounds. These intermetallics are fully ordered stoichiometric compounds without a third element addition and the tests mentioned earlier are carried out without protective atmosphere. The origin of the ductility of these intermetallics is still unknown and under investigation. However, Zhang *et al.* [2005] mentioned three factors that may contribute to the ductility of these compounds:

1. *Multiple slip systems*. The uniaxial tensile test was performed at room temperature on single crystal specimens of YAg [Russell *et al* 2004] and YCu [Russell *et al.* 2005]. The examination of slip lines on the faces of the specimens suggested that {110}<101> and {100}<010> were the active slip systems. On the contrary, TEM investigation using **g.b** = 0 out of contrast analysis (**b**: Burgers vector, **g**: operating reflection vector) of plastically deformed YAg specimens revealed that the majority of dislocations were having <111> Burgers vector with some having <011> Burgers vectors. The existence of multiple active slip systems in these alloys was explained by different dislocation reactions [Russell *et al* 2004].
2. *Fine grain size*. It is known that smaller grain size of an alloy increases the fracture toughness by minimizing dislocation pile-up [Dieter 1986, Hertzberg 1989]. The mean grain size of the DyCu compound specimens having

undergone a fracture toughness test was 0.2 μm [Zhang *et al.* 2005]. It must be mentioned that similar fine grains did not result in such a large increase in the fracture toughness of other intermetallic compounds.

3. *R metal contracting environmental embrittlement.* Hydrogen embrittlement is one of the primary causes of low ductility of intermetallic compounds. It is deemed that rare-earth metals reduce this phenomenon by forming oxides or hydrates at the grain boundary and therefore increase the grain boundary strength.

While a great deal of attention has been paid to these compounds as individual phases [Morris *et al.* 2004, Russell *et al.* 2004, Russell *et al.* 2005, Zhang *et al.* 2005, Xie *et al.* 2008, Wollmershauser *et al.* 2009], they were never considered as constituents capable of enhancing the mechanical properties (*e.g.* strength) of aluminum alloys. Moreover, no attempts were taken to fabricate such alloys. The research inactivity in this area is explainable. Compounds of aluminum with R metals are not members of the ductile RM family [Gschneidner *et al.* 2003], and as a result, a third metallic component such as Mg, Zn, or Cu, capable of forming RM compounds with most of the R metals, must be added. Although the affinity of Al for rare-earth metals is comparable to that of Mg, Cu, Zn and R metals, the concentration of aluminum is much greater. Consequently, it is very likely that the additions of rare-earth elements results in nothing but the formation of their aluminides. Moreover, since ternary Al-R-M systems are considered it is quite possible that instead of a two-phase material a multi-phase material is formed where other phases are not as ductile. This qualitative speculation however does not

prove that the formation of the desired Al/RM material is impossible. The present investigation attempts to clarify this issue quantitatively with the help of computational thermodynamics.

The formation of RM particles may require significant additions of R metals. While these metals are somewhat expensive, this approach can be economically feasible if the superior properties of these new Al alloys justifies the added cost. The situation where RM particles are dispersed within the FCC aluminum phase differs from the classical case of precipitation hardening seen in 2xxx and 6xxx series aluminum alloys. In fact, RM phase can hardly form as a result of an age hardening process since R metals have very low solubilities in solid aluminum even at high temperatures. The RM/FCC two-phase materials are also different from the case when particles of a hard phase are embedded in a ductile matrix. The ductility of RM phase is comparable to that of the aluminum matrix enabling it to "co-deform" with the matrix. Exceptionally high strengths, which are considerable fractions of the theoretical strength ($\mu/30$), are achieved in certain materials consisting of two deformable phases when they are drawn, extruded or rolled to high strains. The concept of co-deformation will be explained briefly as a promising mechanism of enhancing mechanical properties of Al alloys containing RM particles.

2.2 Co-deformation of two-phase materials

The stress-strain curve of two-phase materials has been associated with four different regions (Figure 2-2). First, both phases deform elastically resulting in a linear elastic response of the bulk material. Then, upon reaching a critical load, the softer phase deforms plastically. In this region, the slope of the stress-strain curve can be taken, as the first order, to be the elastic modulus of the harder phase weighted by the volume fraction of it. By increasing the load, the harder phase eventually deforms plastically (or fractures). If possible, further deformation constitutes plastic co-deformation of the two phases up to the point where final fracture occurs (considered as the fourth region).

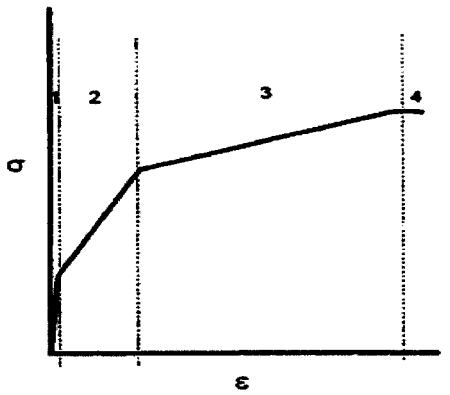

Figure 2-2 Schematic stress-strain curve for aggregated two-phase materials

The behavior illustrated in Figure 2-2 is usually described using the "rule-of-mixtures" estimate for a material's response which assumes (among other suppositions) that the strain in both phases is equal:

$$\sigma_c(\epsilon) = (1-f)\sigma_m(\epsilon) + f\sigma_p(\epsilon) \qquad 2\text{-}1$$

In this model, f is the volume fraction of the fiber and the subscripts "c", "m" and "p" refer to bulk two-phase material, matrix and second phase respectively. This equation predicts that the strength of the two-phase material will be something in between the strength of the softer and the harder phases.

Equation 2-1 satisfactorily predicts the strength of metal matrix composites reinforced by hard brittle particles such as SiC, alumina, or glass fibers, where the second phase particle does not deform plastically and the material fails at the end of stage three shown in Figure 2-2. However, the rule-of-mixtures does not apply when the second phase is a moderately ductile material and the fourth region in Figure 2-2 becomes viable. For example in the case of Cu-18.2vol%Nb drawn wires, ultimate tensile strengths (UTS) up to 2200 MPa have been achieved [Bevk *et al.* 1978] while the UTS of heavily deformed copper and niobium wires is ~450 and ~1100 MPa respectively. According to rule-of–mixtures, model the UTS of Cu-18.2vol%Nb should be ~580 MPa which is well below the experimental observations. Other common examples are wire drawn pearlitic steel [Embury & Fisher 1966] and Cu-Nb [Spitzig & Krotz 1988] where tensile strengths of 1.4 GPa or more is reached at high strains. A summary of strengths achieved for different co-deformed two-phase materials is shown in Table 2-1.

It should be mentioned that such high strains cannot be achieved in a uniaxial tensile test due to the geometrical instability in the form of necking inherent to it. To

avoid this limitation processes such as wire drawing, extrusion or rolling must be employed. These processes are not limited by a geometrical instability.

Table 2-1 Strength of selected heavily co-deformed two-phase materials [Sinclair 2001]

Material	UTS (MPa)	Drawing strain
Cu-15wt%Cr	906	7
Cu-18vol%V	1850	11
Cu-30vol%Fe	1500	8.5
Cu-20vol%Ta	1600	8.9
Cu-20vol%Nb	1400	6.9
Cu-60at%Ag	1350	9.3
Fe-Fe_3C	4000	3

Basic aspects of the co-deformation of FCC/BCC materials are reviewed by Sinclair *et al.* [1999]. α/β brasses and two-phase (ferrite–austenite) stainless steels are industrial examples of FCC/BCC materials. Slip transmission from one phase to another is the key to successful co-deformation and the FCC/BCC two-phase materials have been the subject of many investigations since these two phases are very well studied in terms of operating slip systems and dislocation structure and it is found that slip continuity is possible in FCC/BCC materials bearing Kurdjumov–Sachs orientation relationship. In the case of FCC/RM two-phase material, the RM intermetallics are characterized by the B2 crystal structure, whose active slip systems are different from those inherent to the FCC and BCC phase. It was mentioned that the RM phases are characterized by having

multiple slip system. The interaction of these slips systems with those of the FCC phase during slip transmission in the co-deformation process can be the subject of experimental and theoretical investigations.

Whether or not a two-phase RM/FCC structure maintains co-deformation and achieves high strengths deserves extensive experimental investigation. Nevertheless, the first task is to prepare such an alloy.

2.3 Alloy fabrication

Firstly let us specify the R and M elements that are going to be dealt with. For the R element, cerium and lanthanum are considered based on their lower price compared to other members of the rare-earth family. Mg, Cu, and Zn are common alloying elements in Al alloys which are indicated by Gschneidner *et al.* [2003] as M elements capable of forming ductile intermetallics. Copper is able to form RM compounds with many R metals but not with Ce and La. As a result Cu is eliminated. Between Mg and Zn, the preference is given to Mg because of its lower density and the fact that more phase diagram data is available in the literature for Mg-R and Al-Mg-R systems. The importance of this type of data will be explained later. In summary, Al-Ce-Mg and Al-La-Mg systems are considered in which the formation of CeMg and LaMg ductile intermetallics is intended.

Casting is a common step in the fabrication of all engineering materials. It would be the most convenient if the Al/RM material formed as a result of a casting process. Finding out whether the formation of the desired two-phase material during casting is feasible requires either an infinitely laborious experimental investigation on numerous alloys with systematically chosen compositions, or the availability of a thermodynamic database on multi-component Al alloys. A thermodynamic database consists of critically assessed analytical expressions of the Gibbs energies of all phases in the system written in a language which is comprehensible for a software capable of performing sophisticated thermodynamic calculations. Such a thermodynamic database can be employed to model the solidification of Al alloys to which varying amounts of M and R metals are added.

Firstly, let us consider the typical direct-chill casting technique. It is characterized by a low cooling rate. Only a few degrees of supercooling at the mold surface results in the heterogeneous nucleation of Al. The released heat due to the formation of these nuclei increases the temperature at the Al/melt interface to the equilibrium melting temperature of Al. This temperature is maintained at the interface during the growth of solid aluminum. Therefore, a local equilibrium can be assumed at the interface of solid/liquid. In this case, an analysis of solidification processes can be performed by invoking the Scheil-Gulliver method [Gulliver 1913, Scheil 1942].

The assumption of local equilibrium at the solid/liquid interface means that at any stage of the solidification solidifying phases and their compositions are governed by the equilibrium phase diagram. In the case of a binary system, this information can be

directly read from the phase diagram by drawing a tie-line at each temperature. In systems composed of three or more components, such analysis of solidification is impossible since the positions of the tie-lines are unknown unless the thermodynamic properties of phases in the system are known.

If analytical expressions of Gibbs energies of all phases in a multi-component system are available, the local equilibrium can be calculated by minimizing the Gibbs energy of the whole system. As a result, the equilibrium phases and their amounts at each temperature during cooling of the melt can be found. After finding the amount of solid phases at one temperature, the new amount and composition of the liquid will be calculated and used for computing equilibrium at a lower temperature. The complete solidification path of an alloy is derived by repeating this procedure until all the liquid is solidified.

The prediction of the Scheil-Gulliver method is an extreme in the sense that it assumes no diffusion in the solid phase. In the case of alloys containing fast diffusing elements (such as carbon in steels) a more realistic modeling of solidification can be achieved if the so called "back diffusion" of these elements in the solid phase is considered. The effect of back diffusion can be handled by solving diffusion equations analytically [Broady & Flemings 1966, Cyine & Kurz 1981] or numerically using commercial software (*e.g.* DICTRA [Anderson *et al.* 2002]). These calculations can be coupled with a thermodynamic database and the Scheil-Gulliver calculations to model solidification path of alloys prone to redistribution of elements in solid phases by back

diffusion. Such treatment has resulted in better modeling of solidification for steels [Hillert *et al.* 1999, Hallstedt *et al.* 2006] and nickel base superalloys [Tancret 2007, Walter *et al.* 2005]. However, this approach is questionable for Al alloys [Larouche 2007] since none of the common alloying elements of this system are considered to be fast diffusing elements.

There are several casting processes that are characterized with high cooling rates such as strip casting in which the cooling rate may reach 4000 K/s [Suzuki *et al.* 2005] compared to 10 K/s of direct chill casting. Such high cooling rates can result in the supercooling of the melt which translates to a supersaturated liquid. It is frequently seen that high cooling rates result in the formation of metastable phases rather than phases predicted by the equilibrium phase diagram or the Scheil-Gulliver method. This is extremely important since it provides the possibility of having the FCC/RM two-phase material fabricated even if the equilibrium phase diagram and Scheil-Gulliver method predict otherwise.

To justify the formation of metastable phases, Hillert [1999] argued that a higher chemical driving force for the "nucleation" of metastable phases favored their precipitation from a supersaturated melt or solid solution. Hillert's argument can be best explained if solid state precipitation in a hypothetical binary system shown in Figure 2-3a is considered. If an alloy with overall composition of x_0 is supercooled to the temperature T_1 then according to the phase diagram, β should precipitate from α. The driving force for the "complete" precipitation of the β phase is shown in Figure 2-3b by ΔG_m. This value is

always greater for a stable phase compared to that of a metastable phase. This term, however, is different than the driving force for the "onset" of precipitation which is shown as D^{β} on the graph. Hillert [1999] showed that at low supersaturations this driving force is directly proportional to the difference in composition between the parent and precipitating phase:

$$D^{\beta} = \left(x^{\beta} - x_{eq}^{\alpha}\right) \times \left(\frac{\partial^2 G^{\alpha}}{\partial x^2}\right)_{x_0} \times \left(x_0 - x_{eq}^{\alpha}\right) \qquad 2-2$$

This means that metastable phases can readily have higher driving forces for nucleation than stable phases. Such possibility is shown schematically for the metastable phase γ in Figure 2-3b where D^{γ} is noticeably higher than D^{β}.

Purdy *et al.* [2004] further examined this concept especially for the case where a solution phase is forming from the melt. They deduced that the driving force for the onset of precipitation is maximized for a composition of the solution phase where:

$$\left(\frac{\partial G^{S}}{\partial x^{S}}\right)_{x^{S}} = \left(\frac{\partial G^{L}}{\partial x^{L}}\right)_{x_0^{L}} \qquad 2\text{-}3$$

This is why a geometrical construction used for finding such a composition of precipitate is called "double tangent construction" (Figure 2-4).

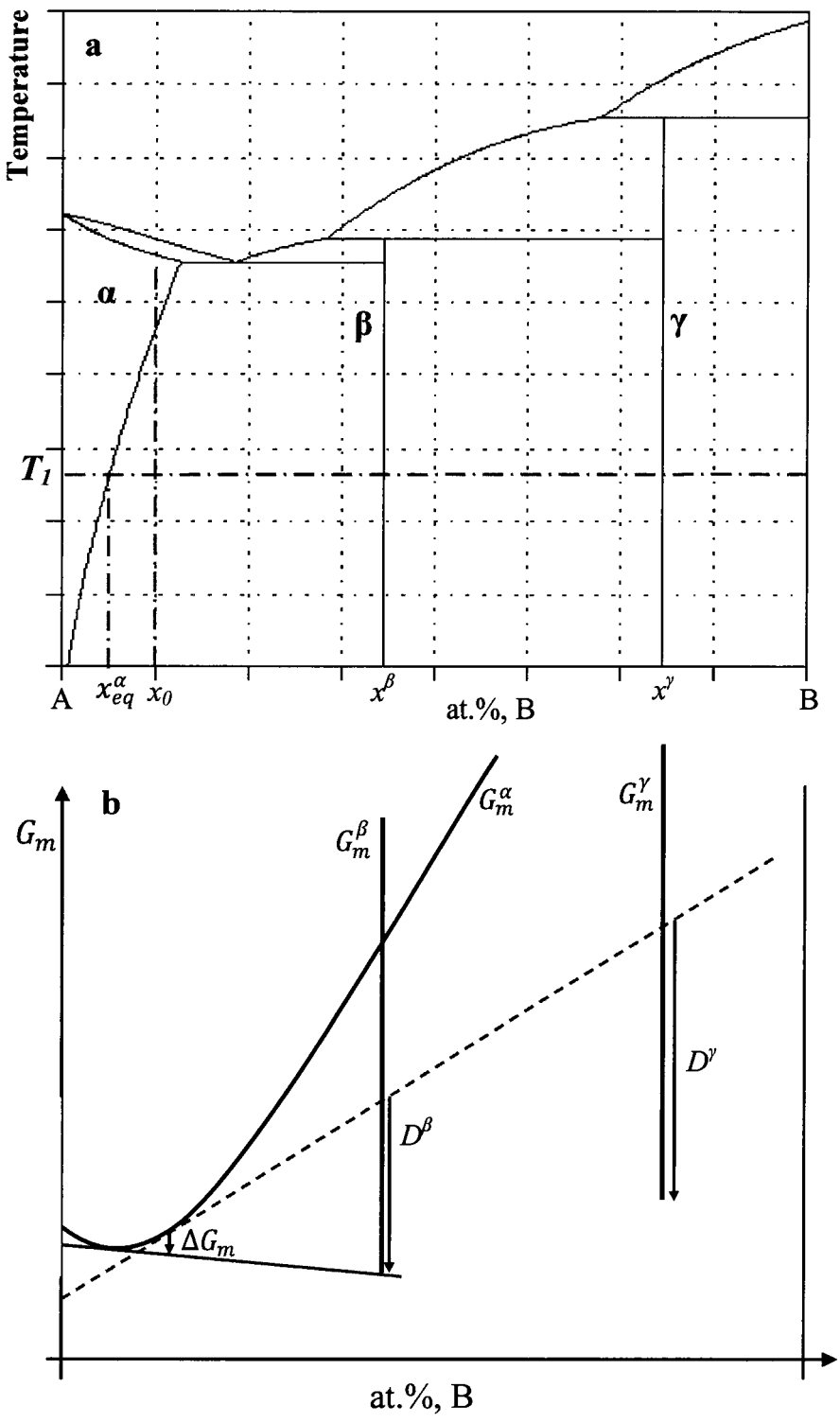

Figure 2-3 a) A hypothetical phase diagram and b) corresponding Gibbs energies of phases in (a) at T_1 and driving forces for the complete and onset of precipitation

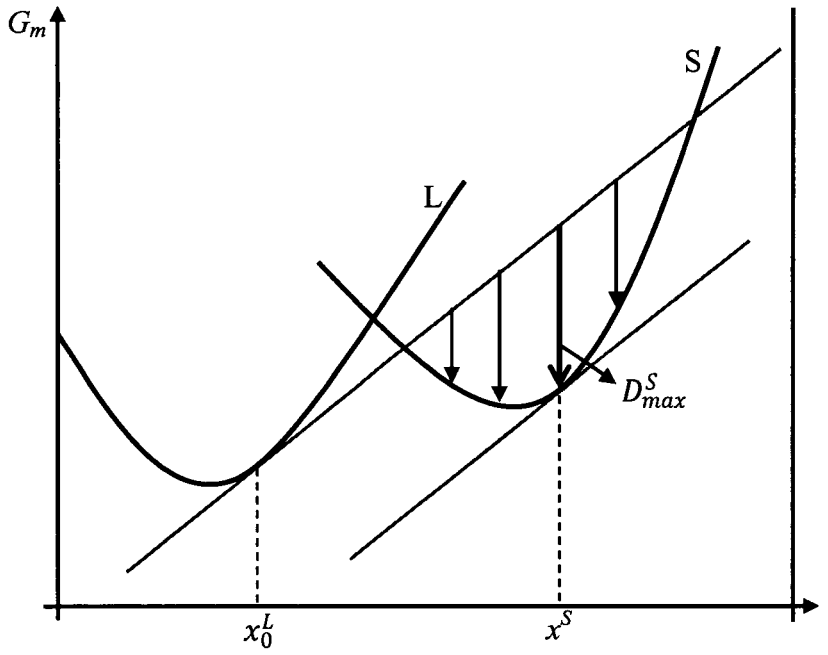

Figure 2-4 Double tangent construction for finding maximum driving force for the onset of precipitation of a solution phase

More importantly, Purdy *et al.* [2004] showed that for phases such as β and γ in Figure 2-3a where $x^\gamma > x^\beta$ the $(D^\gamma - D^\beta)$ increases with increasing x_0. In other words "the likelihood of metastable phase formation is increased with supersaturation".

Equation 2-2 can be easily generalized to a multi-component system composed of k elements:

$$D^\beta = (x_2^\beta - x_{eq}^\alpha, \dots, x_k^\beta - x_{eq}^\alpha) \times \mathbf{H} \times \begin{pmatrix} x_{2,0}^\alpha - x_{eq}^\alpha \\ \vdots \\ x_{k,0}^\alpha - x_{eq}^\alpha \end{pmatrix} \qquad 2\text{-}4$$

where **H** the Hessian of the molar Gibbs energy. If analytical expressions of Gibbs energies of phases in the system are available the formation of metastable phases can be speculated using this equation.

Extreme caution must be taken into account to interpret the results of such speculations. Firstly, it must be noted that this method assumes homogeneous nucleation of intermetallic compounds from the melt. However, it is known that this situation is hardly achieved in solidification and intermetallics are forming through heterogeneous nucleation on Al dendrites or other solid phases in the system. In this case a reliable prediction of metastable phase selection must account for the surface energies of the intermetallic phases. Moreover, as explained so far this method only predicts what phases have a higher potential to nucleate. In order for these phases to become a constituent of the cast microstructure they have to be able to grow. The growth rate of different phases must also be taken into account for a reliable determination of the metastable phase selection. Therefore, a higher driving force for the onset of precipitation of a phase does not guarantee its formation, it only indicates such possibility.

The absence of the RM phase in the as-cast alloy does not necessarily preclude its formation during a subsequent heat treatment. In this case, the precipitation of a target phase cannot be predicted with any certainty unless isothermal sections of the ternary Al-R-M system are known. If analytical expressions for the Gibbs energy of phases in the system are available, the isothermal sections can be constructed by satisfying the equilibrium criterion.

It is seen that the availability of a thermodynamic database on the Al-R-M systems is crucial to predict whether the fabrication of a FCC/RM material is feasible. Such a database can be developed by employing the CALPHAD (CALculation of PHAse Diagram) method [Saunders & Miodownik 1998]. This method is now briefly explained.

2.4 CALPHAD method

The CALPHAD method is summarized in Figure 2-5. In this method, first, all the phase diagram information and thermo-chemical data related to the system are collected and the Gibbs energies of each phase are described by a mathematical formalism with a number of adjustable parameters. Then, by using an optimization technique such as the least square method, the parameters are evaluated by fitting the model to all experimental data. Once this is done for binary systems, the higher order systems can be evaluated by extrapolating binary data and making necessary adjustments. The evaluated Gibbs energies can now be used to calculate all types of thermodynamic properties and plot phase diagrams and property diagrams.

Since the optimization is a mathematical procedure critically dependent on the statistical treatment of input data, careful attention must be paid to the reliability and accuracy of the experimental data and these results must be carefully weighted. After assessing the experimental information, the next step is to assign a model to all phases in the system. There are several models used for Gibbs energy of phases based on the type

of phase. Solution phases, stoichiometric phases and ordered phases are modeled differently. These models are explained in the next section.

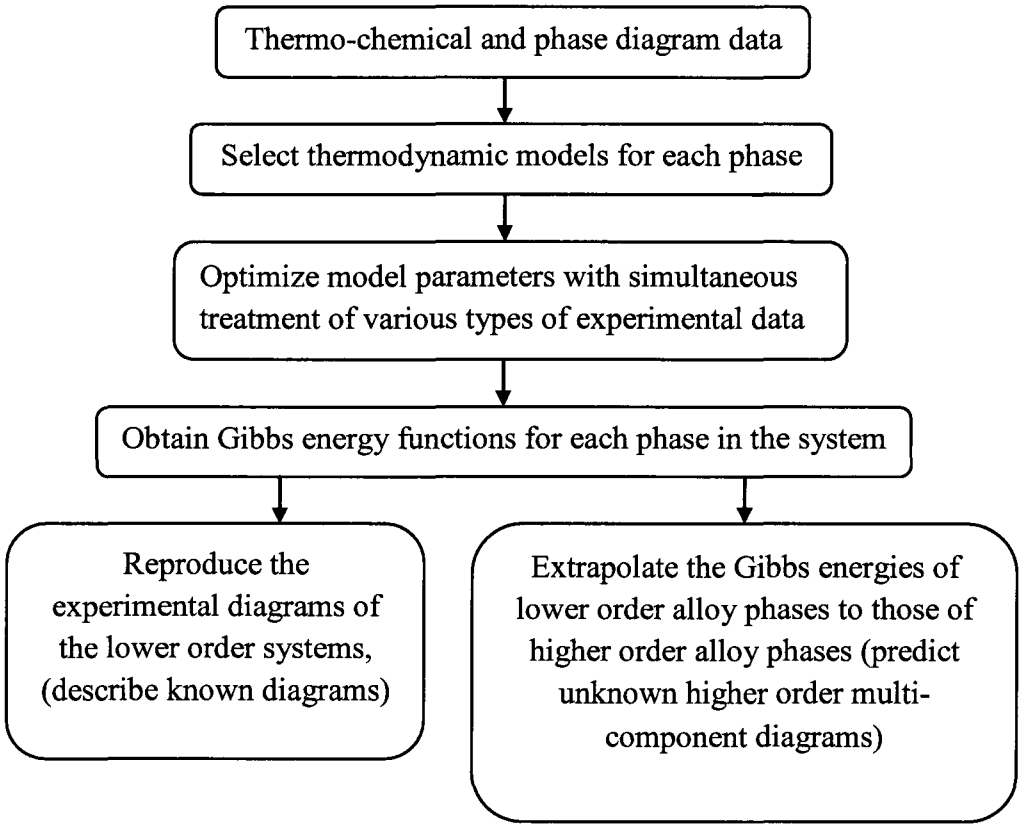

Figure 2-5 Phenomenological approach used to obtain a thermodynamic description of a multi-component system (the CALPHAD method)

2.4.1 Models of Phases

In the CALPHAD method, the Gibbs energy of the phase is modeled because all other thermodynamic properties can be derived from it. The phase model refers to an

analytical description of the Gibbs energy of a phase as a function of temperature (T), composition (x), and, if necessary, pressure (P). *i.e.*

$$G = G(T, P, x) \qquad 2\text{-}5$$

In multi-component systems, the concentration dependence of the Gibbs energy is usually divided into three contributions:

$$G(x) = G^{reference} + G^{ideal} + G^{excess} \qquad 2\text{-}6$$

where $G^{reference}$ is the Gibbs energy contribution from a mechanical mixture of the components of the phase. That is,

$$G^{reference} = \sum_i x_i G_i^\circ \qquad 2\text{-}7$$

The G_i° is the contribution of the pure component i to the Gibbs energy of the phase. The data for G_i° are provided in the literature in the form of $G\text{-}H^{SER}$ where SER stands for "standard element reference" that is the element's stable phase at 298.15 K and one atmosphere pressure. The reason behind this is that the Gibbs energy of an element has no absolute value and therefore a referemce state must be selected. These data are usually expressed as a power series of temperature:

$$G_i^\circ = a + bT + cT\ln T + \sum d_n T^n \qquad 2-8$$

where n is typically 2, 3, -1, 7 and -9 [Dinsdale 1991]. The ideal term in equation 2-6 is merely the configurational entropy of ideal mixing of components and expressed by the following equation:

$$G^{ideal} = \mathrm{RT}\sum_i x_i \ln x_i \qquad 2\text{-}9$$

The non-ideal part of the Gibbs energy is expressed by the excess term. Since no theoretical expression is available for the compositional and temperature dependency of this term, it is expressed by a pure mathematical model with a number of adjustable parameters. The most commonly used formalism for expressing excess term is Redlich-Kister polynomial [Redlich & Kister 1948]. For a binary system it is written as:

$$G^{ex} = x_1 x_2 \sum_{v=0}^{k} {}^{v}L(x_1 - x_2)^v \qquad 2\text{-}10$$

where ${}^{v}L$ is called interaction parameter and once again represents the temperature dependent part of the concentration dependent term, G^{excess}. It is usually described by an expression like equation 2-8.

The Gibbs energy expression explained above is used to model phases such as liquid and disordered solid solutions where components are mixed randomly. On the other end of the mixing spectrum, a stoichiometric intermetallic phase with a fixed composition can be considered. In this case G^{ideal} is equal to zero since there is no mixing, and, G^{excess} is merely the Gibbs energy of formation of the phase from the

mechanical mixture of constituent elements. The Gibbs energy of stoichiometric phases becomes:

$$G^{\varphi} = \sum_i x_i G_i^{\circ} + \Delta G^f \qquad 2-11$$

where ΔG^f is usually modeled as a linear function of temperature.

A more sophisticated model called the sublattice model is used to describe the Gibbs energy of ordered solution phases such as an intermetallic phase with a range of homogeneity. The basic premise for this model is that a "sublattice" is assigned for each distinct site in the crystal structure and random mixing of components is assumed within each sublattice.

This model was first introduced by Hillert and Staffanson [1970] and later refined by Sundman and Agren [1981] and Andersson *et al.* [1986]. It is also known as the compound energy formalism [Hillert 2001]. A binary phase with two sublattices where the two components can mix in both sublattices is represented as $(A,B)_p(A,B)_q$. p and q are stoichiometric coefficients and one mole of formula units thus contains p+q moles of atoms. Instead of mole fractions of constituents (x_i), this model deals with site fraction which refers to the fractions of a constituent in a sublattice. It is commonly represented by letter "y" and it obeys the following relations:

$$\sum_i y_i^s = 1 - y_{Va}^s \quad \& \quad \frac{\sum_s n_s y_i^s}{\sum_s n_s (1 - y_{Va}^s)} = x_i \qquad 2\text{-}12$$

where n_s represents the stoichiometric coefficient of the sublattice s and y_{Va}^{s} is the site fraction of vacancies in that sublattice.

The Gibbs energy of the binary phase shown above is described by the following expression,

$$\Delta G^{\varphi} = \sum_i y_i' \sum_j y_j'' \Delta G^{\circ}_{i:j} + RT\left(\sum_i p y_i' \ln y_i'' + q y_i'' \ln y_i''\right) + y_i' y_j' \sum_k y_k'' \sum_{v=0}^{n} {}^{v}L_{i,j:k}(y_i' - y_j')^{v} + y_i'' y_j'' \sum_k y_k' \sum_{v=0}^{n} {}^{v}L_{i,j:k}(y_i'' - y_j'')^{v} + y_i' y_j' y_i'' y_j'' L_{i,j:i,j} \quad 2\text{-}13$$

where y_i' and y_i'' are site fractions of element i in the first and second sublattices respectively. The commas in the subscripts separate constituents within a sublattice and the colons separate constituents in different sublattices. Interaction parameters once again expressed in the form of equation 2-8. $\Delta G^{\circ}_{i:j}$ describes the Gibbs energy of the "end-member" phases. The end-member phases are formed when each sublattice is occupied only by one kind of species and can be either real or hypothetical. This model can be easily generalized to a higher order systems and higher number of sublattices.

The model that was previously described for random solution phases is actually a particular case of this model in which there is only one sublattice that accomodates all components in which $y_i^s \equiv x_i$. In addition to ordered solution phases, this formalism is

successfully used to model interstitial solid solutions, ionic-liquids [Hillert *et al.* 1985, Chen *et al.* 2003, Grundy *et al.* 2003], and order-disorder transformations [Ansara *et al.* 1988, Ansara *et al.* 1997, Dupin & Ansara 1999].

The choice of sublattice model for a specific phase is normally based on the crystal structure information available for that phase. Gathering information on the crystallography and site occupancy of each and every phase in a system is an important task. It provides a physical basis for the analytical expressions of the Gibbs energies. It is proven that choosing a crystallographically sound descriptions for the phases results in a correct shape of phase boundaries and better agreement between calculated and experimental data which in turn results in a more reliable extrapolation to higher order systems [Joubert 2008, Nakano *et al.* 2005, Kumar *et al.* 1998].

2.4.2 Optimization procedure

If pressure is assumed constant and equal to atmospheric pressure as it is in a wide variety of metallurgical processes then the Gibbs energy of a system in which phases are described by the above models is a function of mole fraction, temperature, and a vector of adjustable parameters $\vec{C}$:

$$G = G(x, T, \vec{C}) \qquad 2\text{-}14$$

The optimization procedure starts with assigning some initial values to these unknown parameters. Next for each available experimentally measured thermodynamic and phase diagram data, F, the error is calculated according to the following expression:

$$\text{error} = \omega\left(F^{experimental} - F^{calculated}\left(x^{exp}, T^{exp}, \vec{C}\right)\right) \qquad 2\text{-}15$$

where ω is the statistical weight of the experimentally measured value. Recall that all thermodynamic properties can be calculated if an analytical expression for the Gibbs energy is available. By using the least square method, a set of optimum parameters can be found by minimizing the sum of squared errors of all available experimental data.

$$\sum_{i}^{number\ of\ experiments} [(\text{error})_i]^2 = min \qquad 2\text{-}16$$

The problem of thermodynamic optimization is a non-linear least squares problem which relies upon an iterative procedure to find statistically best values of adjustable parameters. This mainly comes from the fact that the errors in the x^{exp} and T^{exp} which are the arguments of the target function are also considered.

Several optimization tools are available for carrying out the minimization procedure. These are BINGSS [Lukas *et al.* 1977, Lukas & Fries 1992], TERGSS [Lukas & Fries 1992], PARROT [Jansson 1984] and OPTISAGE[1]. To perform a thermodynamic optimization, one should be able to link the models of phases, the minimization engines

[1] http://www.crct.polymtl.ca/factsage/fs_optisage.php

and the databases together. This is made possible through many available software packages such as Thermo-Calc [Andersson *et al.* 2002], FactSage [Bale *et al.* 2002], PANDAT [Chen *et al.* 2002], MTDATA [Davies *et al.* 2002], etc.

The PARROT module of Thermo-Calc software is used in the present study to optimize the Al-La-Mg ternary system. To explore the possibility of fabricating a two-phase material comprised of aluminum (FCC) and LaMg (B2), the POLY3 module of Thermo-Calc is employed to perform Scheil-Gulliver simulations and evaluate the driving forces of the onset of precipitation for solid phases at different degrees of supercooling. The Al-Ce-Mg system was already optimized [Grobner *et al.* 2002]. The results of this optimization will be used to predict the likelihood of fabricating an Al/CeMg material.

2.5 Thermodynamic optimization of Al-La-Mg system

In order to optimize a ternary system, one has to start with the binary sub-systems. Later, the ternary system will be constructed by the extrapolation of the corresponding binaries with the addition of ternary parameters when necessary. Various geometric extrapolation methods have been proposed to calculate ternary excess Gibbs energy. Some of these models are shown in Figure 2-6. The binary excess Gibbs energies evaluated at the binary points a, b, and c are used to estimate the excess Gibbs energy at the ternary point P. How to choose points a, b, and c is what differentiates these methods.

Currently, the Muggianu model is predominantly used by researchers in the optimization of ternary and higher order systems. In this model, the excess Gibbs energy of a phase in a k-component system is estimated by the following expression:

$$G_k^{excess} = \sum_{i}^{k-1} \sum_{j=i+1}^{k} \frac{4x_i x_j}{(1+x_i-x_j)(1+x_j-x_i)} G^{ij}\left(\frac{(1+x_i-x_j)}{2}, \frac{(1+x_j-x_i)}{2}\right) \quad 2\text{-}17$$

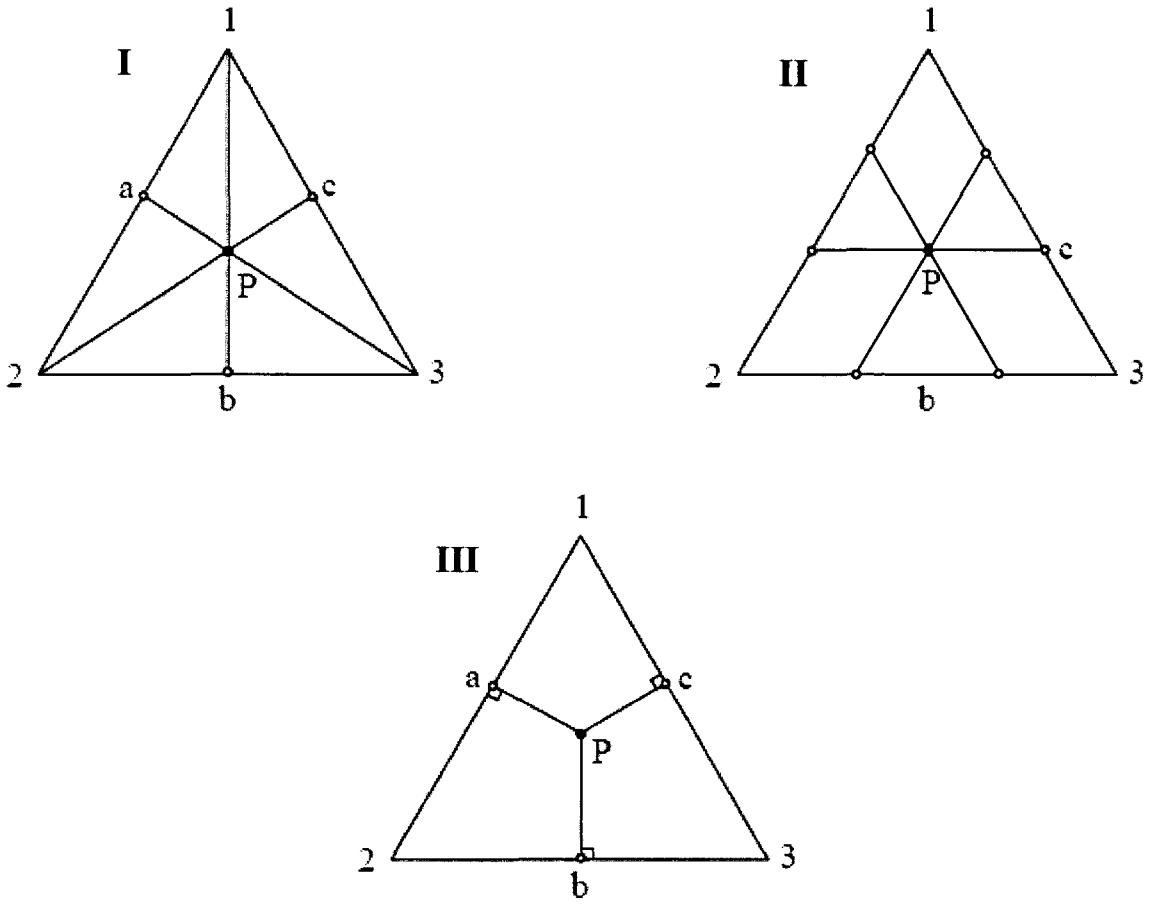

Figure 2-6 Ternary extrapolation methods I) Kohler model [Kohler 1960] II) Colinet model [Toop 1965] III) Muggianu model [Muggianu & Gambino 1975]

If binary G^{ij} s are expressed by the Redlich-Kister formalism (equation 2-10) then their substitution in the above expression gives:

$$G_k^{excess} = \sum_{i}^{k-1} \sum_{j=i+1}^{k} x_i x_j \sum_{v=0}^{n} {}^{v}L(x_i - x_j)^v \qquad 2\text{-}18$$

It is seen that all Redlich-Kister terms of the binary systems are reproduced. This is only true for the zero order term (regular solution) in the Kohler model and zero and first order terms in the Colinet formalism. The Muggianu model is employed in the present optimization because of this important feature.

2.5.1 Binary systems

All three binary systems Al-Mg, Al-La, and La-Mg have been already optimized. For the Al-Mg system, the optimization results by Liang *et al.* [1998] are adopted. Several assessments exist for the Al-La system [Cacciamani & Ferro 2001, Yin *et al.* 2000, Zhou & Napolitano 2006]. The most recent optimization on this system [Zhou & Napolitano 2006] showing the best agreement with the experimental data is used in the present optimization. The La-Mg binary data are taken from the results of an optimization by Guo *et al.* [2004]. There is a good agreement between the available experimental data for this system and those calculated based on the results of this optimization. However, models that are used for some of the intermetallic phases in this system, namely

Laves_C15 and BCC_B2, are not properly chosen. The proper model for each of these phases is explored next. Equilibrium phase diagrams, description of phase, and calculated invariant reactions of the binary systems adopted here are summarized in appendix I.

2.5.1.1 Laves_C15 phase

Laves phases are a family of topologically close-packed intermetallic compounds that appear in numerous binary and ternary systems. There are three modifications of this phase: the $MgZn_2$ (C14), the $MgCu_2$ (C15), and the $MgNi_2$ (C36). Villars *et al.* [1991] have reported totally 1428 intermetallic phases with the Laves structure; 806 of them are of C15 prototype. The Mg_2La intermetallic phase which exists in the La-Mg phase diagram has a cubic C15 ($MgCu_2$ type) crystal structure. The crystallographic data of this prototype of Laves family is presented in Table 2-2.

Table 2-2 Crystallographic data and site occupancies of the Laves_C15 phase

Strukturbericht designation	C15	
Space group	$Fd\bar{3}m$	
Pearson symbol	cF24	
Wyckoff position	8a	16d
Point symmetry of site	$\bar{4}3m$	$\bar{3}m$
Co-ordination number	16	12
Site occupation	Mg	Cu

Ansara *et al.* [1997] and Ferro and Cacciamani [2002] critically reviewed models that are used for the description of the Laves_C15 phase in different systems and suggested that since this structure consists only of two crystallographic sites (Table 2-2), a two sublattice model, $(A,B)_2$ $(A,B)_1$, is the only physically reasonable choice for modeling of this phase. Such model is successfully used in several systems including the Al-La system [Zhou & Napolitano 2006] mentioned above in which the Al_2La phase is modeled as $(\mathbf{Al},La)_2$ $(Al,\mathbf{La})_1$. A bold font is used here to indicate the major constituent in a sublattice.

Since there is no experimental evidence of the existence of a homogeneity range for the Mg_2La phase in the literature, Guo *et al.* [2004] treated it as a line compound with two sublattices and only one type of atom in each sublattice: $(Mg)_2$ $(La)_1$. For the sake of compatibility with the description of the Laves_C15 phase adopted in several other systems, it was decided to change the model of this phase to $(La,\mathbf{Mg})_2(\mathbf{La},Mg)_1$. It should be mentioned that the change of model is actually a necessity here since La inevitably enters both sublattices when a ternary database of Al-La-Mg is to be composed of the Al-La and La-Mg binary systems.

2.5.1.2 BCC_B2 phase

The crystal structure of this phase is shown in Figure 2-1 in page 6. It looks very much like the BCC crystal structure with the exception that atoms are not randomly

mixed in all positions. In the disordered BCC crystal structure (A2) there is only one atomic position "2a" (Table 2-3). This position splits into two distinctive positions in the B2 structure: 1a which is the (0,0,0) position and 1b which is the (1/2,1/2,1/2) position. Each of these positions is preferentially occupied by a distinctive element. In this sense, the B2 crystal structure is merely an ordered derivative of the disordered A2 structure.

The phase model of the A2 structure consists of one sublattice representing the 2a Wyckoff position (Table 2-3) where all substitutional elements mix. Optionally, another sublattice can be added to incorporate vacancies and interstitial elements. The sublattice model of this phase is $(A,B,\ldots)_1(Va,c,d,\ldots)_3$. Where Va represents vacancy and capital and small letters indicate substitutional and interstitial elements respectively. By imitating the crystallographic guidelines mentioned earlier, the model of the B2 phase is derived by splitting the substitutional sublattice of the A2 phase into two separate sublattices representing the 1a and 1b Wyckoff positions. The model for the B2 phase will become, $(A,B,\ldots)_{0.5}(A,B,\ldots)_{0.5}(Va,c,d,\ldots)_3$. This model is successfully used in the optimization of the Mg-Y binary system [Fabrichnaya *et al.* 2003] where the MgY phase with B2 crystal structure is modeled as the ordered part of the A2 phase.

The LaMg phase in the La-Mg phase diagram also has the B2 crystal structure. In the optimization of the La-Mg system by Guo *et al.* [2004] this phase is treated as a stoichiometric compound with the following simple model: $(La)_1(Mg)_1$. Based on the above discussion, it is clear that a change of sublattice model of this phase is necessary to account for the crystallographic aspects of this phase.

Table 2-3 Crystallographic data and site occupancies of the BCC_A2 and BCC_B2 phases

Strukturbericht designation	A2	B2	
Space group	$Im\bar{3}m$	$Pm\bar{3}m$	
Pearson symbol	cI2	cP2	
Prototype	W	CsCl	
Wyckoff position	2a	1a	1b
Point symmetry of site	$m\bar{3}m$	$m\bar{3}m$	$m\bar{3}m$
Site occupation	W	Cl	Cs

It is not possible to change the sublattice model of a phase when a system has been already optimized. As a result, the presence of a more crystallographically sound model for constituent phases of the system is sometimes a reason for the re-optimization of that system. On the other hand, the change of sublattice model becomes necessary when a higher order system is to be composed of binary systems in which a particular phase is modeled differently. This lack of compatibility between binary systems is a serious problem which forces researchers to engage in the optimization of binary subsystems while a good assessment of such systems already exists. Here, a simple approach to change the sublattice of a phase without re-optimizing the system is proposed and applied to the Laves and B2 phases in the La-Mg system.

2.5.2 How to change the sublattice model without re-optimization

The approach is to use additional interaction parameters and end-members' Gibbs energies introduced by a change of sublattice model, along with already optimized

parameters of all other phases in the system to undo loss of agreement with the experimental data caused by that alteration of the model. Such an approach has been used by Dupin and Ansara [1999] in a somewhat different context.

To better explain how this approach is applied, let us consider the Laves_C15 phase in the La-Mg system is explained. It was mentioned that the sublattice model of this phase should be altered from $(Mg)_2(La)_1$ used in the optimization by Guo *et al.* [2004] to $(La,\mathbf{Mg})_2(\mathbf{La},Mg)_1$ in order to reflect the crystallographic nature of this phase and also to ensure the compatiblity with the model used for this phase in the Al-La system. If this is done and the energies of $(La)_2(La)_1$ and $(Mg)_2(Mg)_1$ end members available in literature [Zhou & Napolitano 2006,Liang *et al.* 1998] are added to the database, then, noticeable changes will appear in the phase diagram of La-Mg. Figure 2-7 shows the changes caused by the change of sublattice model of the Laves phase. It is seen that the Laves phase has slightly shifted towards lower Mg concentrations and it now has a narrow homogeneity range. It also forms congruently from the melt rather than peritectically as predicted by Guo *et al.* [2004]. The characteristics of invariant reactions involving this phase will not remain intact either. The temperatures of invariant reactions are noted in Figure 2-7 for comparison. These changes could have been more appreciable had the phase been stable over a wider temperature range.

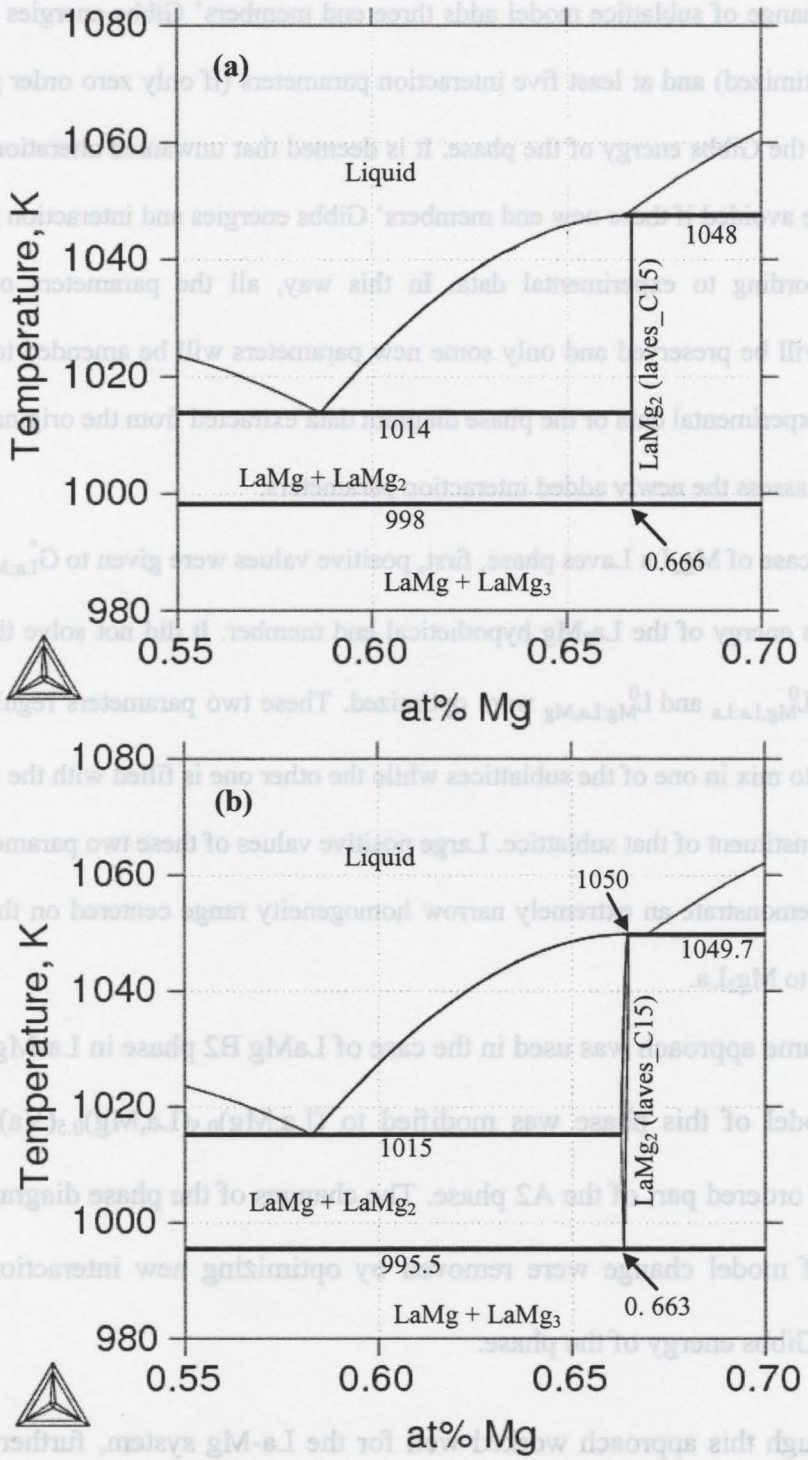

Figure 2-7 Comparison of the portions of the La-Mg diagram concerning the Laves_C15 phase calculated by using a) optimized data by Guo *et al.* [04Guo] and b) the sublattice model of the Laves phase is changed to $(La,Mg)_2(La,Mg)_1$ and $G^{\circ}_{La:La}$ and $G^{\circ}_{Mg:Mg}$ are added to the database

The change of sublattice model adds three end members' Gibbs energies (two of which are already optimized) and at least five interaction parameters (if only zero order parameters are considered) to the Gibbs energy of the phase. It is deemed that unwanted alterations in the phase diagram can be avoided if these new end members' Gibbs energies and interaction parameters are optimized according to experimental data. In this way, all the parameters of the existing optimization will be preserved and only some new parameters will be amended to the database. Either actual experimental data or the phase diagram data extracted from the original optimization can be used to assess the newly added interaction parameters.

In the case of Mg_2La Laves phase, first, positive values were given to $G^{\circ}_{La:Mg}$ representing standard Gibbs energy of the La_2Mg hypothetical end member. It did not solve the problem. In the next step, $L^0_{Mg,La:La}$ and $L^0_{Mg:La,Mg}$ were optimized. These two parameters regulate the ability of La and Mg to mix in one of the sublattices while the other one is filled with the element which is the major constituent of that sublattice. Large positive values of these two parameters will force the phase to demonstrate an extremely narrow homogeneity range centered on the composition corresponding to Mg_2La.

The same approach was used in the case of LaMg B2 phase in La-Mg system. The sublattice model of this phase was modified to $(La,Mg)_{0.5}(La,Mg)_{0.5}(Va)_3$ and it was treated as the ordered part of the A2 phase. The changes of the phase diagram introduced as a result of model change were removed by optimizing new interaction parameters added to the Gibbs energy of the phase.

Although this approach worked well for the La-Mg system, further speculations are necessary to validate its applicability to other systems and find its possible limitations. To name one, it is inevitable that the "goodness" of the optimization outcome

(the agreement between experimental and calculated data) depends on the goodness of the original optimization. This is because in this approach all previously optimized variables are preserved and the database is only amended by a few new variables.

For example, an earlier experience in applying this approach was directed at the Laves_C15 phase in the Al-La system optimized by Cacciamani and Ferro [2001]. They correctly used the model described above for this phase (two sublattices containing both elements: $(\mathbf{Al},La)_2(Al,\mathbf{La})_1$), however, the model parameters were poorly optimized so that the phase showed a solubility range despite the experimental investigations indicating the phase as a stoichiometric phase. Furthermore, a general lack of good agreement between calculated phase diagram and experimental data is observed. The aim was to use unoptimized interaction parameters of the Laves phase to remove the artificial solubility range. This goal was successfully achieved (Figure 2-8); however, the temperature of invariant reactions involving this phase could not be precisely reproduced. It is also seen that the liquidus line is shifted compared to the original optimization.

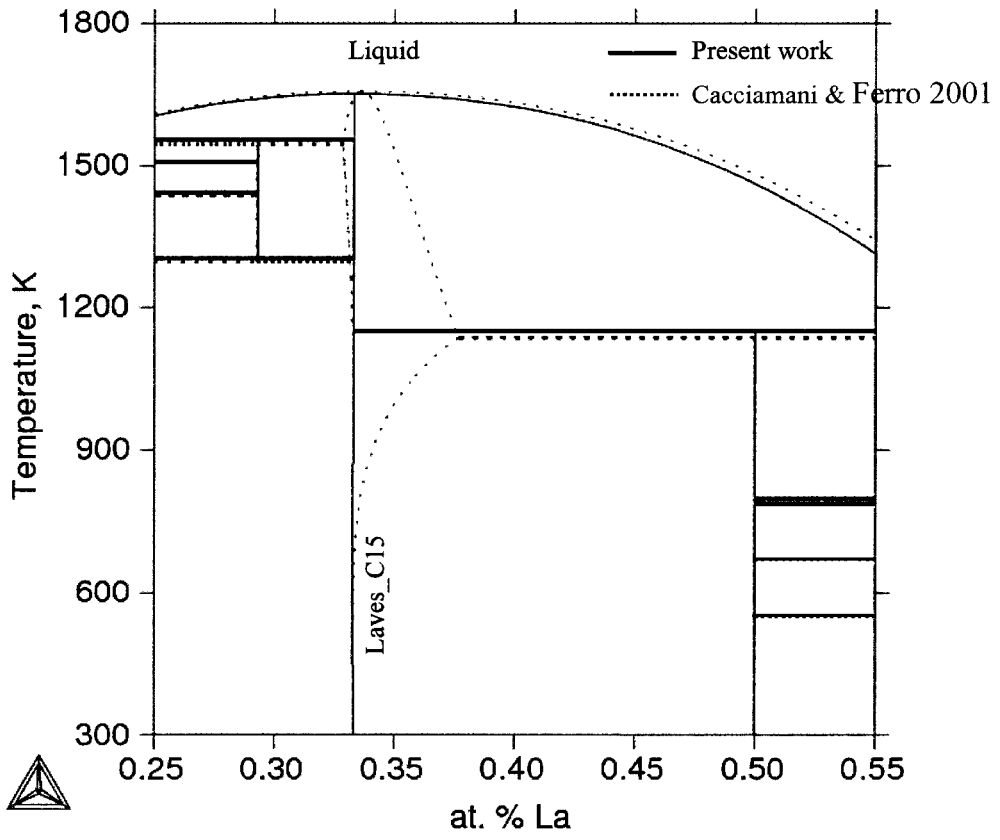

Figure 2-8 Calculated portion of the Al-La phase diagram concerning the Laves_C15 phase

2.5.3 Experimental information on the Al-La-Mg system

The experimental studies on the Al-La-Mg system prior to 1988 have been reviewed by Rogl [1988]. These studies include a complete 400°C isothermal section constructed by Odinaev *et al.* [1988]. They reported the existence of three ternary phases: $LaMg_{1-x}Al_x$, $LaMg_{2-x}Al_x$, and $Al_2Mg_{0.85}La_{0.15}$. The first one is actually an extension of the LaMg B2 binary phase into the ternary region. The solubility of Al in this phase reaches

20 at.% at 400°C. The $LaMg_{2-x}Al_x$ phase has the Laves_C15 crystal structure. It shows a wide solubility range starting from Al_2La in the Al-La binary system to Mg_2La in La-Mg binary system with a large miscibility gap expanding from 30 at.% to 50 at.% Al at 400°C. The ternary phase $La_{0.15}Mg_{0.85}Al_2$ (labeled τ here) is a stoichiometric phase with an unknown crystal structure. Zheng *et al.* [1983] studied a small part of the Al-rich liquidus surface and reported a ternary eutectic reaction L ⇌ αLa $_3Al_{11}$+Mg_2Al_3+Al at 445°C.

Following the review of experimental information by Rogl [1988], Odinaev and Ganiev [1995] studied the Al-La Mg system by means of differential thermal analysis (DTA), X-ray diffraction, and metallography and reported seven pseudobinary sections, a partial liqudus surface and six ternary invariant reactions. They prepared 134 alloys in the same way as [Odinaev *et al.* 1988] and annealed them at 400°C for 20 days. They used a corundum crucible sealed in a quartz tube for the DTA analysis.

The isothermal section at 400°C published by Odinaev *et al.* [1988] was used to optimize the Gibbs energy of the ternary B2 and C15 phases. The Gibbs energy of the τ phase was optimized by using invariant reactions involving this phase reported by Odinaev and Ganiev [1995]. Due to some discrepancies between the calculated and experimental data that are explained in section 2.5.6.2 (page 50), it proved necessary to perform a DTA experiment to validate the optimized data. The details of this experiment are explained next.

2.5.4 Experimental procedure

A differential thermal analysis (DTA) was performed on two alloys with following compositions: Al – 20.1 wt.% La – 19.9 wt.% Mg and Al - 15.07 wt.% La – 14.93 wt.% Mg. From here on they will be referred to as A60 and A70 respectively. The basis for choosing these specific compositions is explained in section 2.5.6.2. Weighted amounts of 99.999 wt.% Al, 99.9 wt.% La, and 99.99 wt.% Mg were melted in an induction furnace under a dynamic argon atmosphere. The chamber of the furnace was evacuated and flushed with Ar several times before melting. The melt was stirred with a boron nitride rod before cooling to ensure homogeneity of the melt. The weight loss due to oxidation and evaporation was measured to be less than one percent. The compositions of the solidified alloys revealed by ICP are presented in

Table 2-4 Chemical compositions of alloys prepared for DTA

Alloy	Al	La	Mg
A60	61.3	18.7	20
A70	70.6	14	15.4

90-100 milligrams of each alloy were sealed in a stainless steel crucible under Ar to prevent oxidation of reactive Mg and La. The DTA analysis was performed using a Netzsch STA 409 instrument under argon. A heating/cooling rate of 10 degrees/min was

employed. The heating and cooling cycles were performed three times to ensure reproducibility of the results.

2.5.5 Thermodynamic models

The three ternary phases reported by Odinaev et al. [1988] are optimized in the present work. As discussed before, the ordered solid solution laves_C15 phase is modeled by a two sublattice model where all elements enter both sublattices. The Gibbs energy of this phase is expressed by the compound energy formalism. Redlich-Kister polynomials were used to express interaction parameters.

The sublattice model of the B2 phase is already described for the binary La-Mg system. To model the solubility range of Al in this phase, aluminum is also entered in both substitutional sublattices: $(Al,La,Mg)_{0.5}(Al,La,Mg)_{0.5}$. The compound energy formalism can be utilized to model order-disorder transformations. Ansara *et al.* [1988] were first to employ this approach. In their attempt, both ordered and disordered parts were modeled as one phase and to ensure the stability of the disordered phase some constraint had to be imposed on parameters describing ordering. Due to some drawbacks associated with this treatment [Saunders 1996, Ansara, Dupin & Sundman 1997] and the fact that it became unduly complicated for higher order systems, a new simplified formalism was introduced by Sundman [1991]. This formalism employs a two phase approach. This means that unlike the previous model, separate, yet related, phase models

are used for the ordered and disordered parts. Gibbs energies of both parts are described by one expression:

$$G_m = G_{\mathrm{m}}^{dis}(x_i) + G_{\mathrm{m}}^{ord}(y_i^1, y_i^2) - G_{\mathrm{m}}^{ord}(y_i^1 = x_i, y_i^2 = x_i) \qquad 2\text{-}19$$

where $G_{\mathrm{m}}^{dis}(x_i)$ represents the Gibbs energy contribution from disordered part of the phase and $G_{\mathrm{m}}^{ord}(y_i^{'}, y_i^{"})$ adds the ordering parameters. The third term, $G_{\mathrm{m}}^{ord}(y_i^1 = x_i, y_i^2 = x_i)$, describes the extraneous contribution of $G_{\mathrm{m}}^{ord}(y_i^1, y_i^2)$ in the disordered state. It is subtracted to ensure that the parameters of the ordered state have no effect on the disordered part. The coefficients of $G_{\mathrm{m}}^{dis}(x_i)$ and $G_{\mathrm{m}}^{ord}(y_i^1, y_i^2)$ can be optimized and added to the database. The subtraction is done automatically by the software. A more detailed description of this formalism applied to ~~A2~~ B2 transformation is given by Dupin and Ansara [1999].

Since the crystal structure of the $Al_2Mg_{0.85}La_{0.15}$ (τ) phase is unknown, it is treated as a stoichiometric phase with three sublattices each sublattice is completely filled by atoms of one component. The Gibbs energy of this phase is given as:

$$G_{\mathrm{m}}^{\tau} = 2G_{\mathrm{Al}}^{\circ} + 0.85G_{\mathrm{Mg}}^{\circ} + 0.15G_{\mathrm{La}}^{\circ} + \Delta G_f^{\tau} \qquad 2\text{-}20$$

where G_i° represents the Gibbs energy of pure component i in its stable phase at 298.15 K [Dinsdale 1991] and ΔG_f^{τ} is the Gibbs energy of the formation for the compound, modeled as a linear function of temperature.

2.5.6 DTA results

An example of the DTA heating/cooling curves for the A70 alloy is shown in Figure 2-9. The presence of two major peaks marked by (b) and (c) is apparent in the graphs. In addition, there is a smaller peak at about 800°C in the cooling curve (marked by the letter a). A change of slope is noticeable in the heating curve at the temperature corresponding to this small peak.

Such small heat effects are expected at the liquidus temperatures where an intermetallic compound or a solution phase starts to precipitate from the melt. To illustrate this point, the ternary Al-Ce-Mg system which is very similar to the Al-La-Mg system is considered. A vertical section Al-τ ($Al_{13}Mg_6Ce$) of this system is shown in Figure 2-10. The optimized data of Grobner *et al.* [2002] are employed to construct this diagram. The enthalpy changes during solidification of one mole of an Al - 15.3 wt.% Mg – 14.7 wt.% Ce alloy is calculated for both equilibrium (lever rule) and Scheil conditions. A dH/dT vs. T graph resembles the results that are achieved by a DTA experiment. Figure 2-11 portrays the calculated dH/dT vs. T curve for this alloy. It is seen that in both cases the intensity of the peak associated with the liquidus point (#1) is appreciably less than the other two peaks especially the one which is associated with an invariant reaction (peak #3: $L + \alpha\text{-}Ce_3Al_{11} \rightarrow \tau + Al$ in the case of equilibrium cooling and $L \rightarrow \tau + Al + Al_{12}Mg_{17}$ in the case of the Scheil condition). Based on this speculation it is believed that the peak "a" in Figure 2-9 is associated with the liquidus temperature of the alloy A70.

Such small heat effects were also recorded at high temperatures for alloy A60 (Figure 2-12). The temperatures of the peaks extracted from DTA curves are summarized in Table 2-5 for both alloys.

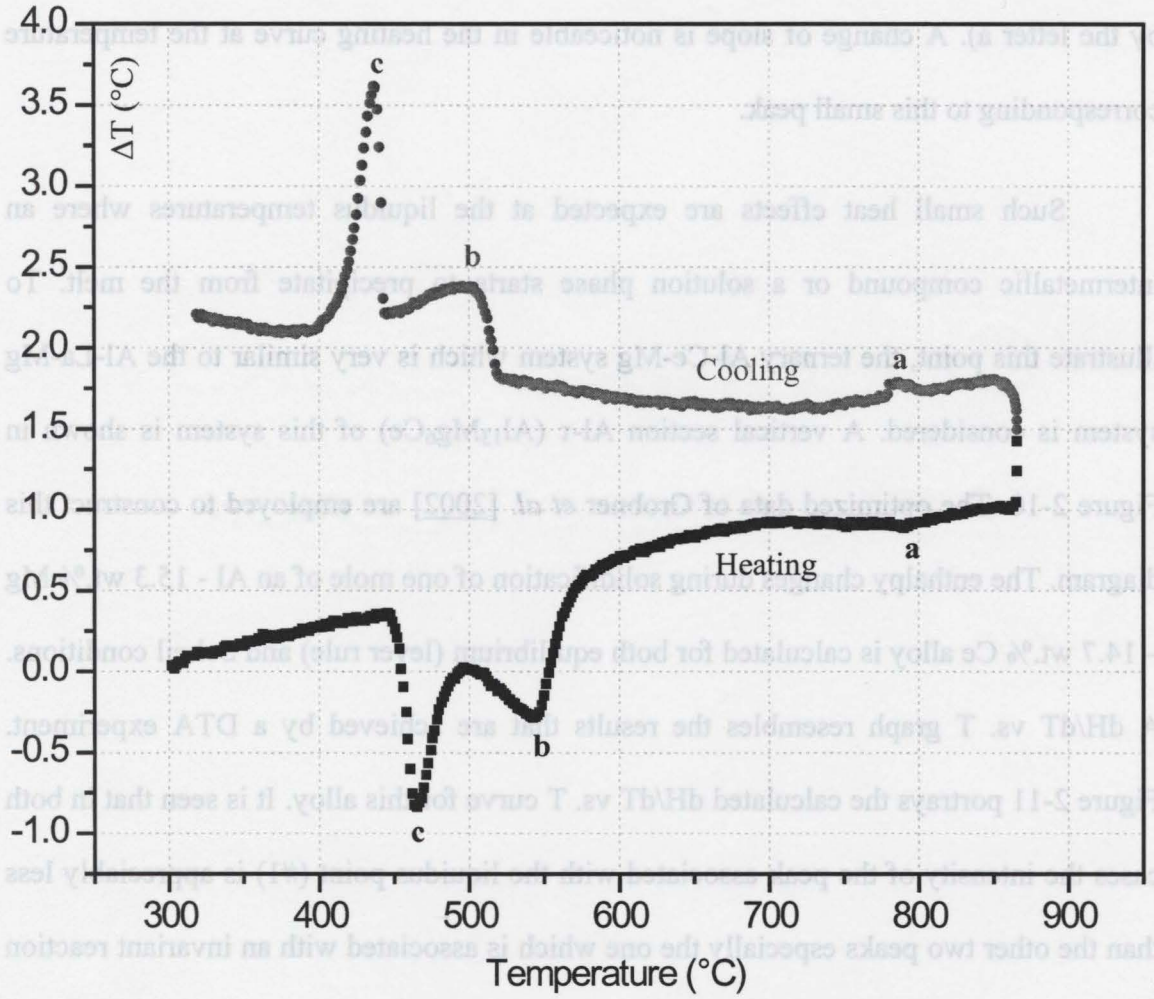

Figure 2-9 DTA results for alloy A70

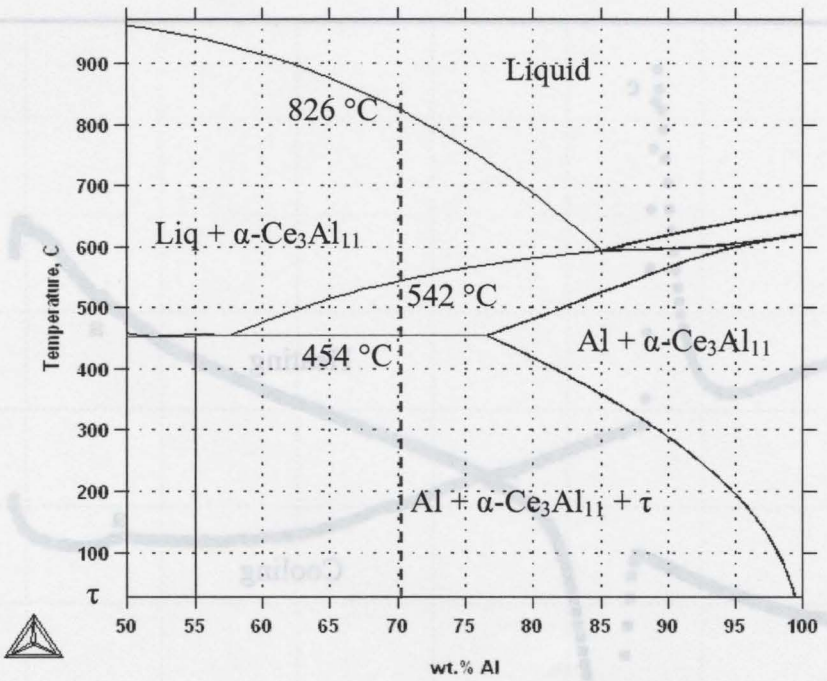

Figure 2-10 Calculated Al-τ section of the AL-Ce-Mg system

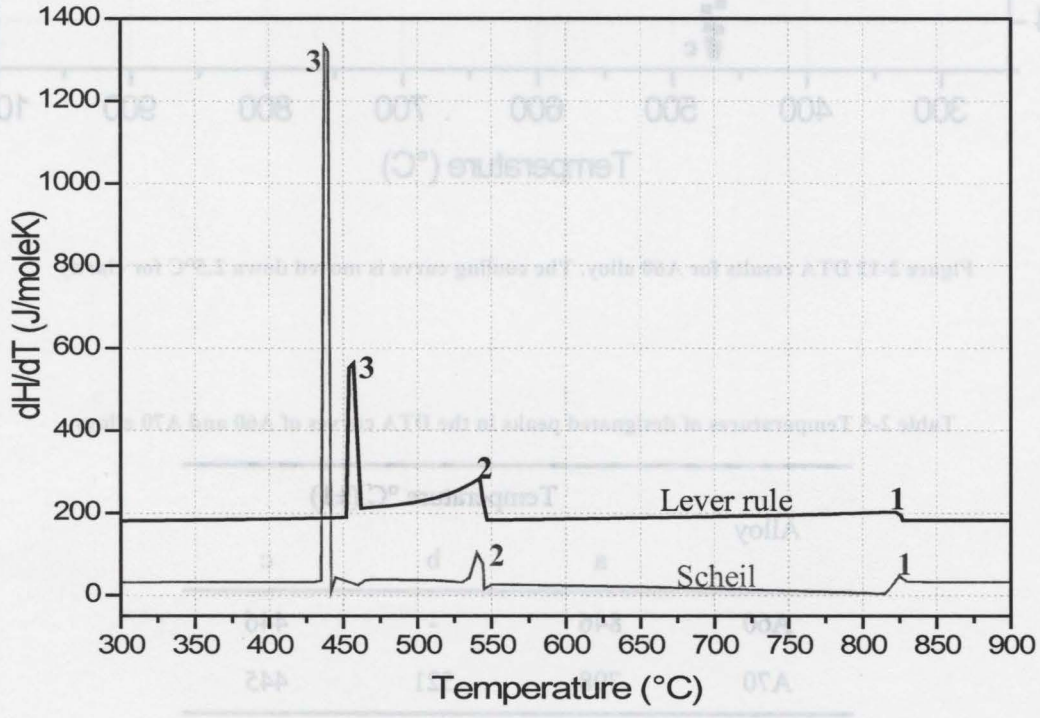

Figure 2-11 dH/dT obtained from the enthalpy–temperature predictions for Al – 14.7 wt.% Ce – 15.3 wt.% Mg alloy computed using optimized data of Grobner *et al.* [2002] for lever and Scheil conditions. The curve for lever rule is shifted up 150 J/moleK for clarity

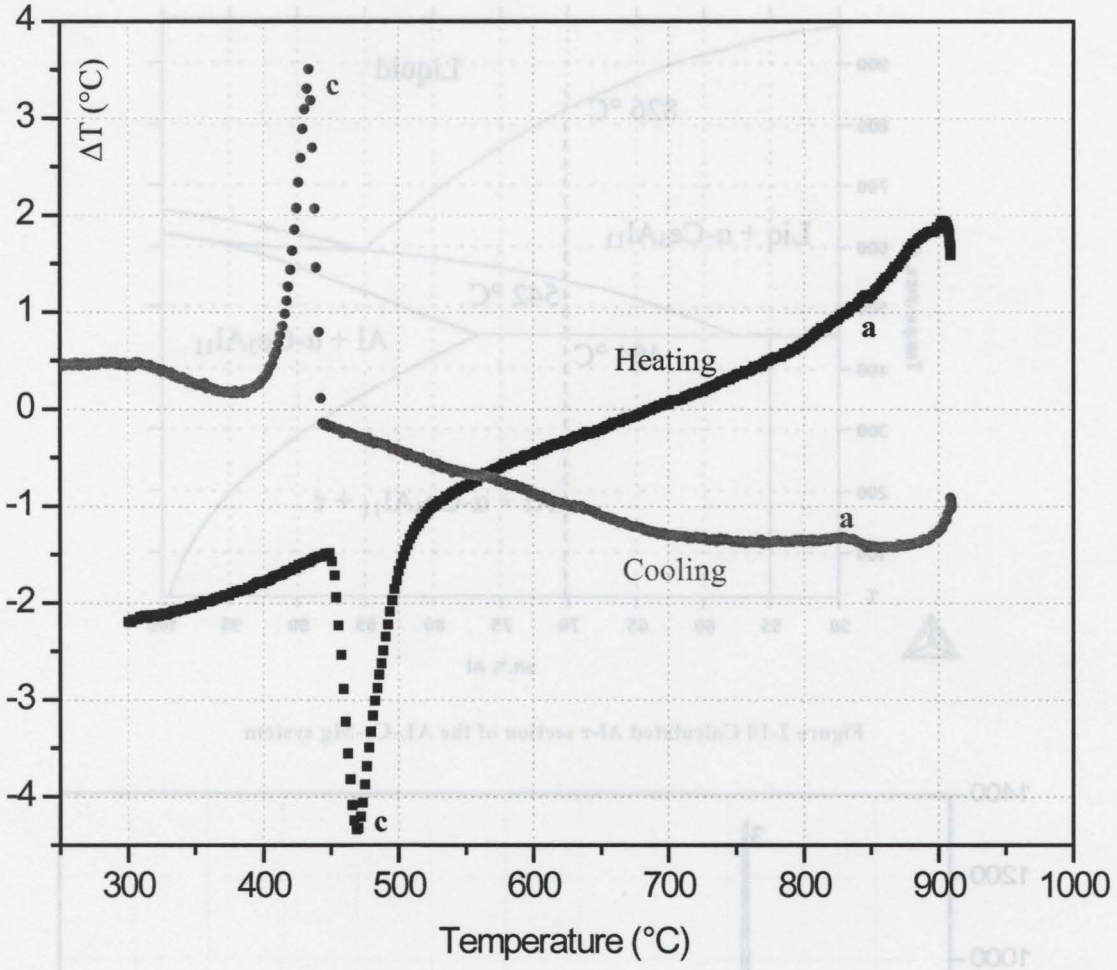

Figure 2-12 DTA results for A60 alloy. The cooling curve is moved down 2.5°C for clarity

Table 2-5 Temperatures of designated peaks in the DTA curves of A60 and A70 alloys

Alloy	Temperature °C (±1)		
	a	b	c
A60	846	-	446
A70	798	521	445

2.5.7 Optimization results

The values of the optimized parameters for the Laves_C15, BCC_B2, and τ phases are presented in Table 2-5 along with those borrowed from binary optimizations.

2.5.7.1 La-Mg system

The La-Mg phase diagram calculated using optimized data is shown in Figure 2-13. It is in complete agreement with the results of optimization by Guo *et al.* [2004]. The temperature and composition of the invariant reaction and the liquidus line are virtually indistinguishable from those predicted by Guo *et al.* [2004].

Figure 2-14 compares molar Gibbs energies of the Laves_C15 phase at 1025 K before and after optimization. The introduction of the positive interaction parameters mentioned earlier resulted in a minimum in the Gibbs energy curve corresponding to the exact stoichiometric composition of this phase (Mg_2La). As a result, changes seen in figure 2b are reversed. The molar Gibbs energy of the BCC phase at 950 K is presented in Figure 2-15. Since this curve represents the Gibbs energies of both BCC_A2 and BCC_B2 phases, only a kink is seen corresponding to the stoichiometric composition of the B2 phase (LaMg). This allows the A2 phase to exist at composition ranges close to the La rich part.

Table 2-6 Thermodynamic parameters for the optimized phases

Phase	Model	Parameter	Value, J/mol	Reference
Laves_C15	$(Al,La,Mg)_2(Al,La,Mg)_1$	$G^{\circ}_{Al:Al}$	+43950	Zhou & Napolitano 2006
		$G^{\circ}_{La:La}$	+53790	
		$G^{\circ}_{La:Al}$	+119970	
		$G^{\circ}_{Al:La}$	-150000+11.619*T	
		$G^{\circ}_{Mg:La}$	-26814.7-10.1377*T	Guo *et al.* 2004
		$G^{\circ}_{Mg:Mg}$	+15000	Liang *et al.* 1998
		$G^{\circ}_{La:Mg}$	+15000	Present work
		${}^{0}L_{La,Mg:La}$	+130042	
		${}^{0}L_{Mg:La,Mg}$	+130042	
		${}^{0}L_{Al,Mg:La}$	-30000+10*T	
		${}^{1}L_{Al,Mg:La}$	+35000	
		${}^{2}L_{Al,Mg:La}$	-45000	
BCC_B2	$(Al,La,Mg)_{0.5}(Al,La,Mg)_{0.5}$	$G^{\circ}_{La:Mg}$	-33402.3+9.188*T	Guo *et al.* 2004
		$G^{\circ}_{Mg:La}$	-33402.3+9.188*T	
		$G^{\circ}_{Mg:Mg}$	0	Fabrichnaya *et al.* 2003
		$G^{\circ}_{Al:Al}$	0	Present work
		$G^{\circ}_{La:La}$	0	
		$G^{\circ}_{La:Al}$	-70000	
		$G^{\circ}_{Al:La}$	-70000	
		${}^{0}L_{La,Mg:La}$	-14088.089+31.798*T	
		${}^{0}L_{La:Mg,La}$	-14088.089+31.798*T	
		${}^{0}L_{La,Mg:La,Mg}$	-31250	
		${}^{1}L_{La,Mg:La}$	-31000-15*T	
		${}^{1}L_{La:Mg,La}$	-31000-15*T	
		${}^{1}L_{Mg:La,Mg}$	24500+25*T	
		${}^{1}L_{La,Mg:Mg}$	24500+25*T	
		${}^{0}L_{La:Al,Mg}$	-65000+15*T	
τ	$(Al)_2(Mg)_{0.85}(La)_{0.15}$	G^{f}_{τ}	-33750+5*T	Present work

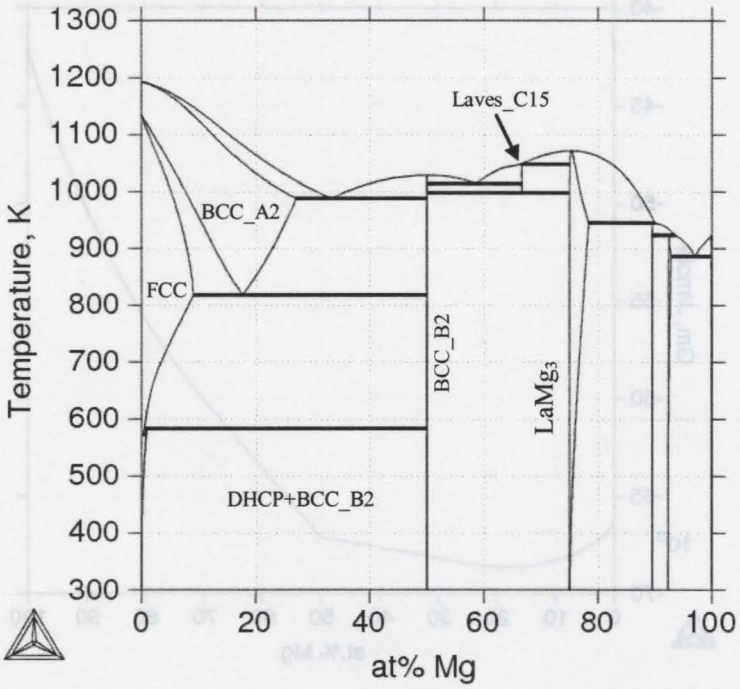

Figure 2-13 La-Mg phase diagram calculated by present thermodynamic description

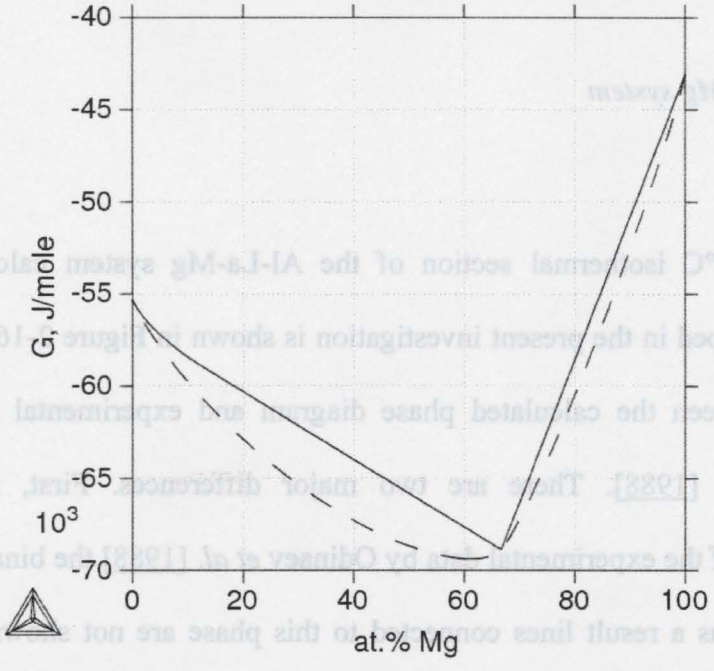

Figure 2-14 Comparison of molar Gibbs energies of the Laves_C15 phase at 1025 K before (dashed line) and after optimization (solid line)

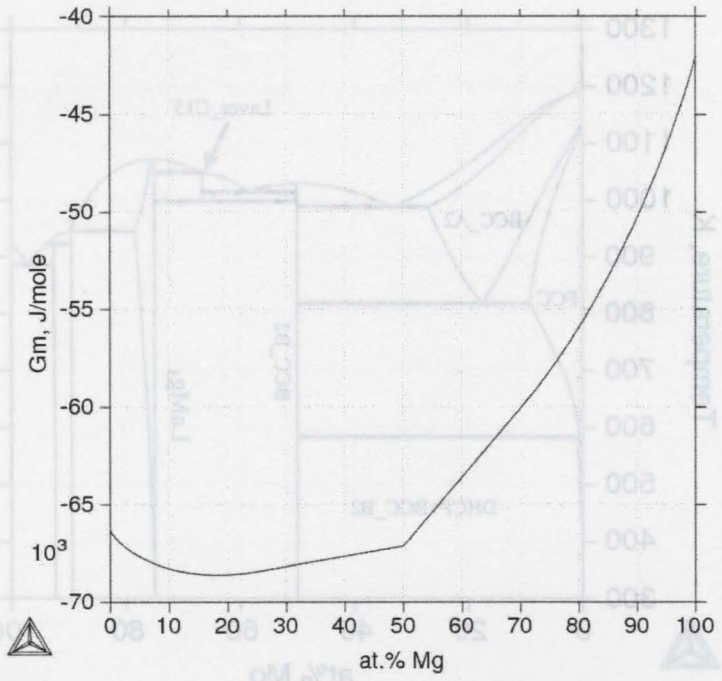

Figure 2-15 Molar Gibbs energy of the BCC_B2 phase at 950 K

2.5.7.2 Al-La-Mg system

The 400°C isothermal section of the Al-La-Mg system calculated using the database developed in the present investigation is shown in Figure 2-16. There is a good agreement between the calculated phase diagram and experimental data reported by Odinaev *et al.* [1988]. There are two major differences. First, in the graphical representation of the experimental data by Odinaev *et al.* [1988] the binary phase $LaMg_{12}$ is ignored and as a result lines connected to this phase are not shown. Second, in the calculated isothermal section the homogeneity range of the Laves_C15 phase terminates at about 16.7 at.% Al by a three phase region while Odinaev *et al.* [1988] extended the

homogeneity range of the Laves_C15 phase to reach the binary La-Mg phase diagram. However, their interpretation is not in compliance with the binary La-Mg phase diagram where the $LaMg_2$ Laves phase is not stable at this temperature.

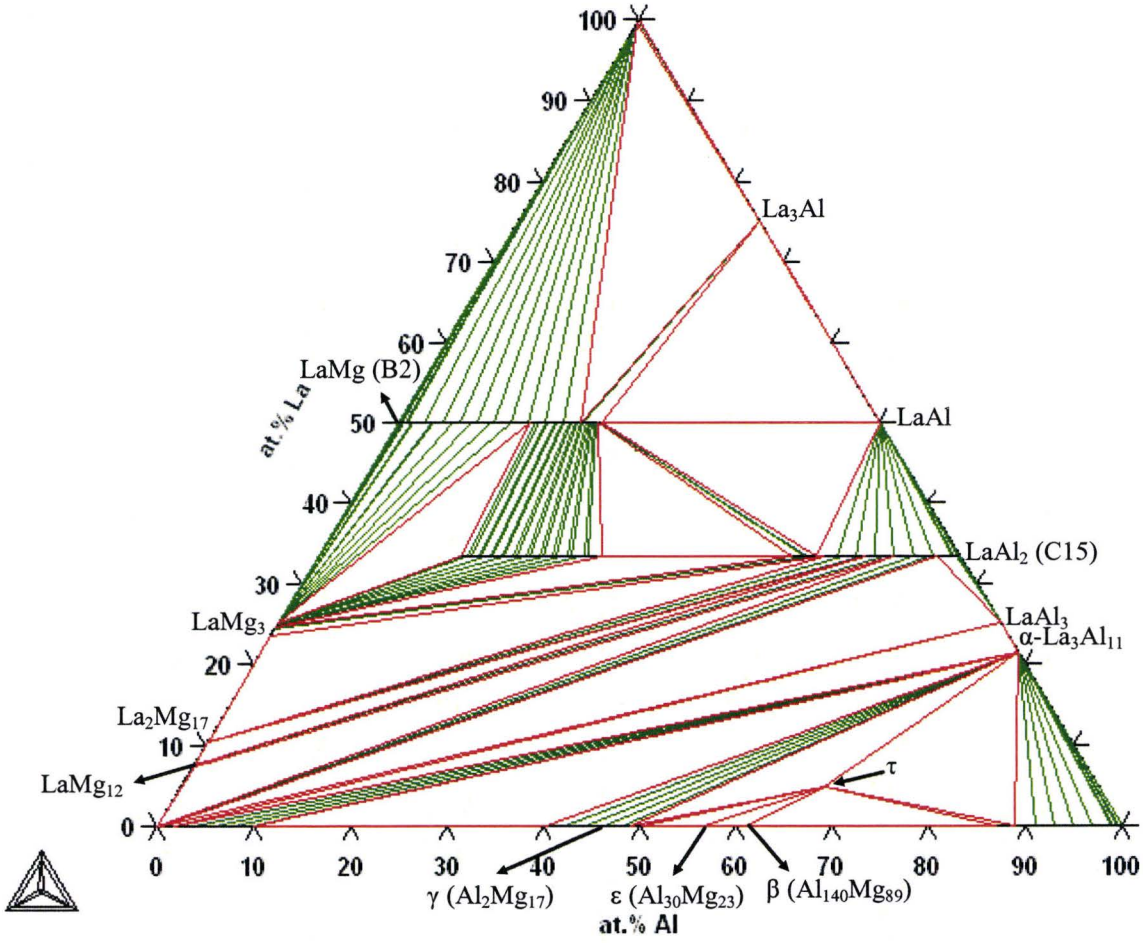

Figure 2-16 Calculated 400°C isothermal section of the Al-La-Mg system

From the 400°C isotherm it is apparent that the homogeneity range of the Laves phase is interrupted by a miscibility gap. This gap is better depicted in Figure 2-17 which

shows a vertical section extending from the $LaMg_2$ phase in the binary La-Mg system to the $LaAl_2$ phase in Al-La system. The miscibility gap appears below 994 K and as mentioned, its position at 400°C compares well with the reported data by [Odinaev *et al.* 1988]. The homogeneity range of the Laves phase is complete in the temperature range of 998 K – 1048 K where it is stable in the binary La-Mg system.

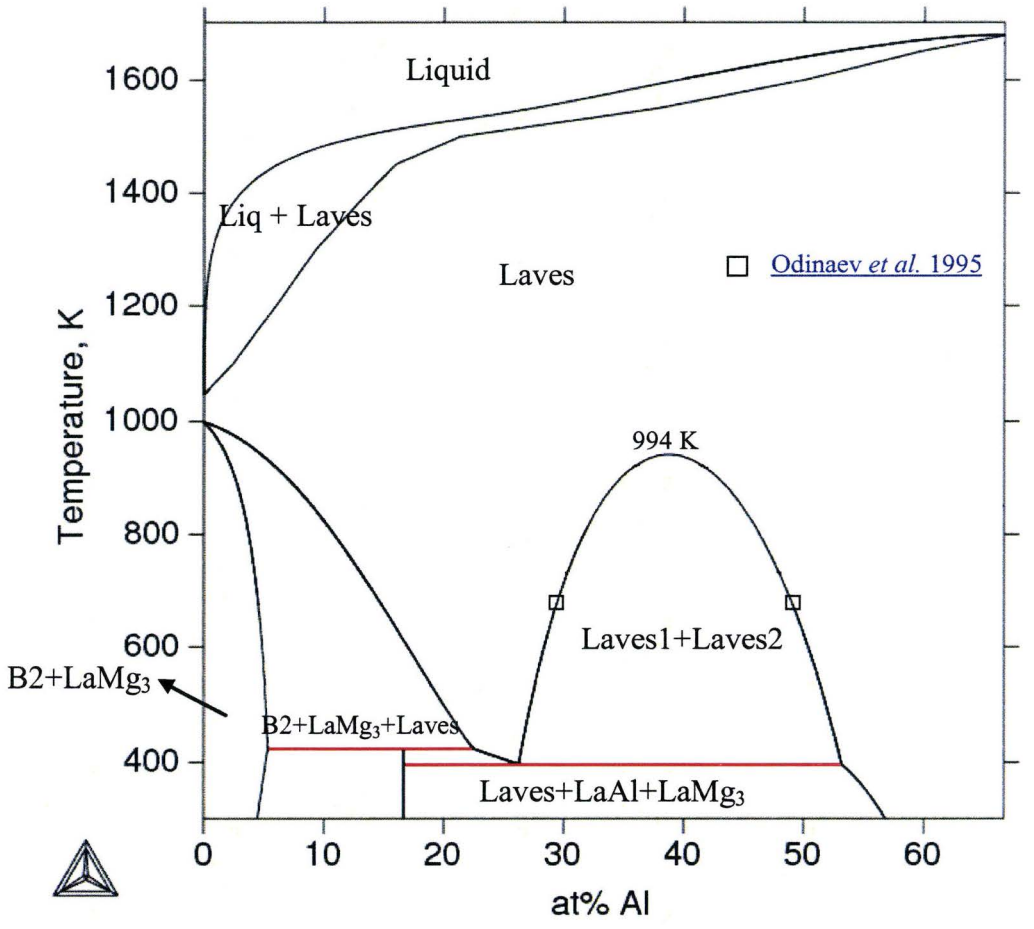

Figure 2-17 Calculated vertical section $LaMg_2$-$LaAl_2$

The pseudobinary sections reported by Odinaev and Ganiev [1995] were compared to the computed results. As an example, calculated vertical section through the ternary Al–La-Mg system containing pure Al and the ternary phase τ is shown in Figure 2-18. A major discrepancy is observed between the calculated and experimental results. It is caused by the presence of the α-La_3Al_{11} phase in the calculated results which rules out a pseudobinary section. More importantly, a high temperature liquidus line which is hundreds of degrees higher than that measured by Odinaev and Ganiev [1995] has appeared associated with the formation of this phase. It is crucial to realize that the formation of the α-La_3Al_{11} phase is predicted completely based on the binary data for the Al-La system and has not been affected by the modeling of the ternary system.

Similar papers are published by Odinaev *et al.* for Al-Mg-Sc [1991] and Al-Mg-Ce [1996] ternary systems. Grobner *et al.* [1999, 2002] optimized these two systems. When comparing their results with the vertical sections of Odinaev *et al.*, Grobner *et al.* also found that these sections were not pseudobinary and calculated liquidus lines were positioned at considerably higher temperatures. To resolve this issue, Grobner *et al.* [1999, 2002] performed a DTA experiment which confirmed the presence of the high temperature liquidus.

The guidelines set by Grobner *et al.* [1999, 2002] are followed to examine the liquidus temperature of two alloys which belong to the Al-τ section shown in Figure 2-18. The liquidus temperatures found in the DTA experiment are indicated in that figure. A perfect match of measurement and calculation is seen at the melting point of

alloy A60 (60 wt.% Al) and a reasonable agreement is achieved for alloy A70 (70 wt.% Al). These agreements confirm the results of the present optimization.

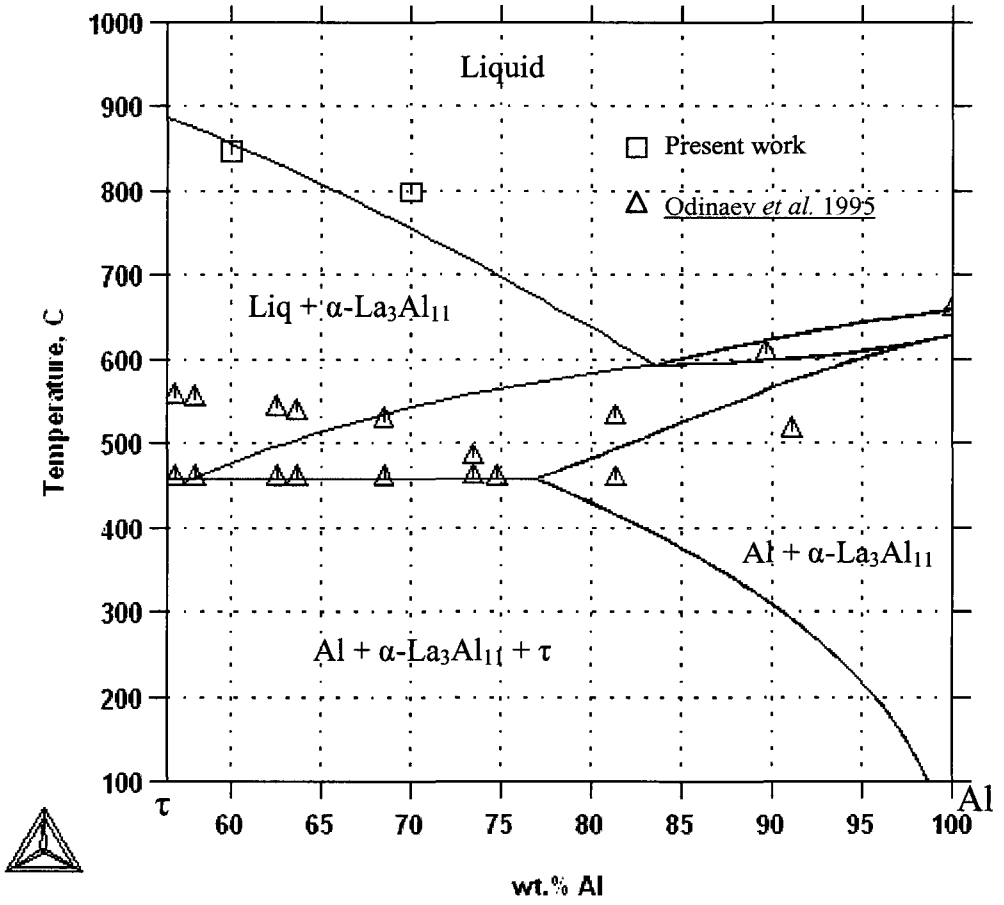

Figure 2-18 Calculated vertical section Al-τ. Experimental data are also indicated on the graph

Since the alloy specimens had not been equilibrated prior to DTA experiment, the rest of the peaks cannot be associated with the equilibrium phase diagram. Instead, they have to be interpreted based on the Scheil calculations [Boettinger *et al.* 2007]. Both alloys follow the same solidification path, only the temperatures of some of the reactions

are different (Table 2-7). The calculated dH/dT vs. T curves for Scheil condition are shown in Figure 2-19.

Table 2-7 Solidification path of alloys A60 and A70 predicted by Scheil calculations

No	Reaction	Temperature (°C)	
		A60	A70
1	$L \rightarrow \alpha\text{-}La_3Al_{11}$	855	753
2	$L \rightarrow \alpha\text{-}La_3Al_{11} + Al$	476	543
3	$L + \alpha\text{-}La_3Al_{11} \rightarrow Al + \tau$	458	
4	$L \rightarrow \beta + Al + \tau$	450	

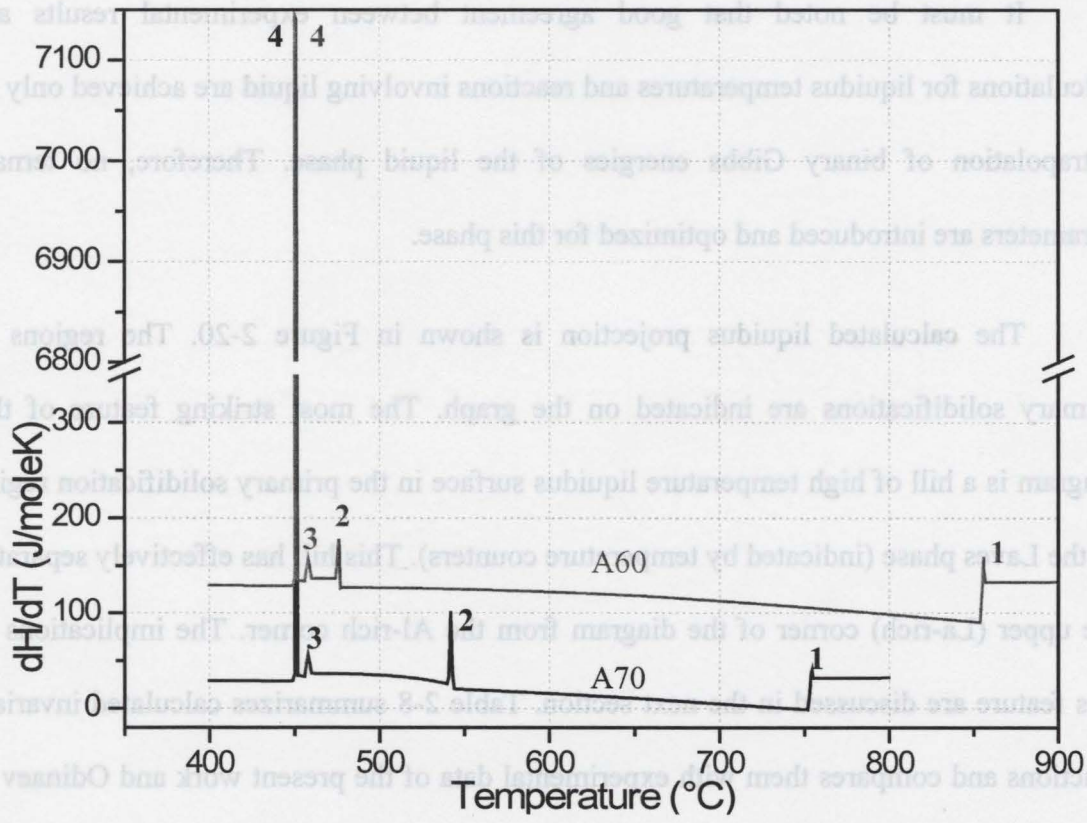

Figure 2-19 dH/dT obtained from the enthalpy–temperature predictions for A60 and A70 alloys computed using optimized data of the present work for Scheil condition. The curve for A60 is shifted up 100 J/moleK for clarity

A good match is perceived between the dH/dT curve of the A70 alloy and the DTA results (Figure 2-9). It can be concluded that the peaks a, b and c are caused by the reactions 1, 2, and 4 of Table 2-7 respectively. The peak corresponding to the reaction 3 is not seen in Figure 2-9 probably because it is masked by the heat effects of reactions 2 and 4. In the case of alloy A60, peak "a" is already associated with the liquidus point (reaction #1). The position and intensity of peak c suggests that it is caused by reaction 4. However, no heat effects are recorded corresponding to reactions 2 and 3. The close proximity of these peaks to the peak associated with reaction 4 can once again be the cause of this phenomenon.

It must be noted that good agreement between experimental results and calculations for liquidus temperatures and reactions involving liquid are achieved only by extrapolation of binary Gibbs energies of the liquid phase. Therefore, no ternary parameters are introduced and optimized for this phase.

The calculated liquidus projection is shown in Figure 2-20. The regions of primary solidifications are indicated on the graph. The most striking feature of this diagram is a hill of high temperature liquidus surface in the primary solidification region of the Laves phase (indicated by temperature counters). This hill has effectively separated the upper (La-rich) corner of the diagram from the Al-rich corner. The implications of this feature are discussed in the next section. Table 2-8 summarizes calculated invariant reactions and compares them with experimental data of the present work and Odinaev &

Ganiev [1995]. The reasonable agreement between the results of experiment and calculations indicates the validity of the optimized data.

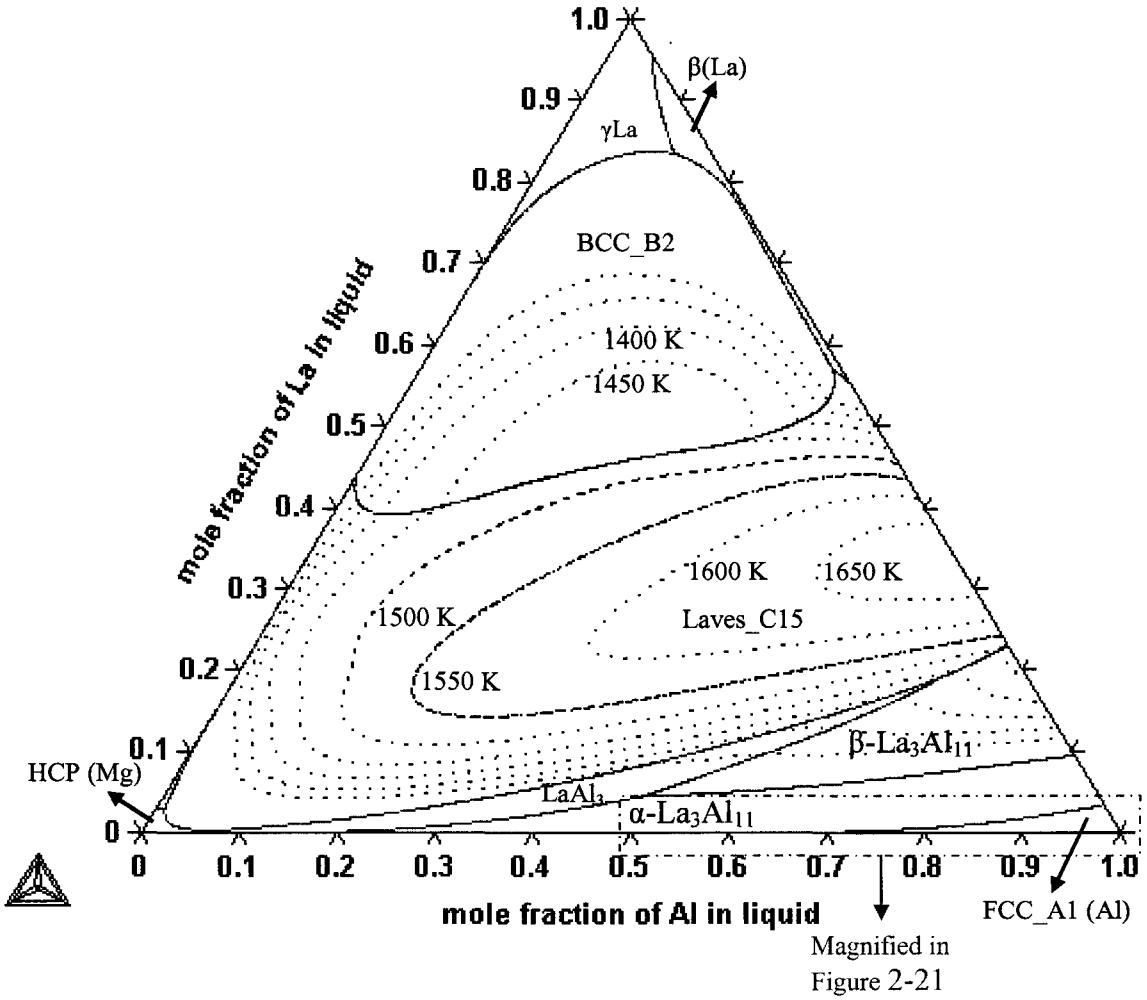

Figure 2-20 Calculated liquidus surface of the Al-La-Mg system

Table 2-8 Calculated invariant reactions in the Al-La-Mg system

Reaction	Calculated			Measured (this work)	Measured [Odinaev & Ganiev 1995]		
	T (°C)	Composition of liquid (at.%)		T (°C)	T (°C)	Composition of liquid (at.%)	
		Al	La			Al	La
$L + \alpha\text{-}La_3Al_{11} \rightarrow Al + \tau$	458.5	65	0.06		459	81	2.8
$L \rightarrow Al + \tau + \beta$	450	63.8	0.04	445	433	63	1.1
$L + \alpha\text{-}La_3Al_{11} \rightarrow \gamma + \tau$	452	56.4	0.03		434	49.1	2.9
$L \rightarrow Al_{12}Mg_{17} + \tau + \beta$	449.4	57.6	0.03		436	55.5	0.9
$L \rightarrow \gamma + HCP\_A3 + \alpha\text{-}La_3Al_{11}$	436	31	0.008		432	30.2	2.8
$L + \gamma La \rightarrow BCC\_B2 + \beta La$	649	12.5	83.8				
$L + Laves\_C15 \rightarrow BCC\_B2 + LaAl$	854	42	57				
$L + LaAl \rightarrow BCC\_B2 + La_3Al$	521.5	22.5	77.2				
$L \rightarrow BCC\_B2 + \beta La + La_3Al$	519	21.2	78.5				
$L \rightarrow LaAl_3 + Mg + \alpha\text{-}La_3Al_{11}$	554.5	16.6	0.07				
$L \rightarrow LaAl_3 + Mg + Laves\_C15$	613	7	0.3				
$L \rightarrow LaMg_{12} + Mg + Laves\_C15$	608.5	0.8	3.1				
$L \rightarrow LaMg_{12} + La_2Mg_{17} + Laves\_C15$	650	0.3	6				
$L \rightarrow LaMg_3 + La_2Mg_{17} + Laves\_C15$	675	0.7	10				
$L \rightarrow \beta\text{-}La_3Al_{11} + \alpha\text{-}La_3Al_{11} + LaAl_3$	915	49	4.5				
$L \rightarrow \beta\text{-}La_3Al_{11} + Laves\_15 + LaAl_3$	1133	70	17				

2.5.7.3 Al (FCC) – LaMg (BCC_B2) two phase material

The primary objective of optimizing the Al-La-Mg system was to examine the possibility of fabricating the two phase FCC - BCC_B2 material by casting. Primary solidification regions exist for both Al and LaMg phases (Figure 2-20). It means that by choosing a proper composition, the solidification can start by the precipitation of one of these phases from the melt. However, the formation of the primary phase will not be followed by the solidification of the other desired phase. This is mainly because these two regions are separated by the high temperature liquidus surface of the Laves phase. According to the Scheil calculations, the solidification paths of alloys belonging to the primary region of the BCC_B2 phase will fall in the temperature "valleys" (solid lines in Figure 2-20) above the primary region of the Laves phase. On the other hand, solidification paths of alloys reside in the primary region of Al will end up in valleys below the primary region of the Laves phase. The primary solidification regions of these two phases (Al and B2) are examined in detail to prove these statements.

The magnified primary solidification region of Al is shown in Figure 2-21. The temperature contours are superimposed on the diagram. According to the Scheil-Gulliver calculations, depending on the composition within this region two solidification paths may be followed. They are presented in Figure 2-22. These paths are marked in Figure 2-21 along with the invariant reaction points. A variety of phases (τ, $Al_{140}Mg_{89}$, and/or α-La_3Al_{11}) may appear in the final cast microstructure of alloys belonging to the primary region of Al; the B2 phase is not one of them.

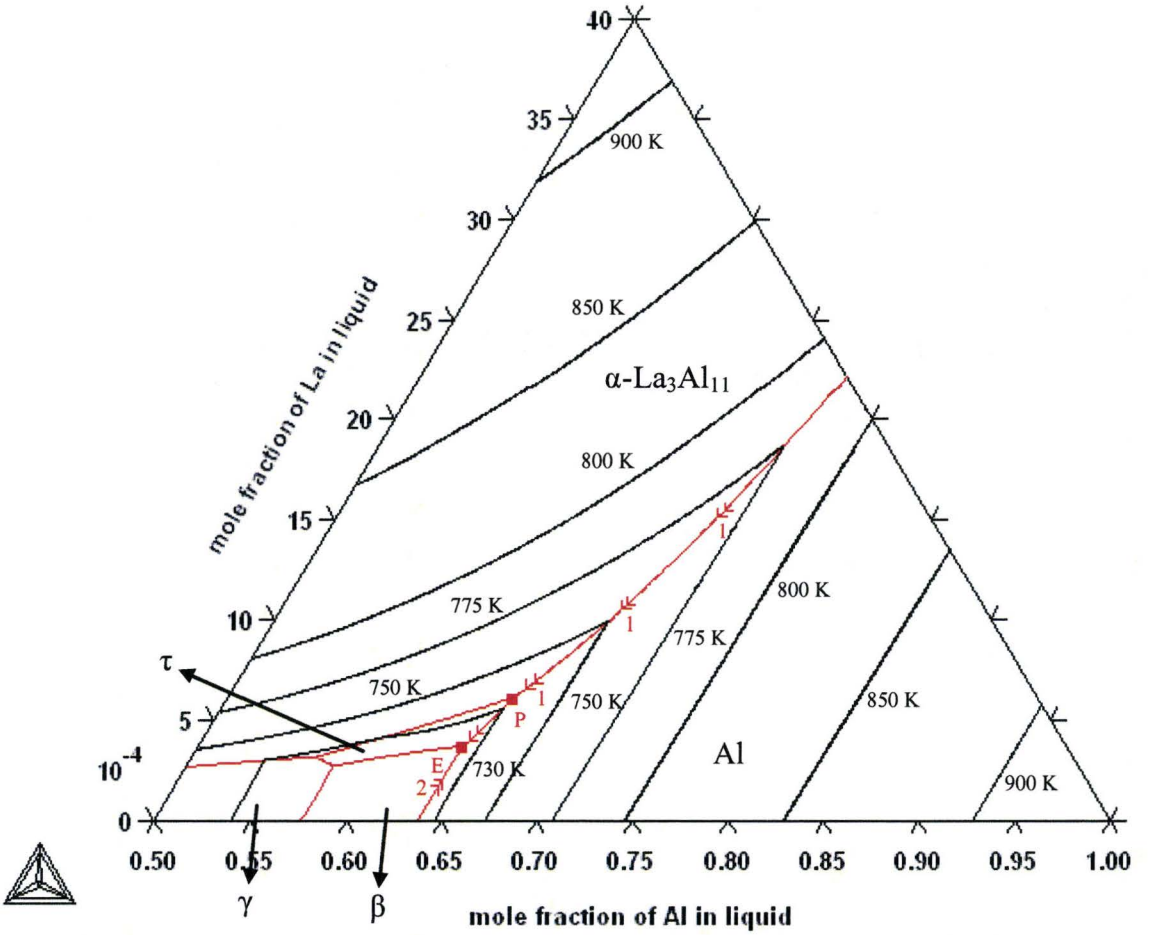

Figure 2-21 Primary solidification region of Al

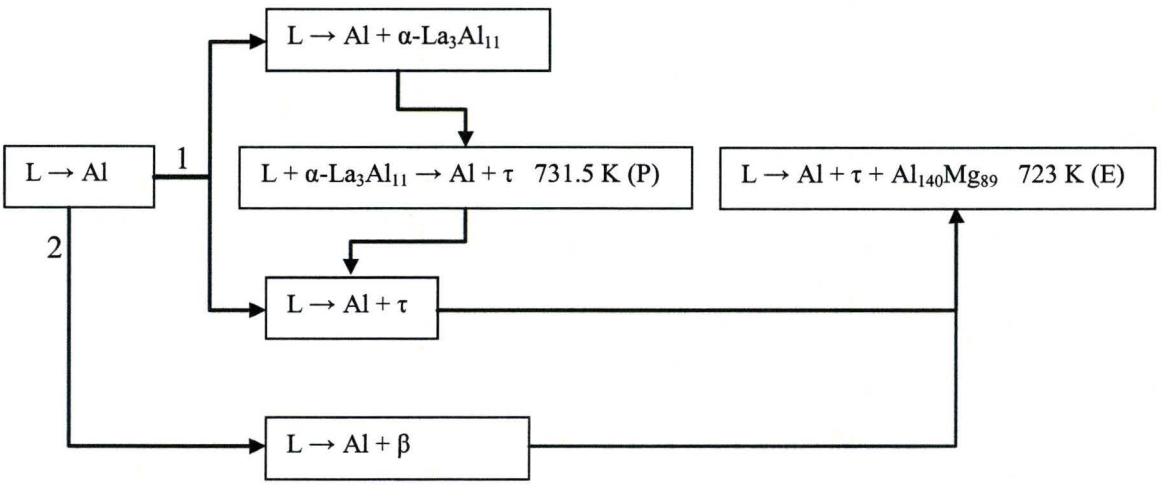

Figure 2-22 Solidification paths of alloys in the primary region of Al predicted by Scheil calculations

The primary solidification region of the BCC_B2 phase is magnified in Figure 2-23 and the possible solidification paths are given in Figure 2-24. It is seen that none of these paths results in the formation of Al. It is worth mentioning that in the third path liquid becomes depleted of Al in the first two steps and the last step occurs according to the binary La-Mg system.

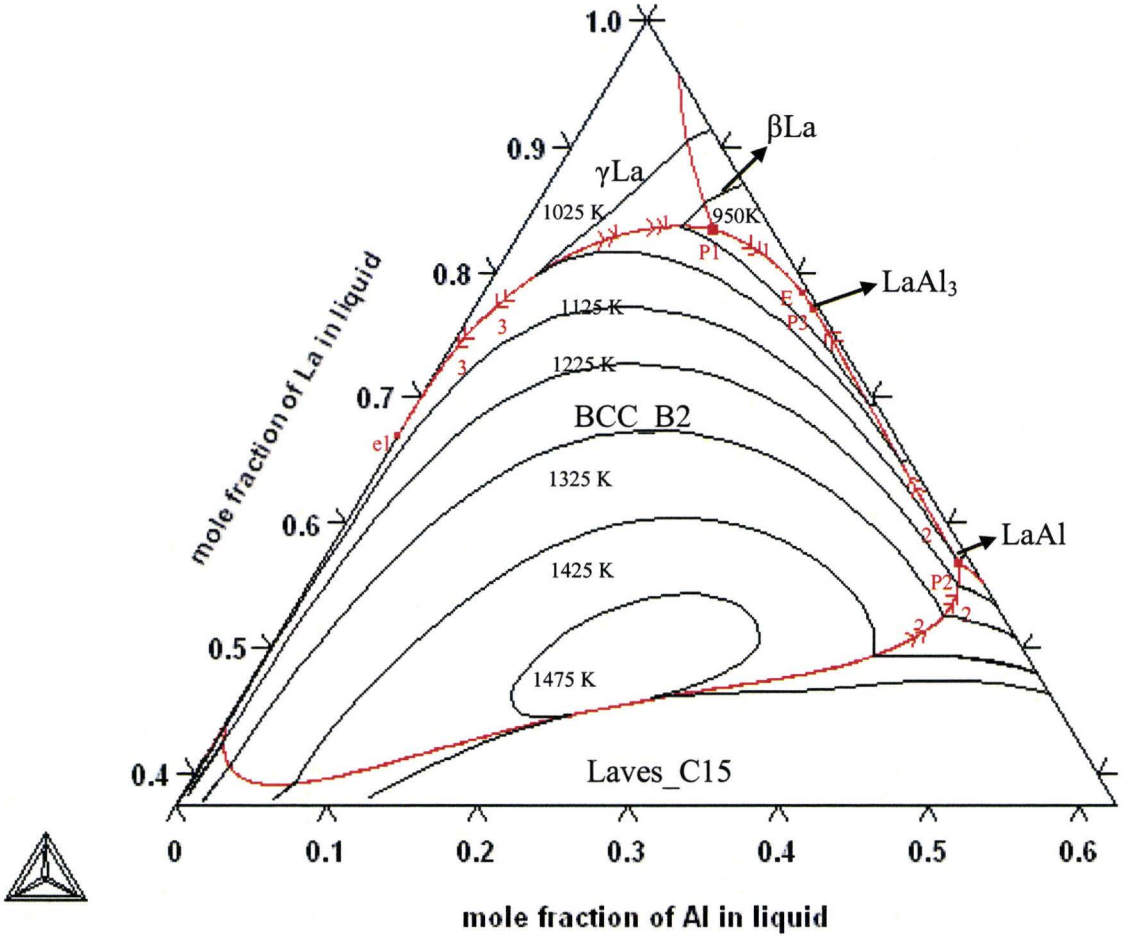

Figure 2-23 Primary solidification region of the B2 phase

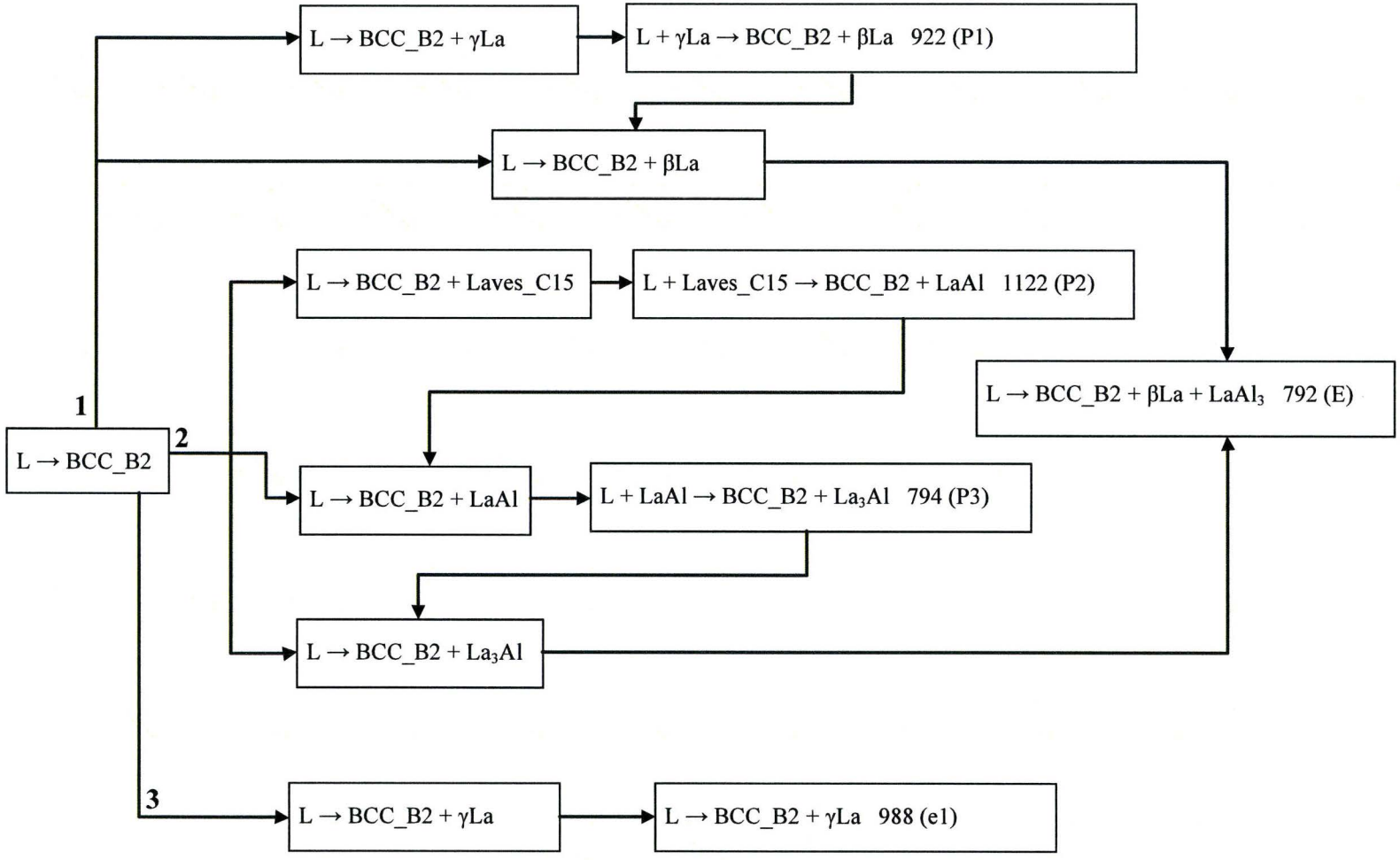

Figure 2-24 Solidification paths of alloys in the primary region of B2 phase predicted by Scheil calculations

In principle it is not necessary to start from the primary solidification region of one of these two phases in order to have it at the final stage. Even if the solidification starts with formation of another phase, the desirable microstructure can still be achieved if both Al and B2 phases form as a result of the path followed. In the case of the Al-La-Mg system, no matter what the alloy's composition is, the mutual formation of Al and B2 phases is inhibited by the high temperature surface of primary solidification of the Laves phase.

Scheil calculations ruled out the fabrication of the Al/B2 material by low cooling rate casting processes. The possibility of the formation of such material by processes involving high cooling rates is also examined. For this purpose, several alloys corresponding to the primary solidification region of the Al are examined. The driving forces for the onset of precipitation (DGM) of several intermetallic phases including the B2 phase are evaluated. To perform such calculations, the phases whose driving forces are needed have to be excluded from the equilibrium. This is because the driving forces for the onset of precipitation of equilibrium phases are always equal to zero [Purdy *et al.* 2004]. Only liquid and Al are allowed to participate in the equilibrium. Such special permission is given to aluminum because no matter how fast molten Al is cooled, solid aluminum forms with only a few degrees of supercooling. The result of such calculations for an Al - 3 at.% Mg - 2 at.% La alloy is shown in Figure 2-25. The situation is once again grim. It is seen at any given superercooling there are always phases with higher potency of formation than the sought after BCC_B2 phase (phases with positive value of DGM are expected to nucleate).

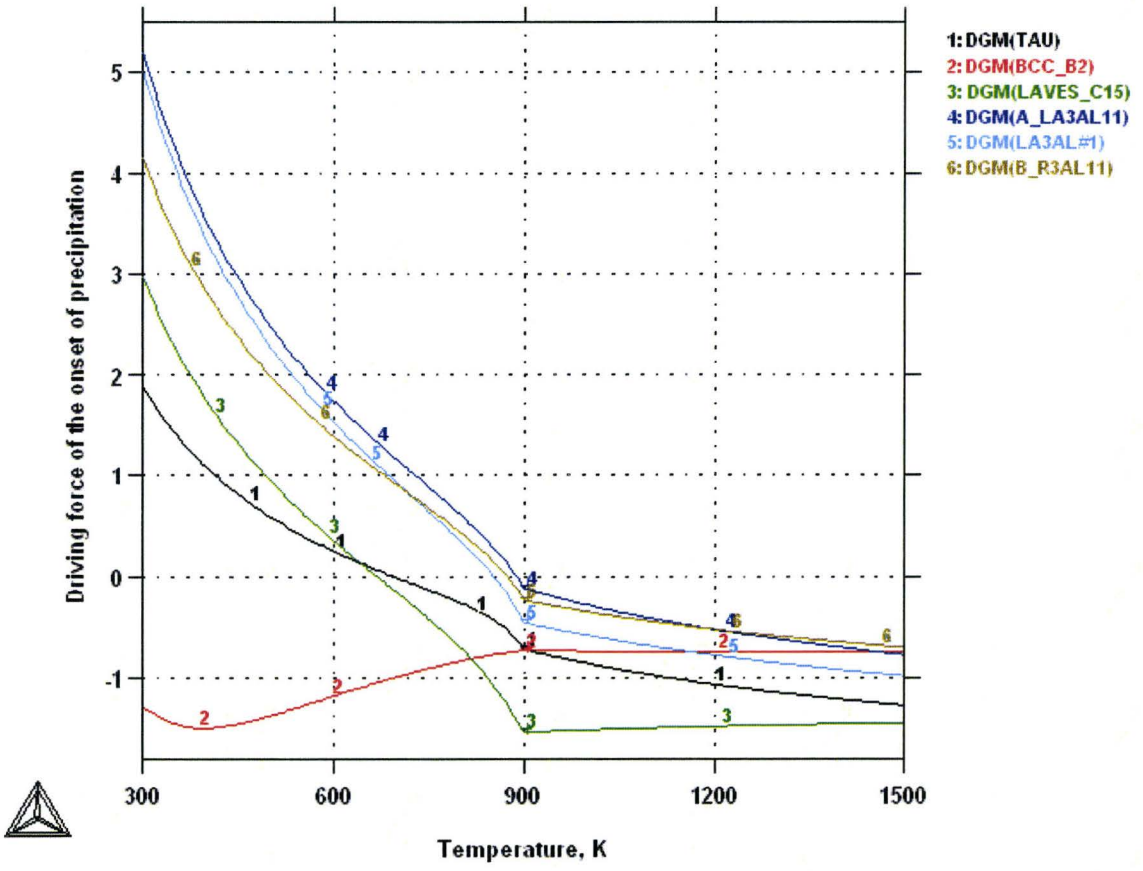

Figure 2-25 Driving forces of the onset of precipitation of intermetallic phases following the formation of the primary Al

2.5.8 Other Al-Mg-R systems

The Al-Mg-(Sc, Ce) systems are optimized by Grobner *et al.* [1999, 2002]. Thermodynamic optimizations of the Al-Mg-(Gd, Dy, Ho, Er) system have been carried out by Cacciamani *et al.* [2002, 2003]. In all these systems, the high temperature liquidus surface of the primary solidification region of the Laves_C15 phase is present. The Al

and B2 phases are completely separated by this region which once again diminishes the possibility of fabricating the intended material.

Although it was disappointing to realize that the fabrication of the FCC/B2 material is impossible, this prediction in fact benefited the industrial supporter of this project, Novelis Inc., in the sense that it precluded them from expensive, time consuming, and futile attempts to fabricate such an alloy.

3 Small additions of cerium and lanthanum

3.1 6xxx series Al alloys

The 6xxx series Al alloys are a family of wrought heat-treatable alloys. The main alloying elements are Mg and Si which form Mg_2Si precipitates during age hardening. Other major alloying elements include Cu and Mn. Copper is usually added to the alloy in order to improve strength of the alloy by forming θ (Al_2Cu) and Q ($Al_3Cu_2Mg_9Si_7$) phases in the age hardening step. Mn is sometimes added to the alloy to modify Fe-bearing intermetallics.

In North America, AA6111 alloy is being considered for outer body panels since its combination of good formability, post heat treatment strength and surface finish is of value [Miller *et al.* 2000]. The typical composition of this alloy is shown in Table 3-1.

Table 3-1 Chemical composition of AA6111 alloy (wt.%)

Mg	Si	Fe	Mn	Cu	Al
0.7	0.7	0.25	0.25	0.7	bal.

The composition of the alloy chosen for this investigation is based on the commercial grade AA6111 with some modifications. These modifications were done to create an alloy with larger amounts of unmodified Fe-containing intermetallics. It means a relatively high amount of iron and no manganese. This would magnify the effect of R metals if such effect exists. The composition of the reference alloy used in this research is given in Table 3-2.

Table 3-2 Chemical composition of the reference alloy (wt.%)

Mg	Si	Fe	Cu	Al
0.7	0.7	0.45	0.2	bal.

In comparison with AA6111 alloy, the amount of copper is also decreased. High concentrations of Cu results in the formation of the θ (Al_2Cu) phase during solidification. By decreasing the amount of copper, such an unnecessary complication will be avoided.

A solidification sequence and amounts of constituent phases at relatively low cooling rates can be predicted by using the Scheil-Gulliver method implemented in the SCHEIL module of Thermo-Calc. In order to perform such calculations, a multicomponent thermodynamic database dedicated to Al alloys (ALCAN database) developed at McMaster University is employed. The results of these calculations are shown in Figure 3-1 and Figure 3-2. The predicted reactions and their corresponding temperatures are:

1. Liquid → Al (dendritic network) 651°C
2. $L \rightarrow Al + Al_{13}Fe_4$ 632°C - 617.5°C
3. $L + Al_{13}Fe_4 \rightarrow Al + Al_8Fe_2Si$ (α) 617.5°C
4. $L \rightarrow Al + Al_8Fe_2Si$ (α) 617.5°C – 598°C
5. $L + Al_8Fe_2Si$ (α) → $Al + Al_5FeSi$ (β) 598°C
6. $L \rightarrow Al + Al_5FeSi$ (β) 598°C - 573.5°C
7. $L \rightarrow Al + Al_5FeSi$ (β) $+ Mg_2Si$ 573.5°C - 550°C
8. $L \rightarrow Al + Al_5FeSi$ (β) $+ Mg_2Si + Si$ 550 °C – 502°C
9. $L \rightarrow Al + Al_5FeSi$ (β) $+ Mg_2Si + Si + Al_2Cu$ (θ) 502°C

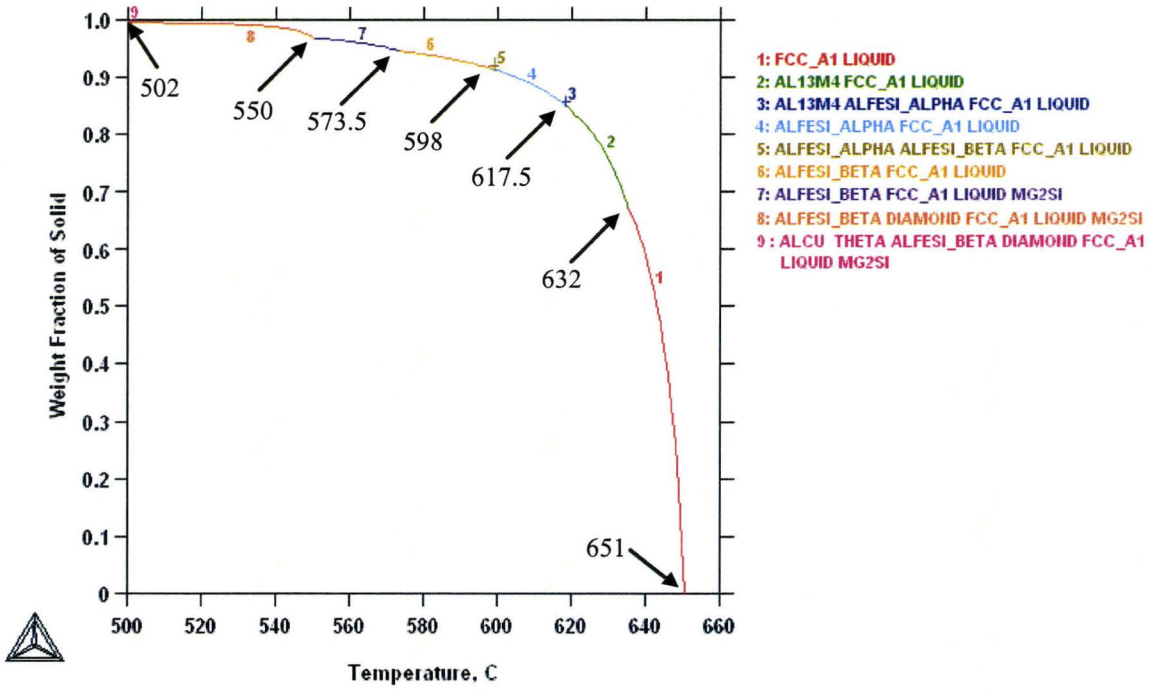

Figure 3-1 Solidification sequence of the reference alloy calculated by Thermo-Calc

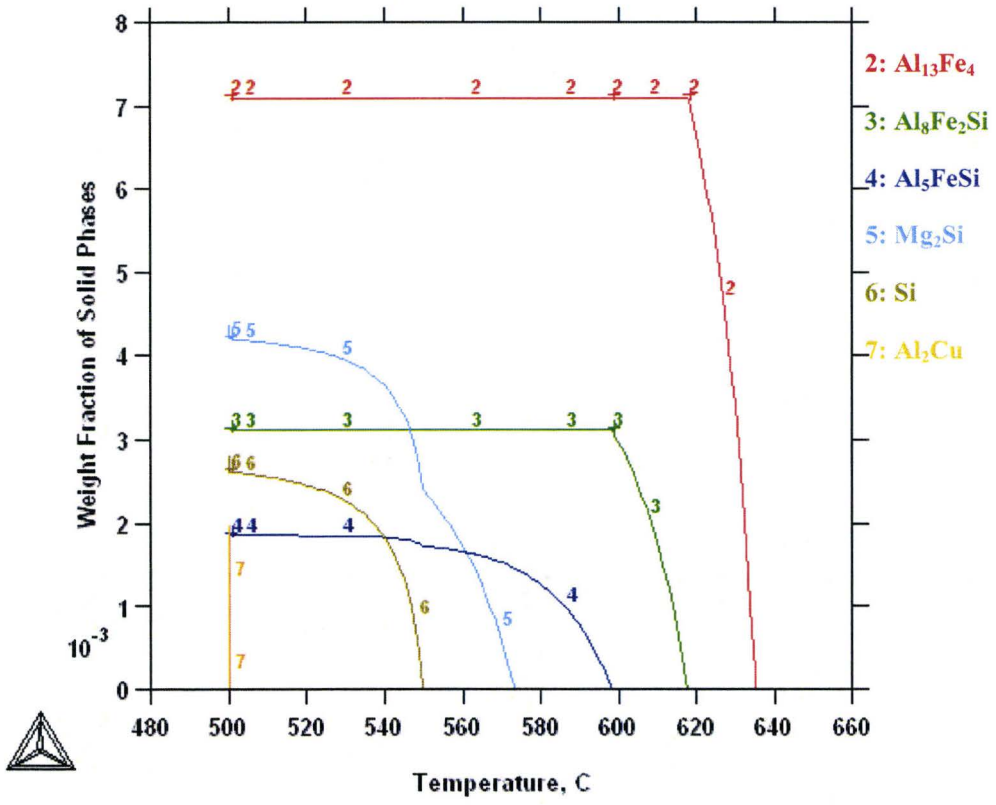

Figure 3-2 Amount of solid phases formed during solidification of an alloy with the composition given in Table 3-2

According to this prediction, three types of Fe-bearing intermetallic phases plus Mg_2Si, Al_2Cu, and pure silicon form in interdendritic spaces of Al. In industrial practice, the forming procedure (stamping, hemming, etc.) is carried out after rolling the sheet to the final gauge and solutionizing. Mg_2Si and Al_2Cu particles will dissolve into the Al matrix during solution heat treatment and have no adverse effect on the formability of the alloy sheet. Fe-bearing intermetallics however, cannot be removed by heat treatment and are detrimental to the formability of the alloy.

In the following sections first the effect of these particles on the formability will be discussed and a less harmful particle from the formability viewpoint will be characterized. Then ways by which cerium and lanthanum additions might modify Fe-bearing intermetallics to such less harmful variation will be explained.

3.2 Formability and failure modes

The formability of a material is the extent to which it can be deformed in a particular process before the onset of failure. Failure may occur in a variety of ways [Parker 1989]:

- The workpiece may fracture.
- There may be severe localized deformation (necking).
- The appearance of the product may be unsatisfactory (for example, surface imperfection due to Luders bands, galling …).
- The workpiece may not retain the shape imposed by a die.

Since the term failure does not have a unique interpretation, formability can not be unambiguously characterized by a single value. Instead, the formability of an alloy must be defined according to the type of failure the material endures in a certain forming process. For example, 5xxx series Al alloys are not suitable for outer body panels in spite

of their acceptable mechanical properties, since they exhibit poor appearance due to Luders band formation during stamping.

A common type of failure in stamping of Al alloy sheets for automotive body panels is a localized necking, which happens when the material fails to deform uniformly and strain concentrates in a small region of the workpiece. It is governed largely by material properties such as work hardening and strain rate hardening and depends critically on the strain path of the forming process. Forming limit diagrams (FLD) [Embury & Duncan 1981, Glover *et al.* 1977] are usually constructed for alloys to show the strains at which localized necking is first observed. A generic FLD is presented in Figure 3-3.

To prepare such a diagram for a material, tests are performed on rectangular sheet specimens with different widths in order to obtain strain paths for biaxial stretch, plane strain, tension, deep drawing (in-plane pure shear) and intermediate strain paths. The test specimens are stretch-formed over a hemispherical tool. A grid is etched on the test specimen before pressing, and the strains are measured in the region where necking has taken place. The major and minor principal strains are measured and the measured values are plotted in a diagram with the minor principal strain as abscissa and the major principal strain on the ordinate.

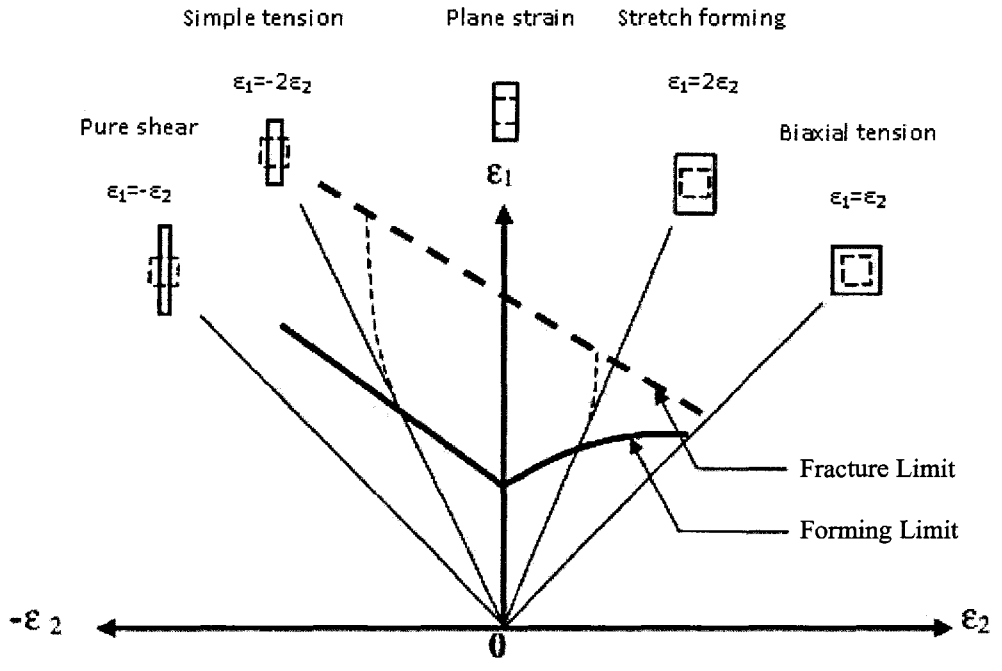

Figure 3-3 Schematic forming limit and fracture limit diagrams

A fine dispersion of small non-shearable particles may increase the strain necessary for failure by localized necking since such construction will result in a more uniform distribution of strain throughout the sheet. Fe-bearing intermetallic particles are in fact non-shearable. However, they are coarse (> 1 μm in size) and hence do not contribute to extending the uniform deformation. The size of these intermetallic particles becomes an important factor in the failure of a workpiece by ductile fracture.

Al alloy sheets can also fail by ductile fracture. Although, fracture usually occurs at larger strains than localized necking (Figure 3-3), it is important in processes such as biaxial stretching, small radius bends, severe drawing, ironing and stretching near notches or sheared edges [Hecker 1975, Morris *et al.* 1982]. The automotive body panels are

usually two layer structures in which an outer layer is joined to an inner layer by hemming [Davies 2003]. Such operation involves small radius bending of the outer panel. The sheet that is to be used for the outer panel must meet bendability criteria needed for a successful hemming. During bending of wide sheets (width/thickness > 10), the strain in the width of the sheet is negligible and hence the strain regime in this process is actually plane strain [Caddell & Hosford 1993]. However since the strain is concentrated in a small region of the material, the maximum bending strain cannot be indicated by FLD (as mentioned, FLD provides the limit for uniform deformation) and fracture limit must be considered instead.

Ductile fracture occurs either by concentration of strain in narrow shear bands or by nucleation and linking of microscopic voids. Second phase particles such as iron-containing intermetallics contribute to the ductile fracture by acting as sites of void nucleation. In the next section, characteristics of a particle which enhance its ability to initiate voids are discussed.

3.2.1 Void nucleation at the brittle particles

During deformation, brittle second phase particles such as the Fe-bearing intermetallics in Al alloys are acting as barriers to dislocation movement. Dislocations either pile-up behind these particles or leave debris around the particles if they continue moving in the slip plane or cross-slip around the particles. Both dislocation pile-ups and

dislocation debris will result in a high strain concentration in the vicinity of the particles. If not relaxed, this local plastic-strain concentration can lead to the void nucleation by decohesion of the particle/matrix interface or cracking of the particles.

The most important characteristics of a particle that affects its ability to initiate a void is its size. It is observed experimentally [Llorca *et al.* 1993, Brechet *et al.* 1991, Caceres & Griffiths 1996] that the larger the particle the lower the strain needed to initiate voids. One of the reasons behind this inverse relationship is that these intermetallic phases are brittle and the mechanism of brittle fracture is based on pre-existing flaws in the material, the probability of finding a flaw with the critical size is higher for larger inclusions [Cox & Low 1974]. Moreover, a higher strain concentration in front of particles is expected when second phase particles are coarser. This is because coarser particles mean that for a given volume fraction, the particle spacing will be greater which leads to a less tortuous path for dislocations and a larger dislocation pileup in front of these particles.

The inverse proportionality of void nucleation strain and particle size is predicted by several models. Gurland and Platteau [1963] considered void nucleation in terms of an energy balance. They assumed that cavitation will not occur unless the elastic energy released (ΔE_{el}) by removing the stress (or some fraction of it) from the particle is at least equal to work needed to create new surfaces (ΔW) associated with the void. For a spherical inclusion it yields:

$$\left(\frac{4}{3}\pi r^3\right)\left(\frac{1}{2}E\varepsilon_n^2\right) \geq 4\pi r^2\gamma \qquad 3\text{-}1$$

where r is the particle radius, E is the Young's modulus of the particle, ε_n is the void nucleation energy, and γ is the energy of the surface formed by cavitation. The left hand side term is the ΔE_{el} and the right hand side term represents ΔW. A rearrangement of the equation 3-1 gives:

$$\varepsilon_n \geq \sqrt{\frac{6\gamma}{rE}} \qquad 3\text{-}2$$

Tanaka *et al.* [1970] speculated that the above energy criterion is satisfied for all but the smallest particles (less than 25 nm) almost as soon as yield occurs. Since, in many instances, inclusions of more than one hundred times this size have been observed to remain coherent to the matrix after strains of more than one hundred times the yield strain have been applied it must be concluded that the energy requirement is only a necessary one and separation requires that the interfacial strength is reached at some local point. Following a mechanism of work hardening proposed by Ashby [1966] the local stress at the particle/matrix interface (σ_{loc}) can be calculated as:

$$\sigma_{loc} = \alpha \frac{\varepsilon r}{2kb} \qquad 3\text{-}3$$

in which α is a constant, b is the burgers vector and k is the length of the dislocation pile up which can be set approximately equal to the half of particle spacing. Voids will form at the particle/matrix interface if σ_{loc} reaches the interfacial strength (σ_c) which gives:

$$\varepsilon_n = \frac{2\sigma_c kb}{r\alpha} \qquad 3\text{-}4$$

This once again shows the inverse relationship between void nucleation strain and particle size. Caceres and Griffiths [1996] used a simple model to describe the cracking of Si particles in cast aluminum alloys which was originally proposed by Brechet et al. [1991] for metal matrix composites. In this model the statistical nature of void nucleation is taken into account by assuming that the particles obey Weibull statistics *i.e.*,

$$p = 1 - \exp\left[\frac{V}{V_0}\left(\frac{\sigma_p}{\sigma_0}\right)^m\right] \qquad 3\text{-}5$$

where p represents the probability of cracking of a particle of volume $V = \frac{1}{6}\pi d^3$, σ_p is the stress in the particle and, $V_0 = \frac{1}{6}\pi d_0^3$, σ_0, and m are constants.

If no plastic relaxation occurs before cracking of particles then σ_p is:

$$\sigma_p = 2.14\mu\alpha\varepsilon^* \qquad 3\text{-}6$$

in this equation α is the aspect ratio of the particle, ε^* is equal to the plastic strain near the particle, and μ is the shear modules of the matrix. By inserting (3-6) in (3-5) the probability of particle cracking is evaluated as:

$$p = 1 - \exp\left[\frac{d^3}{d_0^3}\left(\frac{\mu\alpha\varepsilon^*}{\sigma_0}\right)^m\right] \qquad 3\text{-}7$$

This equation simply shows that larger particles with higher aspect ratio are more prone to cracking.

Elongated second phase particles (platelets or needles) are often seen in the microstructure of structural materials. For these particles, size might not be a correct characteristic and aspect ratio must be considered instead as the parameter affecting void nucleation strain. Acicular particles are in fact considered to be more effective void nucleation sites. Sharp edges of such inclusions act as stress raiser points which aid void nucleation. It is observed that while equiaxed inclusions almost always nucleate voids by interfacial separation, inclusions with large aspect ratio may undergo multiple internal fracturing [Broek 1973, Gammage *et al.* 2004]. The reason for this phenomenon is that the higher the aspect ratio the higher the stress inside the inclusion. Following a treatment by Kelly and Tyson [1965] for fiber reinforced composites, the stress inside a cylindrical inclusion (σ_z) with diameter d embedded in a matrix with shear strength of τ_m subjected to a tensile stress in the direction of the inclusion's axis can be estimated as:

$$\sigma_z = 4\tau_m \frac{z}{d} \qquad 3-8$$

where z is the distance in the direction of inclusion's axis. It is seen that this stress increase with aspect ratio of particle and when this stress reaches the fracture stress of the inclusion, it breaks.

Another disadvantage of non-equiaxed particles is that plastic relaxation processes which result in lowered strain concentration are less efficient when elongated particles exist [Lilholt 1993]. For example, the prismatic punching of dislocation loops out of an elongated particle will need a dislocation with the length equal to the length of the particle. Another mechanism which can be activated in the presence of elongated

particles is double cross slip. The sequence by which this mechanism works is shown schematically in Figure 3-4. As seen, this mechanism is also less efficient because one of the prismatic loops is blocked by the particle.

The strength of the interface between the particle and the matrix plays an important role where void nucleation through decohesion is viable. Segregation of impurities on the particle/matrix interface can decrease the interfacial strength and lead to lower void nucleation strength. Second phase particles with faceted interfaces will also have low interfacial strength. Voids can readily form at such interfaces under tensile stresses. In contrast, void nucleation might shift to the matrix in the vicinity of a particle when the particle/matrix interface is strong [Faleskog & Shih 1997].

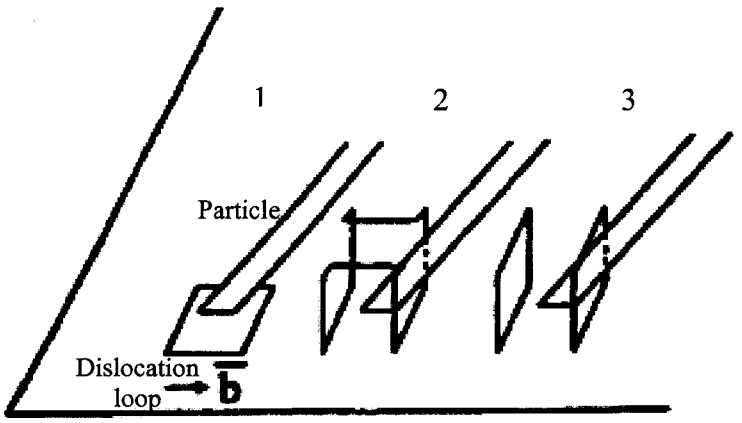

Figure 3-4 Double cross-slip at elongated particles [Lilholt 1993]

Intermetallic particles are generally brittle in nature; however, it is undeniable that there are levels of brittleness among different types of intermetallics. Having less brittle

particles will postpone the fracture to higher strains. Scarce information available on the ductility of individual intermetallic phases precludes the possibility of a comparison.

So far the properties of intermetallic phases as individual particles were considered. When a population of intermetallic particles embedded in a matrix is present two other factors must be taken into account: the volume fraction and the distribution of particles. For a given intermetallic particle size, a higher volume fraction of second phase particles means that higher number of particles are spread throughout the matrix. Since void nucleation is a statistical event, it is apparent that having higher number of potential void nucleation sites will result in a lowered void nucleation strain. This fact is firmly supported by experimental observations [Weck *et al.* 2008, Sarkar *et al.* 2001, Babout *et al.* 2001, Maire *et al.* 1995]. The inhomogeneous nature of the second phase particle distribution significantly affects the void nucleation process. The particle rich areas of an alloy act as weak spots which lower the void nucleation strain and accelerate the fracture process [Gammage *et al.* 2005, Kang *et al.* 2007, Poruks *et al.* 1998].

Upon nucleation of voids at particles, the holes then grow as the applied tensile strain increases until they coalesce to give a fracture path. Examining these two processes, the volume fraction of the particles or alternatively their spacing is the most important parameter. As an upper limit, voids can grow until the point where they impinge into each other. This point is limited by the interparticle spacing [McClintock 1968]. Another geometric approach of void growth and coalescence proposed by Brown and Embury [1973] is shown in Figure 3-5. Because of the stress-concentrating effect, a

spherical void will elongate initially at a rate of about twice that of the specimen itself. As it extends and becomes ellipsoidal, it grows more slowly until, when very elongated, it extends at the same rate as the specimen. In this theory it is assumed that when the spacing of neighboring voids becomes equal to their length (Figure 3-5b), any further plastic flow is localized on the region between voids, and ductile fracture occurs immediately (Figure 3-5c).

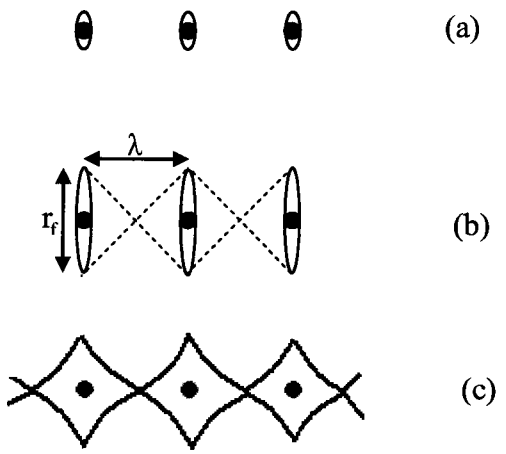

Figure 3-5 The growth, (a) and (b), and coalescence (c) of voids at particles [Brown & Embury 1973]

The growth strain is estimated to be the tensile strain required to grow the void from its initial size to the critical size (r_f). If the average particle radius is r and λ is their spacing, and if they elongate at a rate which, on average, is faster by a factor C than the rate of extension of the specimen ($1 < C < 2$), then the true strain to coalescence may be written as:

$$\varepsilon_g = \frac{1}{C}\ln\left(1+\frac{\lambda-2r}{2r}\right) \qquad 3-9$$

or in terms of volume fraction of particles (f_v):

$$\varepsilon_g = \frac{1}{C}\ln\left(\sqrt{\frac{\pi}{6f_v}}-\sqrt{\frac{2}{3}}\right) \qquad 3\text{-}10$$

In this theory the contribution of the final linkage to the total failure strain is considered to be negligible.

As a summary of the above discussion, it can be said that a low volume fraction of finely distributed, less brittle, small sized, equiaxed particles with high interfacial strength tend to delay ductile fracture to higher strains. Before discussing approaches to achieve such a desired population of particles, it is necessary to examine types of Fe-bearing intermetallic particles normally seen in the 6xxx series Al alloys.

3.3 Iron-bearing intermetallics in the 6xxx series Al alloys

Iron is a common impurity in aluminum alloys. Most commercial aluminum alloys contain around 0.2 – 0.3 wt.% Fe. The solubility of Fe in solid Al is very low, less than 0.05 wt.%. During casting process, as the primary Al solidifies iron is rejected to the remaining liquid and then solidifies in the form of intermetallic compounds with aluminum and other alloying elements. In the 6xxx series Al alloys, silicon and manganese (if present) are the main participating elements in the formation of Fe-bearing

intermetallic particles. These particles are found in the interdendritic spaces of primary aluminum and cannot be removed by any post-casting heat treatment.

The nature of these particles, their crystal structure and chemical formula, has been the subject of numerous publications and ongoing research. Available information on the different types of Fe-bearing intermetallic compounds are reviewed by [Allen *et al.* 1998] and [Liu & Chang 1999].

Regardless of the exact nature of these particles, they can be divided into two main categories based on their morphology: plate-like (Figure 3-6a) and Chinese script (Figure 3-6b). These two types of particles are examined and compared next.

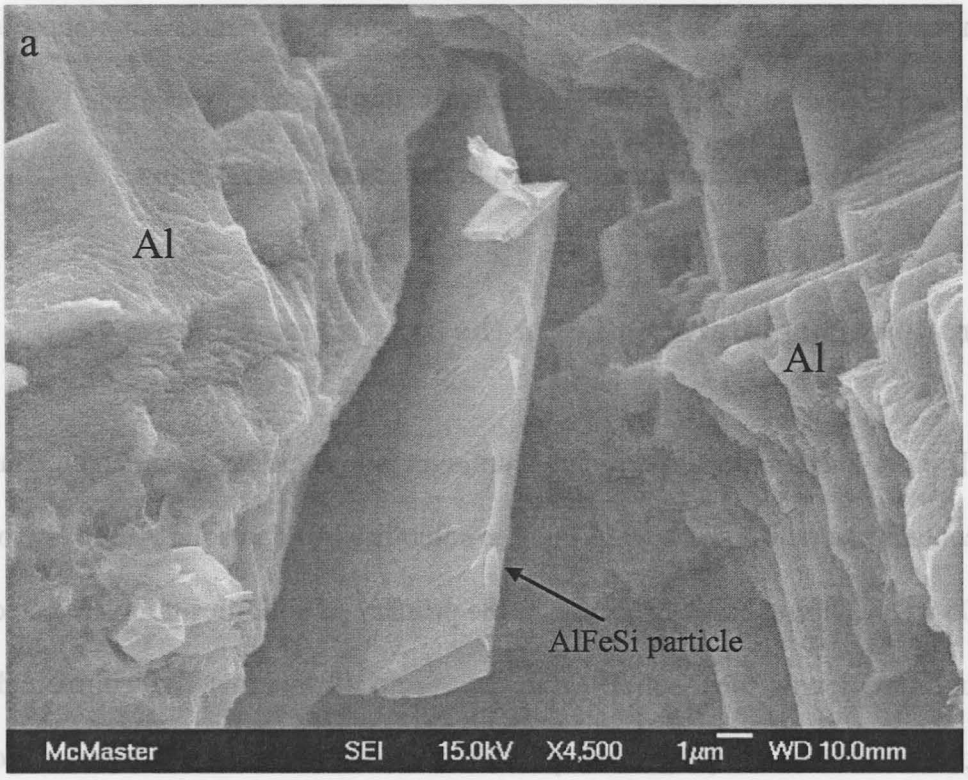

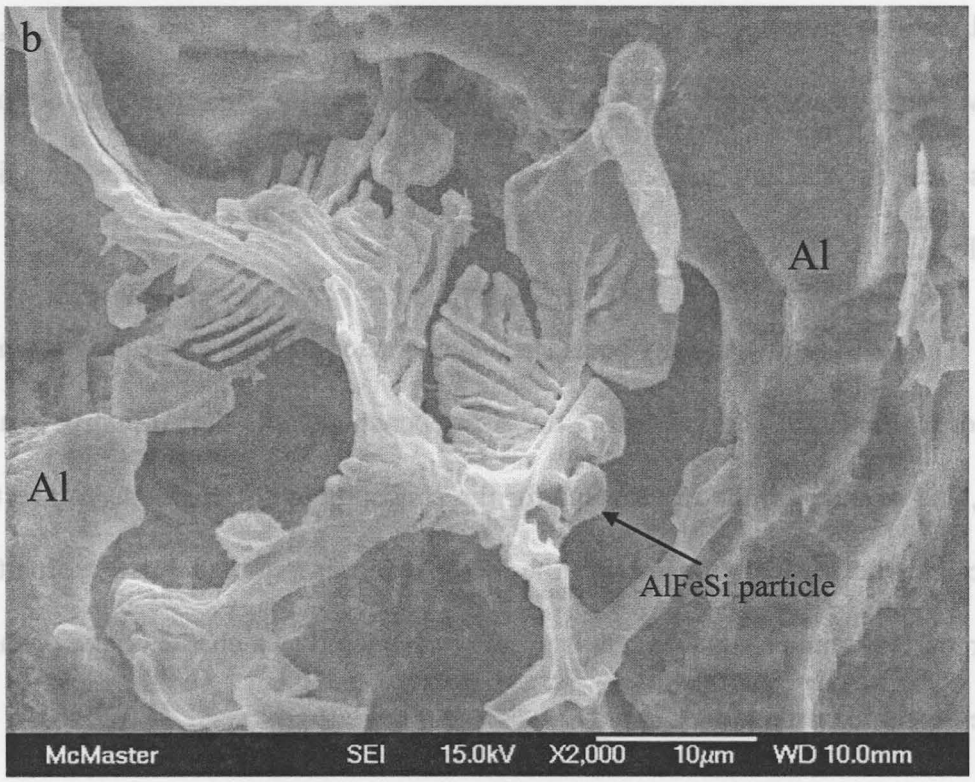

Figure 3-6 a) Plate-like and b) Chinese script Fe-bearing particles

3.3.1 Plate-like Fe-bearing particles

When Mn is not an alloying element, plate-like particles are the dominant iron-containing intermetallic particles in the microstructure of DC cast 6xxx series Al alloys. These particles are characterized by a high aspect ratio and faceted interfaces with the aluminum matrix. The crystal structure associated with these particles is monoclinic [*e.g.* Mulazimoghlo *et al.* 1996, Skjerpe 1987, Westengen 1982, Turmezey *et al.* 1990]. Two slightly different stoichiometries are reported for plate-like particles which are: Al_5FeSi and $Al_9Fe_2Si_2$ [Hansen *et al.* 1998]. A tetragonal phase with Al_3FeSi_2 chemical

formula is also observed to assume the plate-like shape [Kral 2005, Kral *et al.* 2006]. However such observations are barely made in alloys with Si contents associated with 6xxx series alloys. The presence of this phase is mostly reported in near eutectic Al-Si cast alloys.

The Fe/Si ratio is usually considered in characterizing the Fe-bearing intermetallic particles by the EDS. This is because the X-ray penetrates into the Al matrix to a certain extent, and as a result, the exact value for the concentration of elements gained through EDS cannot be trusted. Considering the stoichiometries reported for these particles, a Fe/Si ratio less than or equal to one is usually considered as a characteristic of the plate-like Fe-bearing intermetallics.

A high resolution TEM investigation by Mulazimoghlo *et al.* [1996] revealed that the Al_5FeSi particles are highly twinned which gave an insight on the growth mechanism of these particles. Since the twin planes were parallel to the growth direction they concluded that the intersection between twin plane and solid/liquid interface provided sites for atoms to attach to the growing particles. Such a mechanism prohibits the particle from twisting or bending during growth resulting in a plate-like morphology.

3.3.2 Chinese script Fe-bearing particles

Another commonly seen morphology of Fe-containing intermetallic particles is the so-called Chinese script morphology. This term is assigned because of their irregular shape seen in 2D images (Figure 3-7). In contrast to plate-like particles, Chinese script particles have a diffuse interface with the Al matrix. Two crystal structures that are assigned to particles having this morphology are cubic [*e.g.* Sha *et al.* 2006, Mulazimoghlo *et al.* 1996, Turmezey *et al.* 1990 and hexagonal [Griger *et al.* 1989, Dons 1984, Sun & Mondolfo 1967]. It is suggested [Allen *et al.* 1998] that the equilibrium Chinese script particles have hexagonal crystal structure but at cooling rates associated with the industrial processes and in the presence of trace elements, the cubic form becomes stable. The chemical formulas proposed for this phase are Al_8Fe_2Si and $Al_{16}Fe_4Si_3$. A Fe/Si ratio greater than one is a distinct characteristic of Chinese script particles. It is widely seen that the presence of Mn results in the stabilization of Chinese script particles. Mn replaces iron to an appreciable extent in the later stoichiometry of Chinese script particles which gives $Al_{16}(Fe,Mn)_4Si_3$ [Barlock & Mondolfo 1975, Zakharov *et al.* 1989].

The diffuse interfaces of these particles give them more flexibility to respond to the local changes of heat and diffusion which results in a less rigid form as opposed to plate-like particles.

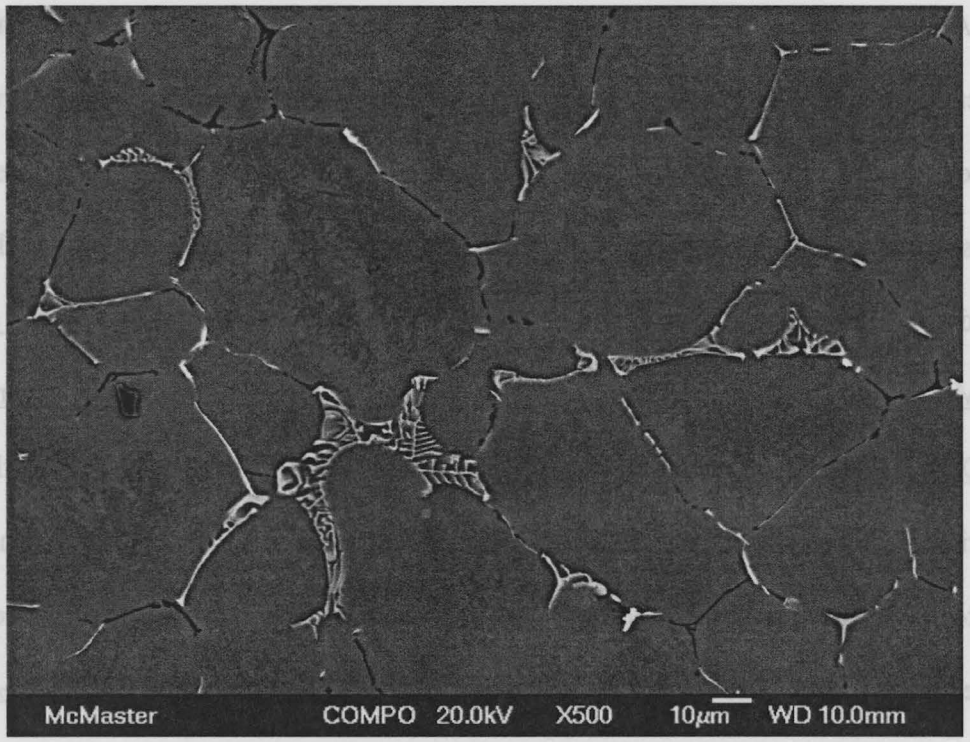

Figure 3-7 Chinese script morphology of Fe-bearing particles

By comparing these two shapes of Fe-bearing intermetallics, it can be concluded that Chinese script particles are beneficial from the viewpoint of formability. Plate-like particles are associated with low interfacial strength because of their faceted interface with the Al matrix. On the other hand, diffuse interfaces of Chinese script particles provide higher interfacial strength by interweaving matrix and particle together. It is also claimed that plate-like particles are intrinsically more brittle in comparison with Chinese script particles, perhaps, due to their low symmetry crystal structure. Finally, the elongated shape of plate-like particles increases the ability of these particles to initiate voids. To support this statement, it is reported that the presence of α instead of β has resulted in improved ductility and extrudability of the 6xxx series Al alloys [Clode &

Sheppard 1990, Musulin & Celliers 1990, Onurlu & Tekin 1994, Zajac *et al.* 1994]. In fact, it is a common practice to homogenize 6xxx series alloys at 580°C for 6 hours to transform a majority of plate-like particles formed during casting to Chinese script ones and increase extrudability [Birol 2004, Couto *et al.* 2005].

3.4 Small additions of R metals as an approach to improve formability

In section 3.2.1 it was established that a low volume fraction of finely distributed, less brittle, small sized, equiaxed particles with high interfacial strength may increase the formability of 6xxx series Al alloys. The volume fraction of the particles can only be reduced if the concentration of Fe in the melt is decreased. This can be done by reducing the usage of recycled aluminum or employing purification processes. Both of these are not practical since they will increase the cost of production. The distribution of second phase particles is usually affected by the thermo-mechanical processing of cast ingots. Since the extent of this step is greatly reduced for the strip cast sheets, this option is also not practical. The only viable possibility is to reduce the size, aspect ratio, and/or brittleness of the particles or increase the strength of the interface between particles and matrix.

As explained earlier, Chinese script particles conform to the description of a less harmful particle (higher interfacial strength, desirable shape, and less brittle) and improved formability of the alloy is expected it they are made to be the dominant

intermetallic particles of the cast microstructure instead of elongated particles. In the present investigation, this goal is pursued through small additions of Ce and La. Since Sr is known to have such an effect, the modification mechanism associated with this element is described next in order to gain an insight into how Ce and La additions might change the phase portrait of the alloy.

The mechanism by which Sr modifies the Fe-bearing intermetallics is explained according to the solidification sequence of intermetallic phases. Since these particles are composed of Al, Fe, and Si, this ternary system must be examined. The liquidus projection of the aluminum-rich corner of the Al-Fe-Si system is shown in Figure 3-8. It is calculated using Thermo-Calc and the ALCAN database. The solidification path is marked by arrows. The reactions resulting in the formation of Fe-bearing intermetallics are:

1. Liquid $\rightarrow$ Al (dendritic network) a - b
2. $L \rightarrow Al + Al_{13}Fe_4$ b - c
3. $L + Al_{13}Fe_4 \rightarrow Al + Al_8Fe_2Si$ (α) c
4. $L \rightarrow Al + Al_8Fe_2Si$ (α) c - d
5. $L + Al_8Fe_2Si$ (α) $\rightarrow Al + Al_5FeSi$ (β) d
6. $L \rightarrow Al + Al_5FeSi$ (β) d - e
7. $L \rightarrow Al + Al_5FeSi$ (β) $+ Mg_2Si + Si$ e

The reaction that is of interest here is the peritectic reaction at point "d" which results in the formation of plate-like particles (β) at the expense Chinese script particles

(α). It is suggested that modifying elements adsorb at the interface of the Chinese script particles and prevent the diffusion of silicon into their interior which is necessary for their conversion to the plate-like particles [Mulazimoglu *et al.* 1996]. Consequently, the peritectic reaction is suppressed and Chinese script particles are preserved as the dominant particles in the as-cast microstructure.

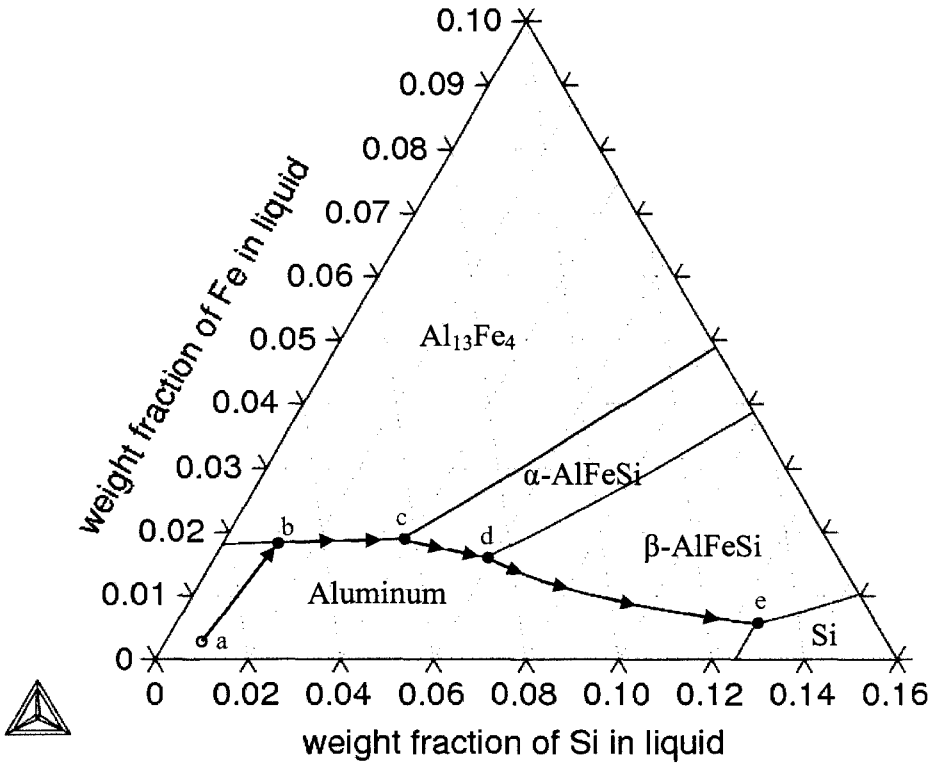

Figure 3-8 Liquidus projection of Al rich corner of Al-Fe-Si phase diagram

Mulazimoglu *et al.* [1996] found a silicon-rich layer around Chinese script (α) particles in the presence of Sr as an indication of a barrier to Si diffusion (Figure 3-9). However, because of the very fine nature of the interface the presence of Sr (modifying elements in general) cannot be verified beyond doubt.

It is mentioned that Mn addition also promotes the formation of Chinese script particles. The mechanism by which Mn stabilizes α is different than that proposed for Sr. As mentioned before, in the former case, α becomes a quaternary phase in which Fe and Mn share the same sublattice. The presence of Mn and Fe in one sublattice increases the entropy contribution to the Gibbs energy of the phase and hence increases its stability [Abu Khatwa & Malakhov 2006].

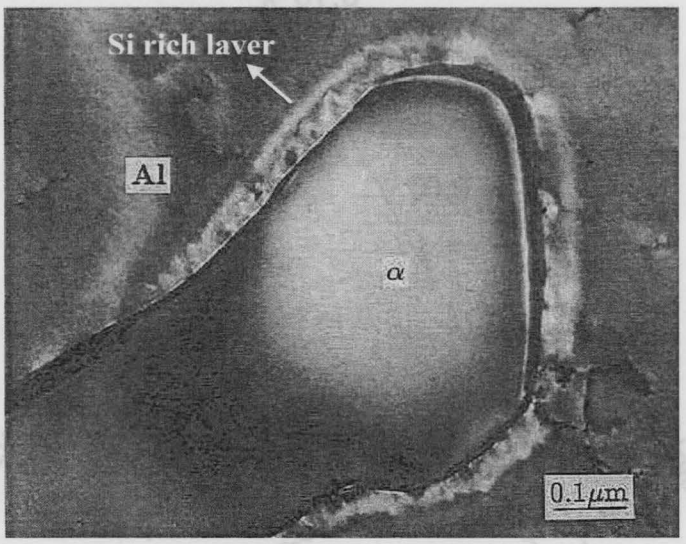

Figure 3-9 Si-rich layer surrounding α-AlFeSi phase in presence of Sr [1996Mul]

In addition to the above theories which are concerned with a change of constituent phases to new ones, it is possible to modify the existing phases without changing their nature. For example, smaller intermetallic particles can be expected due to R metals addition. As mentioned before, because the solubility of R metals in aluminum is very small, the liquid in front of growing dendrites is significantly enriched with the added element. This leads to a higher constitutional supercooling, which results in the branching

of dendrites and the decrease of dendrite spacing. Therefore, the dendrite structures will be refined and the iron-bearing intermetallics formed in the interdendritic spaces at the end of solidification are smaller. Such a phenomenon is seen in high carbon Fe-V-W-Mo steel where austenitic dendrite structure and eutectic carbides formed in inter-dendritic spaces are refined due to 0.09 wt% addition of cerium [Fu *et al.* 2005]. In the case of aluminum alloys, it has been reported [Ye *et al.* 1985] that with 1 wt% addition of mischmetal to an Al-7Si-0.3Mg alloy, the undercooling increases up to 15 K with respect to that of the reference alloy.

What forces intermetallic particles to assume an elongated shape is the interfacial energy anisotropy. When different atomic planes of a phase bear different interfacial energy, the phase will grow in a manner that increases the area of low energy faces and decreases the area of high energy planes, so, the minimum energy criterion is met. This results in an elongated particle with low surface energy facets. If the segregation of R metals results in an increase in the interfacial energy of low energy planes or a decrease in the energy of high interfacial energy ones, then, chances are a more rounded particle will form.

While all the above theories explain "how" the small additions of an element modify the intermetallic particles, none of them give an explanation on "why" some elements are able to cause such effects and others not. This means that the modification ability of an element can only be determined by experimental investigations. The rest of

this chapter deals with the experimental study of the Ce and La additions to the alloy whose composition is mentioned in Table 3-2.

3.5 Experimental procedure

3.5.1 Casting and processing

Commercial purity aluminum containing 0.13 wt. % iron was melted in a graphite crucible placed in a pit-type electrical resistance furnace. Mg was added in the form of Al-50wt. % Mg master alloy; the other alloying elements were introduced to the melt as pure materials. Two series of alloys were prepared: one with added amounts of Ce and another with La additions. Five alloys were fabricated in each series, one without R metal addition (reference alloy) and four R metal containing alloys. The amount of R metals in these four alloys were 0.03 wt. %, 0.06 wt. %, 0.1 wt. % and 0.2 wt. %. More than 0.2 wt. % could hardly be classified as a "small amount". The minimum amount of 0.03 wt. % was chosen to compare the modifying power of cerium and lanthanum with that of Sr, for which 300 ppm worked [Mulazimoglu *et al.* 1996].

Hydrogen-induced porosity is a serious problem in Al alloys which, if not prevented, deteriorates mechanical properties (fracture, fatigue ...) of the alloy. The hydrogen solubility in Al decreases with decreasing temperature; the liberation of excess

hydrogen during cooling from the melt produces porosity. A flow of argon was used in this study to remove hydrogen and thus minimize porosity. Hydrogen atoms diffuse into the Ar bubbles due to a lower pressure inside them. Argon was injected into the bottom of the crucible through a rotating tube. The action of the rotor creates smaller bubbles over a wider area, which increases surface-area/volume ratio. These finer bubbles have a longer residence time in the metal, allowing for a higher capability of collecting the hydrogen atoms present. In addition, the rotor served to stir the melt giving rise to a homogeneous melt. The degassing procedure was performed several times and after each time a small sample was cast and the composition of the alloy was verified by glow discharge optical emission spectroscopy and corrections were made if necessary. For each composition, two 5×5×25 cm^3 ingots were fabricated by pouring the melt in a water-chilled copper mold.

The compositions of these alloys were later determined by inductively coupled plasma optical emission spectroscopy. They are presented in Table 3-3. Despite all efforts, the compositions of Ce-containing alloys are different than those of La-added samples. As a result, properties and microstructures of samples with Ce and La additions were compared with those of their respective reference alloys, RC and RL.

In industrial practice, the forming process is normally performed on the sheets in T4 temper or pre-aged condition before the final aging during paint bake [Bryant 1999]. This practice was used as a guideline in the present investigation. A thermo-mechanical procedure was designed to fabricate T4 tempered sheets. This schedule is shown in Figure 3-10. It is worth noting that the T4 temper refers to a substantially stable condition

of the material achieved after solution heat treatment and natural aging of alloys at room temperature. Alloy sheets were made by hot-rolling samples at 430°C from 8 mm thickness to 3 mm. This corresponds to 62% reduction. The percent reduction that SC alloys might undergo in an industrial practice easily reaches 90% if not higher. However, similar investigation performed on the effect of Ce on the formability of AA5457 Al alloy [Yan 2007] revealed that rolling as-cast samples to 90% reduction completely destroyed the as-cast microstructure. Such mild amount of rolling (62% reduction) was chosen here in order to preserve as much of the microstructural aspects of as-cast samples as possible.

Table 3-3 Chemical compositions of alloys used in the present work (wt. %)

Alloy	Mg	Si	Fe	Cu	Ce	La	Al
RC	0.76	0.8	0.5	0.21	-	-	
C04	0.79	0.81	0.53	0.23	0.04	-	
C07	0.75	0.76	0.5	0.21	0.07	-	Rem.
C1	0.79	0.85	0.55	0.23	0.1	-	
C2	0.75	0.78	0.51	0.22	0.2	-	
RL	0.82	0.56	0.42	0.2	-	-	
L04	0.83	0.57	0.43	0.2	-	0.04	
L07	0.81	0.57	0.43	0.2	-	0.07	Rem.
L1	0.85	0.6	0.45	0.2	-	0.11	
L2	0.8	0.58	0.42	0.19	-	0.21	

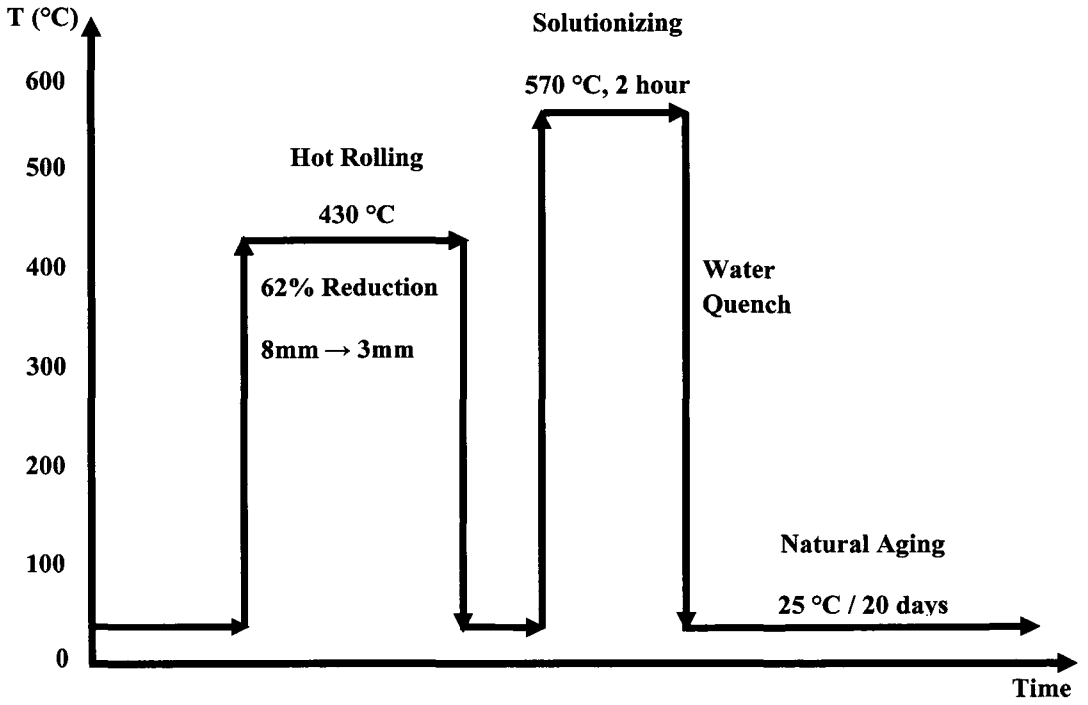

Figure 3-10 Schematic thermo-mechanical processing performed on the alloys

A thermodynamic calculation using Thermo-Calc and ALCAN database showed that the Mg_2Si phase is not stable at temperatures higher than 530°C. To ensure the dissolution of the Mg_2Si particles, the solution heat treatment of samples was performed at 570°C, forty degrees Celsius higher than the predicted temperature. Rolled samples were solutionized for 2 hours and quenched in ice water. The quenched samples were brought to T4 temper by natural aging at room temperature for at least 20 days.

3.5.2 Microstructural analysis and mechanical testing

An examination of the square cross-section of RC alloy revealed that except for 5 mm of the edges of the sample which consisted of the chill zone and columnar region, the rest of the cross-section was made of equiaxed grains. All experiments were performed on samples cut from the region containing equiaxed grains (Figure 3-11). A portion of the center of the ingots was discarded to avoid possible effects associated with the center line (shrinkage, segregation, etc.)

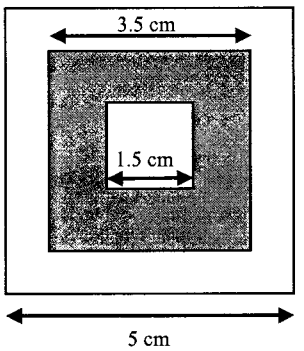

Figure 3-11 The region of the ingot used for the experiments (gray area)

Samples were prepared for metallographic investigation by hot mounting in Lucite followed by grinding with SiC papers and polishing with diamond solutions and colloidal silica. Scanning electron microscopy (SEM) was used to characterize the morphology of intermetallic compounds and an energy-dispersive spectroscopy (EDS) detector attached to the SEM was employed to find constituent elements of intermetallics and estimate the Fe/Si ratio where applicable.

Intermetallic particles were extracted from alloys in as-cast and T4 temper via a selective dissolution of the FCC matrix in boiling phenol detailed by Gupta *et al.* [1996]. Boiling phenol reacts with the FCC matrix according to the following reaction:

$$3C_6H_5OH + 2Al \rightarrow 2Al(C_6H_5O)_3 + 3H_2$$

while the Fe-bearing intermetallic particles remain intact. When the dissolution is complete, a mixture of benzylalcohol and toluene is added to the resultant suspension. Through a series of centrifuge and decantation steps the intermetallic particles were separated from the liquid mixture. Finally, the particles were rinsed with anhydrous ethanol, centrifuged and dried in air at 120°C. This process yields a gray powder, which can be examined by X-ray diffraction (XRD) analysis.

Boiling phenol was also used to reveal the true 3D morphology of intermetallic particles. Specimens of RL and L2 alloys were deep-etched by holding $0.75 \times 0.75 \times 3$ cm^3 samples in boiling phenol for 5 minutes. The Al matrix was partially dissolved which made it possible to examine the morphology of Fe-bearing intermetallics by SEM.

The effects of Ce and La were quantified via morphological changes of Fe-bearing intermetallic compounds. Quantitative metallography was employed to determine the area % of intermetallic phases. For each alloy, several SEM images taken in the backscatter mode were analyzed by UTHSCSA ImageTool 3 image analyzing software[2]. The details of this investigation are presented in appendix II.

[2] http://ddsdx.uthscsa.edu/dig/itdesc.html

Grain structures of the samples in the as cast and T4 condition were also revealed by electroetching samples using Barker's reagent. The grains would appear in different colors when investigated by optical microscopy under polarized light. Grain size measurement was performed according to ASTM E112-96 standard procedure. This procedure is elaborated in Appendix III.

Hardness testing was performed on solutionized and T4 tempered alloys in order to assess the effect of R metals on the aging of the alloys. The test was carried out according to the ASTM E18-03 standard procedure using a 1/16 inch ball indenter and total force of 60 Kgf. This setting corresponded to Rockvell hardness scale F (HRF). Scale F was chosen since it is the most appropriate for soft sheets of metals such as solution treated sheets in the present investigation.

A conventional method of assessing bendability is to measure the *r/t* ratio, where *r* is the minimum bend radius attained without fracture and *t* is the sheet thickness. The smaller the (*r/t*) value, the greater the bendability of a material. Datsko and Yang [1960] theorized that "failure will occur in the outer fiber of a material being bent when the true strain in the outer fiber is equal to the true strain at the instant of fracture of a tensile test specimen of the same material". They proposed the following relation,

$$\frac{r_{min}}{t} = \frac{C}{A_r} - 1 \qquad 3\text{-}11$$

where C is a constant equal to 50-60 and A_r is reduction in area at fracture in a tensile test expressed in percentage. They showed that this relation properly correlated the

experimentally measured bendability data to A_r for different materials. It means that the bendability of a material can be assessed by a simple tensile test.

In order to characterize the bendability of the alloys under study, tensile test specimens were machined from the sheets in T4 temper according to ASTM B557 (subsize specimen 1 inch gauge length). In each case, four samples were tested by an Instron 5566 machine; a constant crosshead speed of 2 mm/min was maintained. A strain gauge extensometer was employed to measure the elongation with a great deal of accuracy.

3.6 Results and Discussion

3.6.1 As-Cast condition

Figure 3-12 shows a typical cast microstructure of the reference alloy sample. As expected, the microstructure consists of primary aluminum and plate-like Fe-bearing intermetallic particles (seen as needles in this 2D image). Figure 3-6a showing the reference sample with the FCC matrix partially dissolved in boiling phenol (deep etching) clearly illustrates that these particles are platelets.

According to the results of the EDS examinations, the Fe/Si ratio of these particles is very close to one which once again points out that they are of β type. As an example, the composition of the particle marked with an arrowed in Figure 3-12 is

presented in Table 3-4. Nevertheless, the true nature of these particles can only be revealed by XRD. X-ray diffractogram of intermetallics extracted from the sample RC is shown in Figure 3-13. These results corroborate that these particles are monoclinic $Al_9Fe_2Si_2$.

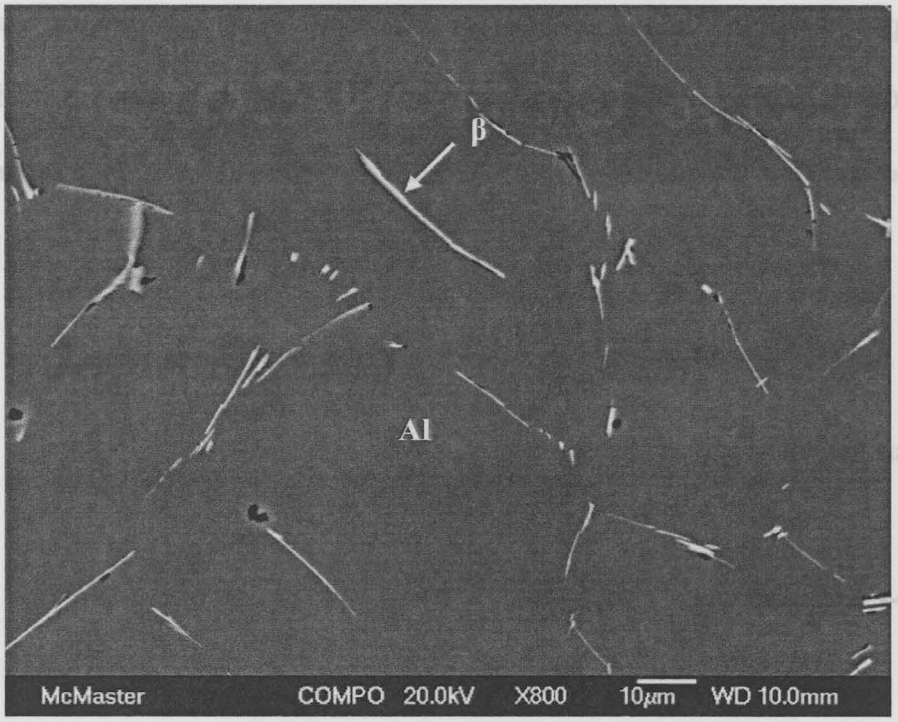

Figure 3-12 Backscattered image of as-cast reference alloy RC, showing that the β platelets are the only intermetallic particles present in the microstructure

Table 3-4 EDS analysis of the composition of the particle arrowed in Figure 3-12

Element	Atomic % (± 0.1)
Al	81.7
Si	9.1
Fe	9.2

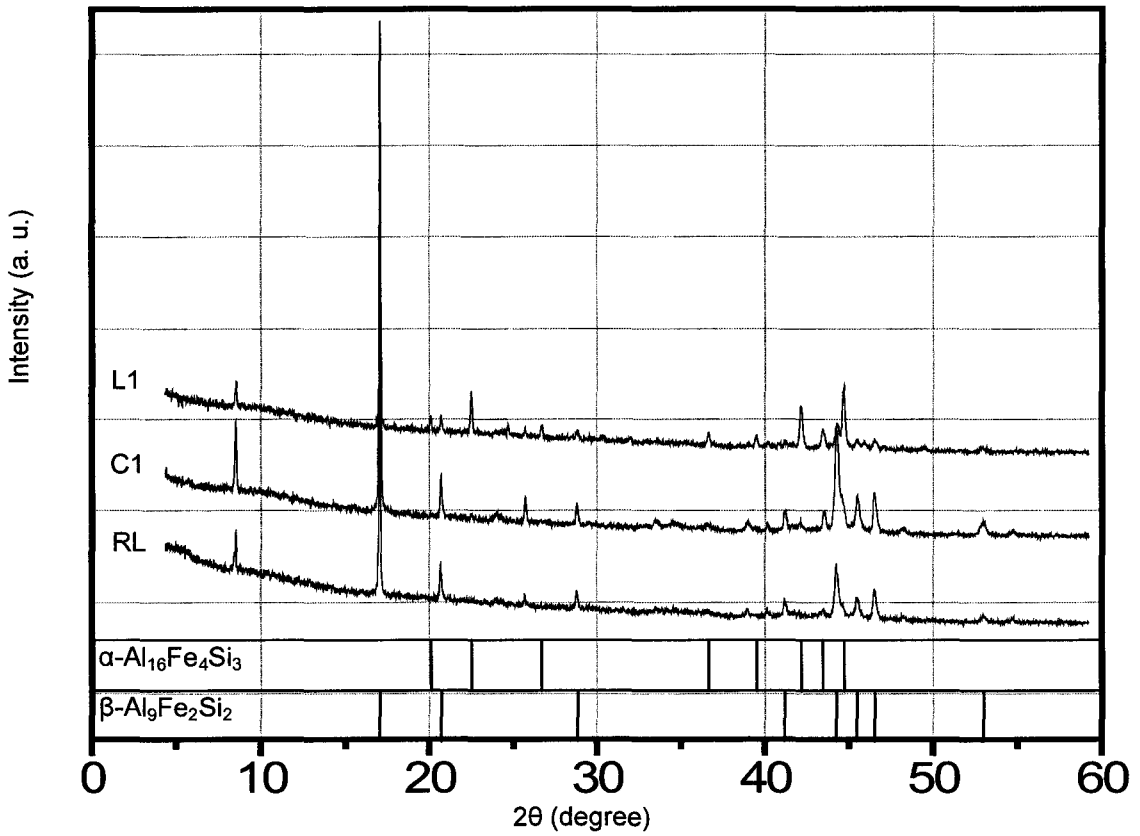

Figure 3-13 XRD patterns of intermetallic phases extracted from as-cast RC, C1, and L2 alloy samples

Additions of cerium do not noticeably change the phase portrait of the alloy (Figure 3-14a-d). The XRD spectrum of extracted particles from the sample containing 0.1 wt. % Ce, presented in Figure 3-13, shows similar features as that of the reference sample. As an advantage however, Ce additions lead to a slight decrease in the aspect ratio of β particles (Table 3-5).

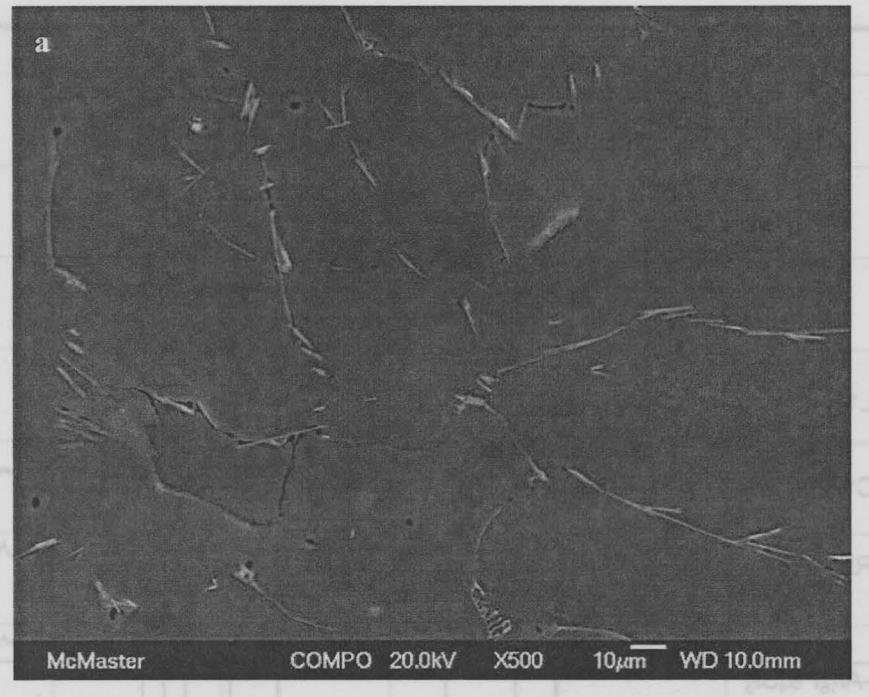
a
McMaster COMPO 20.0kV X500 10μm WD 10.0mm

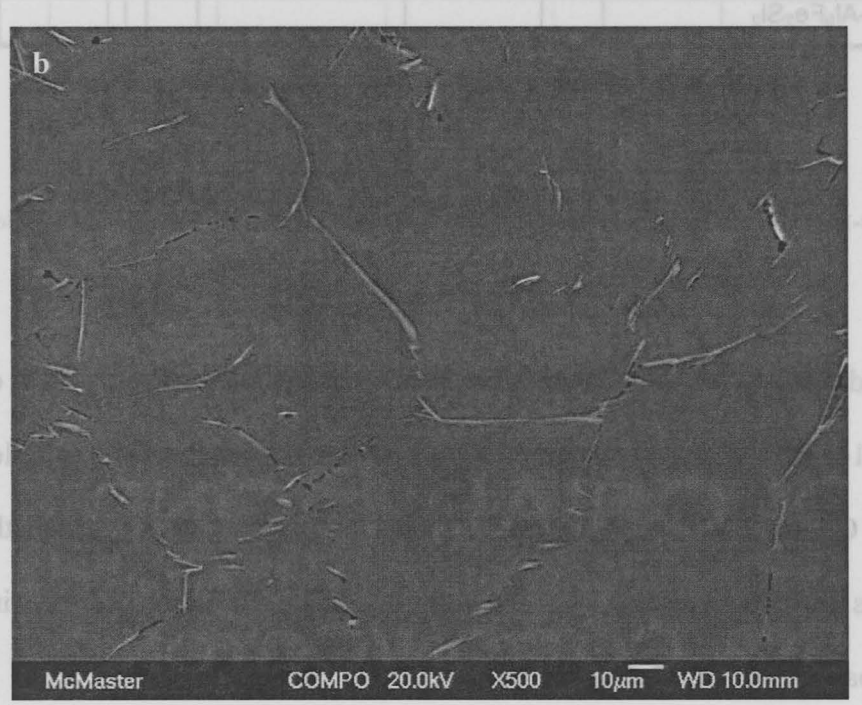
b
McMaster COMPO 20.0kV X500 10μm WD 10.0mm

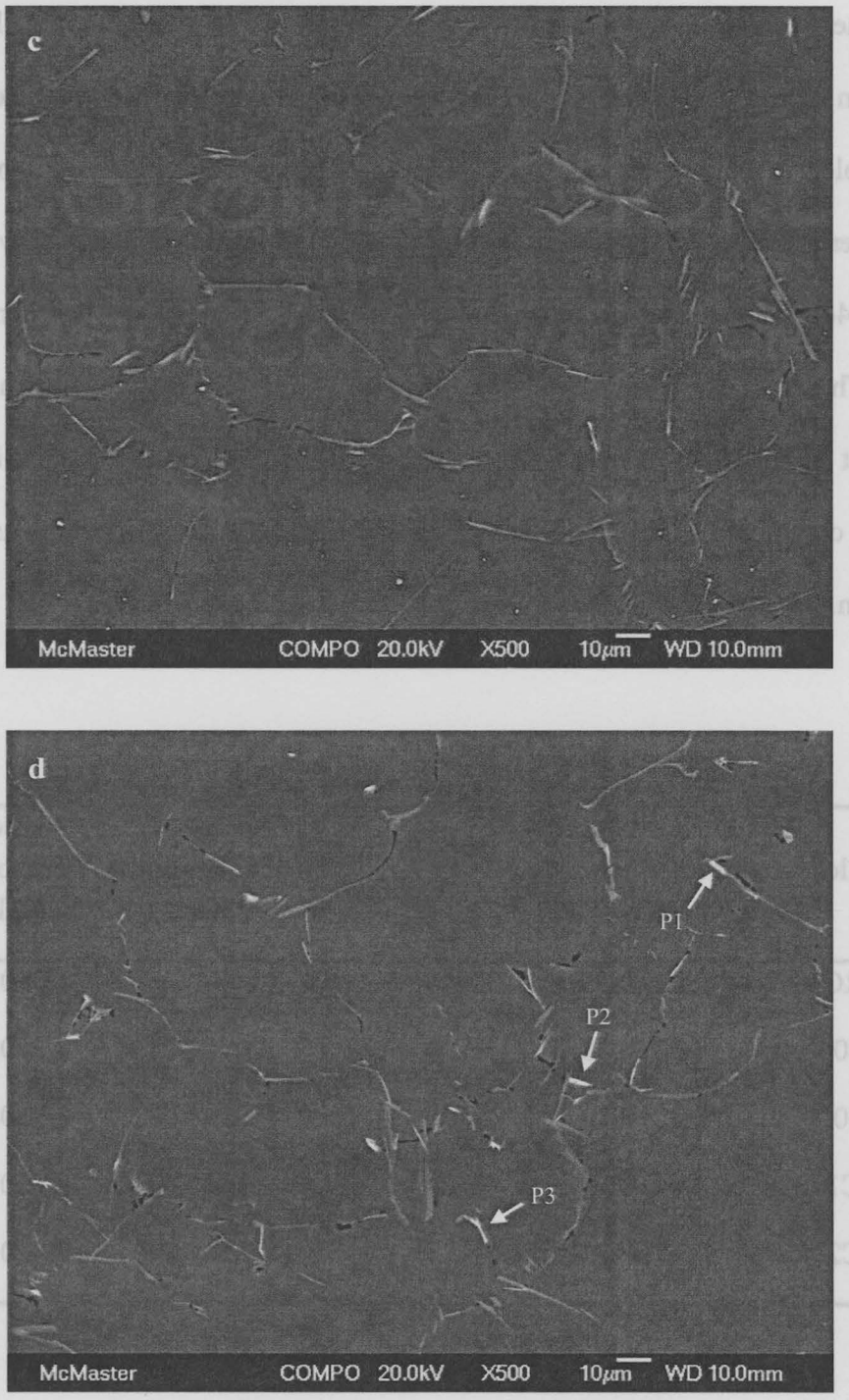

Figure 3-14 Backscattered image of the a) C04, b) C07, c) C1, and d) C2 alloy samples

Other than Fe-containing particles, the presence of a new intermetallic phase is observed in alloys containing Ce. These intermetallic particles are characterized by a brighter color in backscattered images which indicates the existence of high atomic number elements in the phase. EDS examination of particles marked by arrows in Figure 3-14d revealed that Ce along with Al, Si, and Cu are the constituents of these particles. There is a slight increase in the total area % of intermetallics with an increase in the amount of Ce. This increase can be attributed to the formation of this new Ce-containing compound (Table 3-5). It must be emphasized that this new phase does not contain iron.

Table 3-5 Effect of Ce addition on the intermetallic phases

Alloy	Total Area Percent of Intermetallic Phases ($\alpha + \beta$)	Area Percent of α Phase	Area Percent of R-bearing Phases	Aspect Ratio of β particles
RC	2.11±0.06	-	-	7.0±0.3
C04	2.28±0.08	-	0.05±0.01	6.3±0.4
C07	2.32±0.10	-	0.09±0.02	6.5±0.2
C1	2.34±0.10	-	0.16±0.02	5.7±0.1
C2	2.47±0.20	-	0.26±0.04	5.4±0.2

Table 3-6 EDS analysis of the composition of the particles P1 through P3 shown in Figure 3-14d

Element	Atomic % (± 0.1)		
	P1	P2	P3
Al	88.5	88.7	81.9
Si	6.7	5.5	12.7
Fe	-	-	-
Ce	5.2	4.9	3.8
Cu	1.6	1.9	1.6
Mg	-	-	-

An addition of La up to 0.07 wt. % also does not change the type of the Fe-bearing intermetallic phases in the as-cast alloys (Figure 3-15a and b). An interesting change in the nature of intermetallics is observed for alloys with 0.1 and, more pronouncedly, with 0.2 wt. % of lanthanum in which particles with Chinese script morphology exist side-by-side with the plate-like β particles (Figure 3-15c and d). According to the outcome of EDS analysis, these particles are characterized by a Fe/Si ratio within the 1.2–1.6 range (*e.g.* refer to the composition of particle P1 and P2 of Figure 3-15c presented in Table 3-7). XRD analysis of extracted particles from a sample containing 0.1 wt.% La identified them as cubic α-$Al_{16}Fe_4Si_3$ phase. The true 3D shape of these particles revealed by deep-etching a sample containing 0.2 wt. % La is previously shown in Figure 3-6b. By raising the concentration of La from 0.1 wt. % to 0.2 wt. %, the

fraction of the α phase can further be increased from 1/2 to approximately 3/4 (Table 3-5).

Two possible mechanisms were mentioned in section 3.4 to explain how an added element could modify Fe-bearing intermetallics. They were the inhibition of phase transformation by surface adsorption, and an increasing stability of a phase by increasing the entropy contribution to the Gibbs energy of the phase. In the latter case the added element becomes a constituent of the phase. Examination of several plate-like and Chinese script Fe-bearing intermetallics using EDS did not reveal the presence of La in them, which suggests the surface adsorption as a more plausible mechanism. Similarly to Sr, it can be imagined that adsorption of La to α/L interface does not allow Si to enter α, thus preserving its dominance in the as-cast microstructure. This hypothesis and its implications will be further examined in chapter 4.

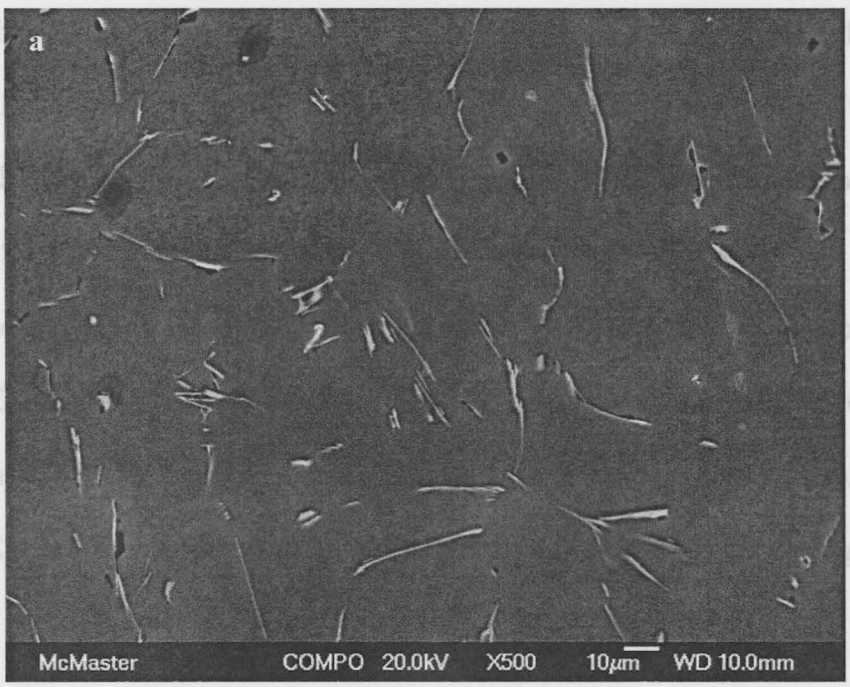

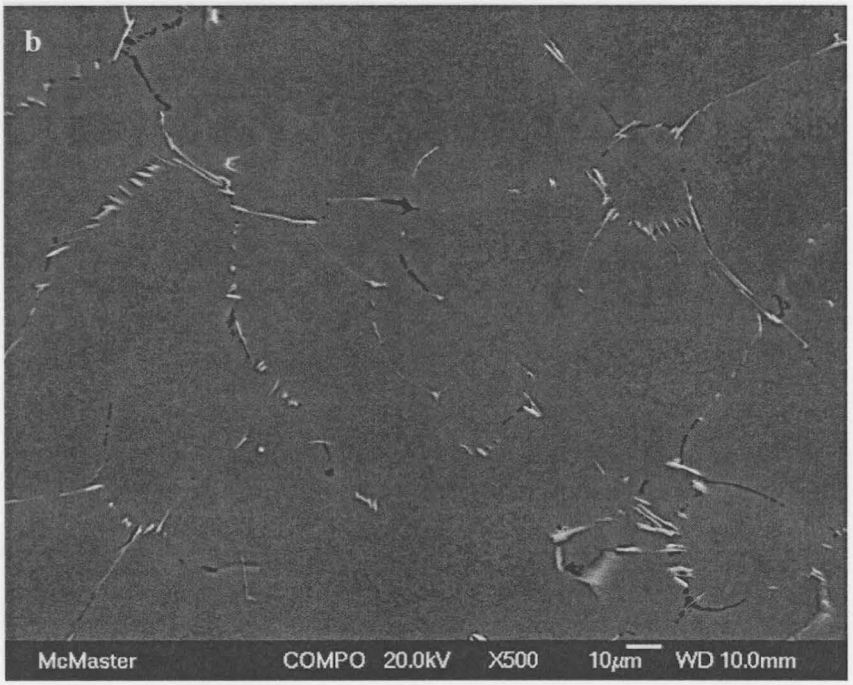
b
McMaster
COMPO 20.0kV X500 10μm WD 10.0mm

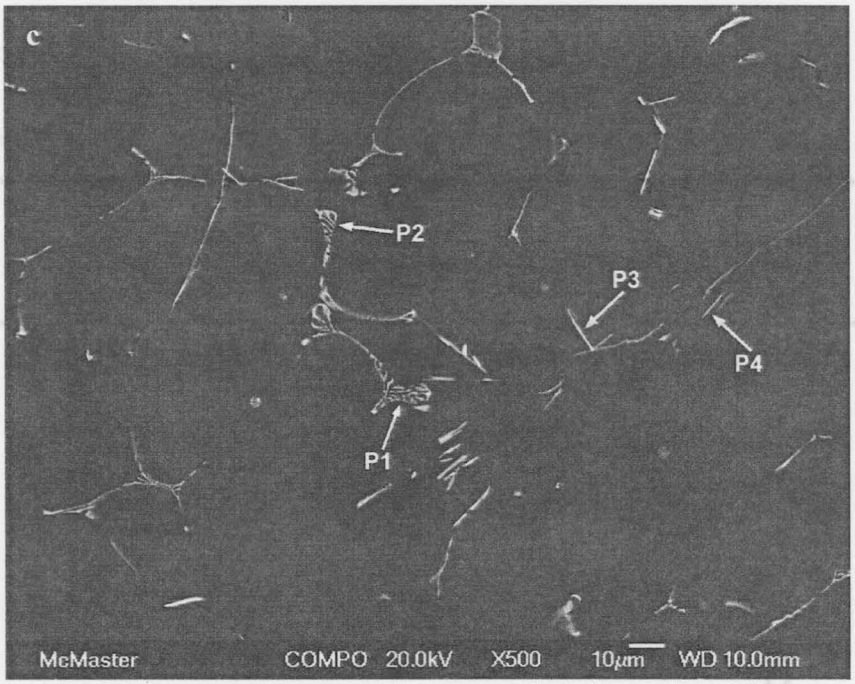
c
P2
P3
P4
P1
McMaster
COMPO 20.0kV X500 10μm WD 10.0mm

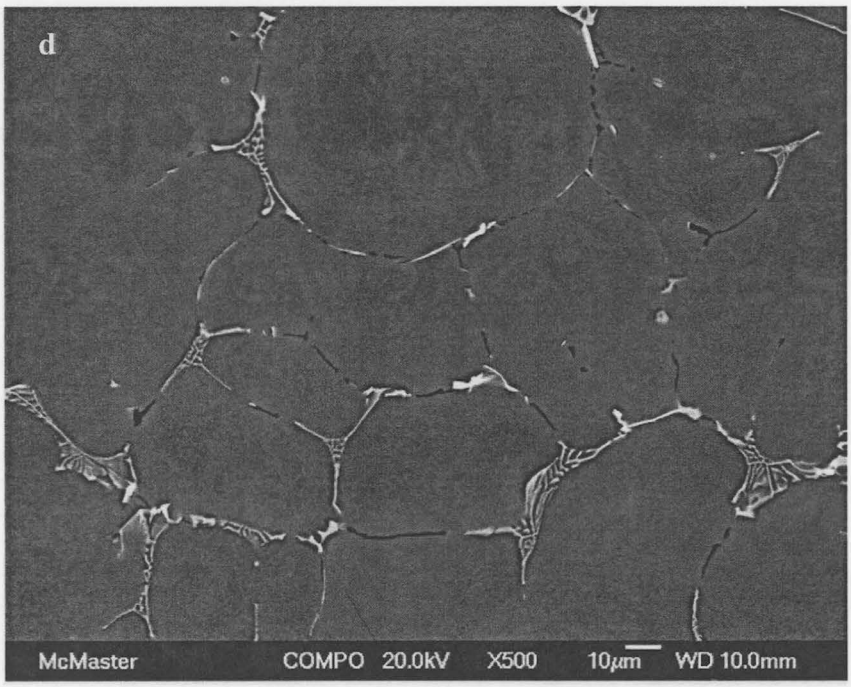

Figure 3-15 SEM image of a) L04, b) L07, c) L1, and d) L2 alloy samples

Table 3-7 EDS analysis of the composition of the particles P1 through P4 shown in Figure 3-15c

Element	Atomic % (± 0.1)			
	P1	P2	P3	P4
Al	80.1	77.2	79.3	83.3
Si	8.3	8.4	13.4	8.4
Fe	10	13.2	-	8.3
La	-	-	5.5	-
Cu	1.6	1.2	1.8	-
Mg	-	-	-	-
Fe/Si	1.2	1.55	-	

Table 3-8 Effect of La addition on the intermetallic phases

Alloy	Total Area Percent of Intermetallic Phases (α + β)	Area Percent of α Phase	Area Percent of R-bearing Phases	Aspect Ratio of β particles
RL	2.05±0.07	-	-	6.1±0.2
L04	2.13±0.05	-	0.046±0.007	6.0±0.2
L07	2.19±0.20	-	0.10±0.03	5.3±0.2
L1	2.22±0.20	1.17±0.09	0.17±0.03	5.3±0.1
L2	2.4±0.07	1.84±0.10	0.28±0.06	5.2 ±0.1

Lanthanum, however, did participate in the formation of new intermetallic particles similar to those observed in Ce-added alloys. An example of such particles is P3 in Figure 3-15c. Once again, it is found that iron is not a constituent of these particles. The increase in the fraction of La-containing phases with the increase in the La concentration is once again very similar to what is observed in Ce-added alloys (compare the third columns of Table 3-8 and Table 3-5).

Another evidence for the greater modification power of lanthanum was gained by examining the grain structure of the alloys. The grain structure of samples with 0.2 wt. % Ce and 0.2 wt. % La are compared in Figure 3-16a and b. It is seen that the addition of 0.2 wt. % cerium results in a non-uniform grain structure, while the La-added sample shows a uniform grain size. The same non-uniformity of grain structure was also seen at lower Ce concentrations. More importantly, the increase in La content resulted in a gradual decrease in the grain size of the cast alloy (Figure 3-17).

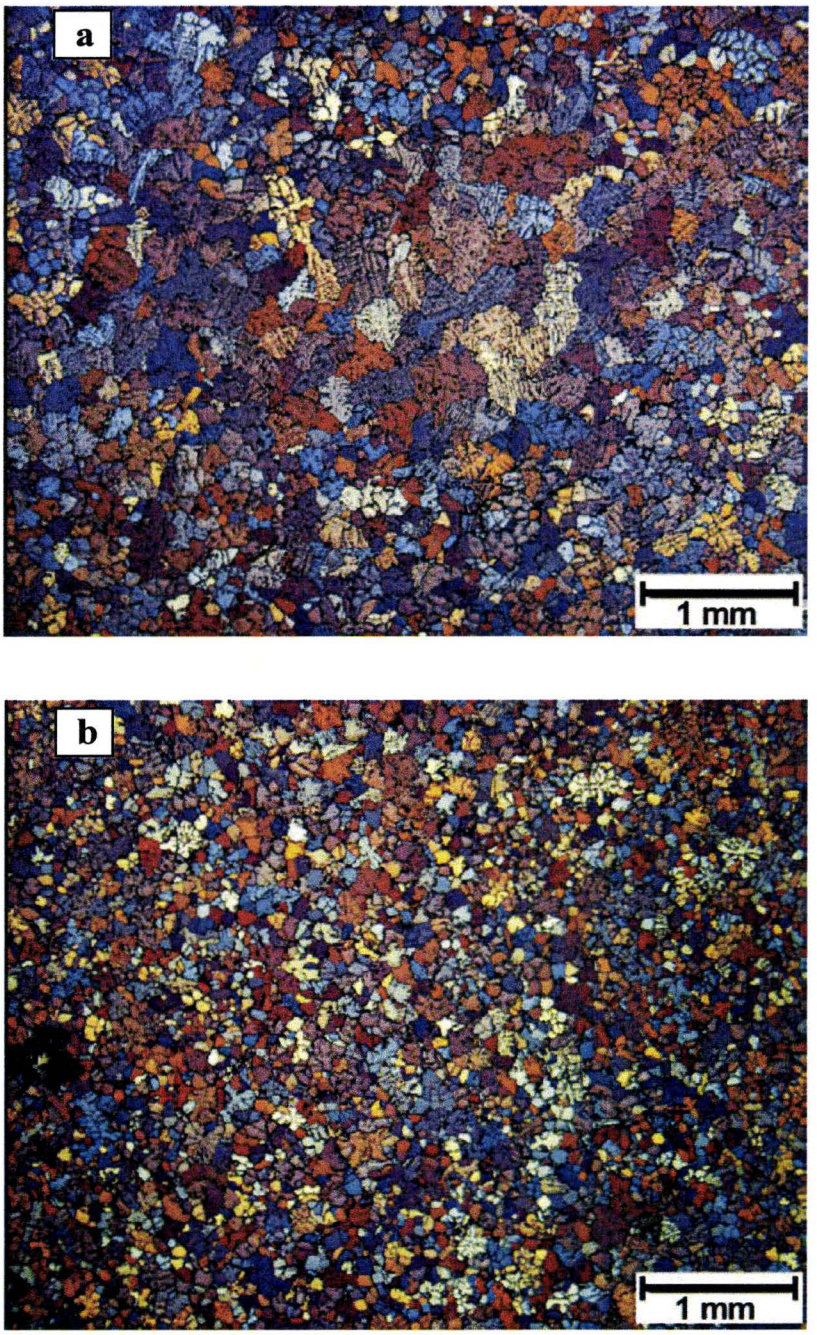

Figure 3-16 Grain structure of (a) as-cast C2 alloy sample, showing a non-uniform structure and (b) as-cast L2 alloy sample, showing a uniform grain size

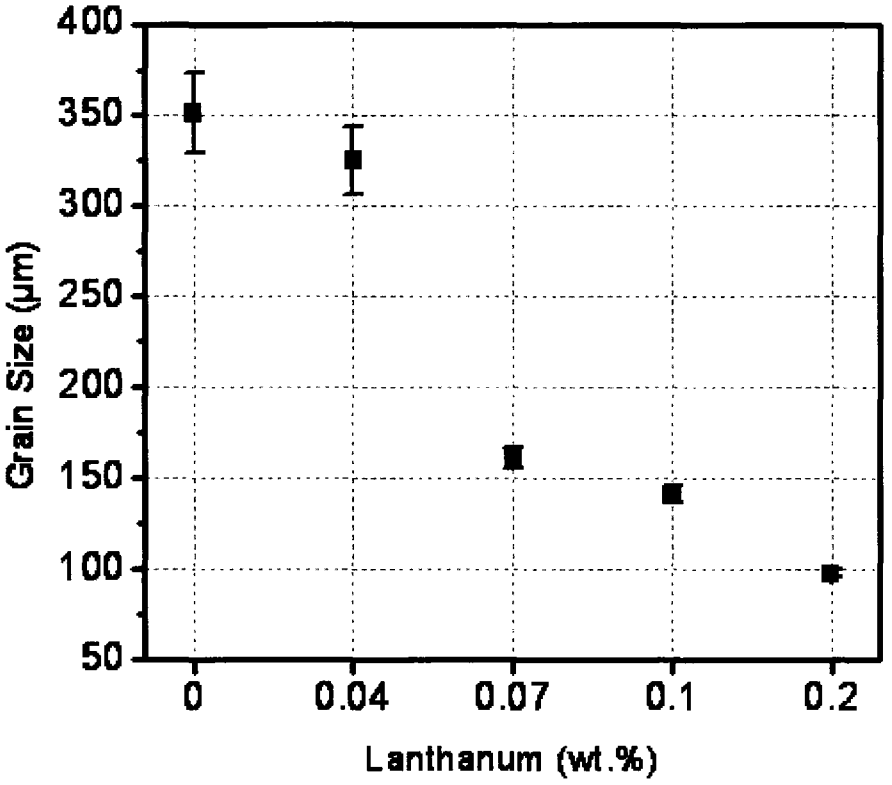

Figure 3-17 Influence of La on the grain size of as-cast alloys

The grain refinement of La-added samples can only be explained by the introduction of an inoculant due to La addition. Lanthanum oxide is the first thing that comes to mind. La is a highly reactive element, it is possible that very small oxide particles are formed in the melt which act as nucleation sites for Al. Such an effect is reported for an Fe-V-W-Mo alloy [Fu *et al.* 2005] modified by Ce. If oxides are to be assigned as the nucleating agent, then, it is not clear why such grain refinement is not observed in Ce-added samples while Ce has even greater affinity for oxygen than La. In addition to high melting temperature which both lanthanum oxide and cerium oxide have, a grain refiner must be wetted by the molten alloy, in other words, the contact angle between liquid and the grain refiner must be as low as possible [Quested 2004, Murty *et*

al. 2002]. This criterion can be met if the interfacial energy between the inoculants and solidifying phase is small. Low interfacial energy between two solids is attained if they have planes with similar atomic structure and atomic spacing.

Lanthanum oxide has a hexagonal ($P\bar{3}m1$) crystal structure with a=0.3938 nm and c=0.61361 nm at room temperature [Aldebert & Traverse 1979]. The disregistery between [0001] plane of this phase with [111] plane of FCC aluminum (planes that have similar atomic structure) is more than 37 percent. Ceria has a cubic crystal structure ($Fm\bar{3}m$) with a=5.412 nm at 25°C [Kuemmerle & Heger 1999]. The mismatch between ceria and Al is 34 % compared to disregistery of TiB_2 which is 5.9% at room temperature [Quested 2004]. As seen, none of these oxides can be considered as effective inoculants. It is noteworthy that Aldebert and Traverse [1979] reported the existence of a cubic crystal structure ($Im\bar{3}m$) for La_2O_3 at high temperatures (> 1800°C) with a=4.51 nm. The disregistry for this phase is less than 12 %.

Yan [2007] examined the modification effect of Ce on a 5xxx series Al alloy and observed grain refinement due to 0.1 wt% addition of Ce. She suggested that the cerium aluminide (Al_4Ce) particles are acting as the heterogeneous sites resulting in the grain refinement. Ce-containing and La-containing particles are seen in the microstructure of the Ce-added and La-added alloys respectively. Since these particles were not characterized in this investigation no speculation can be done on the capability of these particles to act as grain refiner. However, they were typically observed to be in the interdendritic spaces along with Fe-bearing intermetallics rather than in the center of a

grain. Also, a high concentration of alloying elements is needed for the formation of these particles. Such concentrations are not achieved before the formation and appreciable growth of Al dendrites which makes it less probable for these particles to be the nucleation sites.

At first glance, both a smaller grain size and a greater fraction of α-AlFeSi particles with Chinese script morphology are beneficial to the formability of the Al alloy under investigation. However, it should be kept in mind that 6xxx series alloys are wrought heat-treatable alloys and, therefore, a favorable alteration of the as-cast microstructure is practically meaningful only if the effect of this alteration is retained in alloys which have undergone thermo-mechanical processing.

3.6.2 T4 condition

Central to the high strength of 6xxx series Al alloys is the precipitation hardening mechanism. It is imperative that the changes in the chemistry of the alloy do not jeopardize this strengthening mechanism. On the other hand, it will be of great scientific and industrial interest if the additions of Ce and/or La result in further strengthening of the alloy by forming additional precipitates. Rockwell hardness measurements were performed on alloys naturally aged at room temperature for 8 and 20 days to characterize the effect of Ce and La additions on the precipitation hardening of the alloy. The results

are shown in Figure 3-18. It is seen that these additions neither improve nor deteriorate the strength of the alloy in T4 temper.

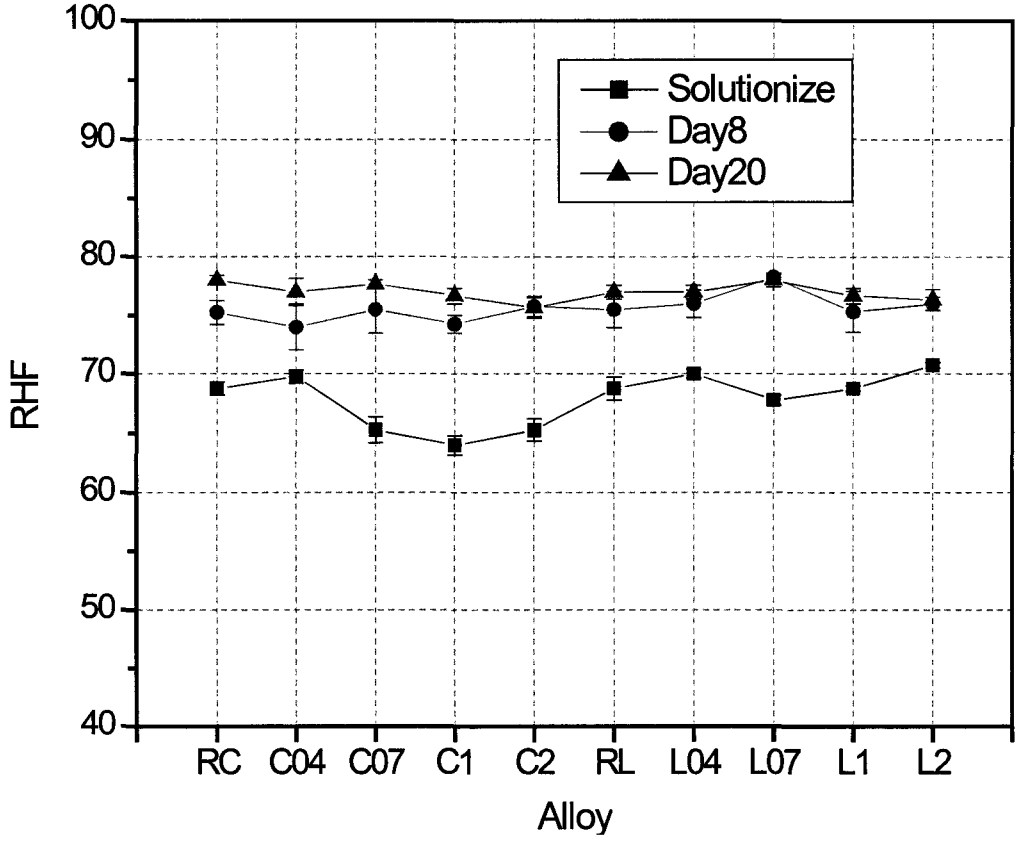

Figure 3-18 Effect of Ce and La addition on the hardness of naturally aged alloys

Uniaxial tensile testing was performed on reference, C1, and L2 alloy samples in T4 temper and tensile properties data were extracted from stress-strain curves. It is seen in Table 3-9 that all pertinent properties are virtually the same. Since the alloys show the same elongation at fracture, equation 3-11 predicts that all alloys have the same level of

bendability. It means that, despite all the beneficial effects that the addition of La has had on the alloy the in as-cast condition, it has not been able to deliver the sought-after higher bendability of this alloy. The microstructure and grain size of the alloys in T4 temper were examined to explain the cause of this phenomenon.

Table 3-9 Tensile properties of samples in T4 temper

Alloy	Yield stress (MPa)	Ultimate Tensile Stress (MPa)	Uniform Elongation (%)	Elongation to Fracture (%)
RC	124±1	240±1	20±1	23±1
C1	128±3	239±2	21±1	25±2
RL	128±1	244±1	21±1	25±1
L2	132±2	241±3	21±1	23±2

The microstructures of the reference, C1, and L2 alloys in T4 temper are illustrated in Figure 3-19a-d. It is seen that morphological features of the cast alloys have changed considerably after thermo-mechanical processing. The Fe-containing intermetallics have broken down into relatively smaller parts. On the other hand, rolling and solutionizing have had little influence on the type of the AlFeSi phases. XRD examination showed that β-AlFeSi was still the dominant intermetallic phase in the reference and C1 alloys while α-AlFeSi was the dominant phase in the L2 alloy (Figure 3-20). The important observation is that the microstructures of all alloys are now

somewhat similar, exhibiting relatively small sized and discrete AlFeSi particles forming a necklace type configuration.

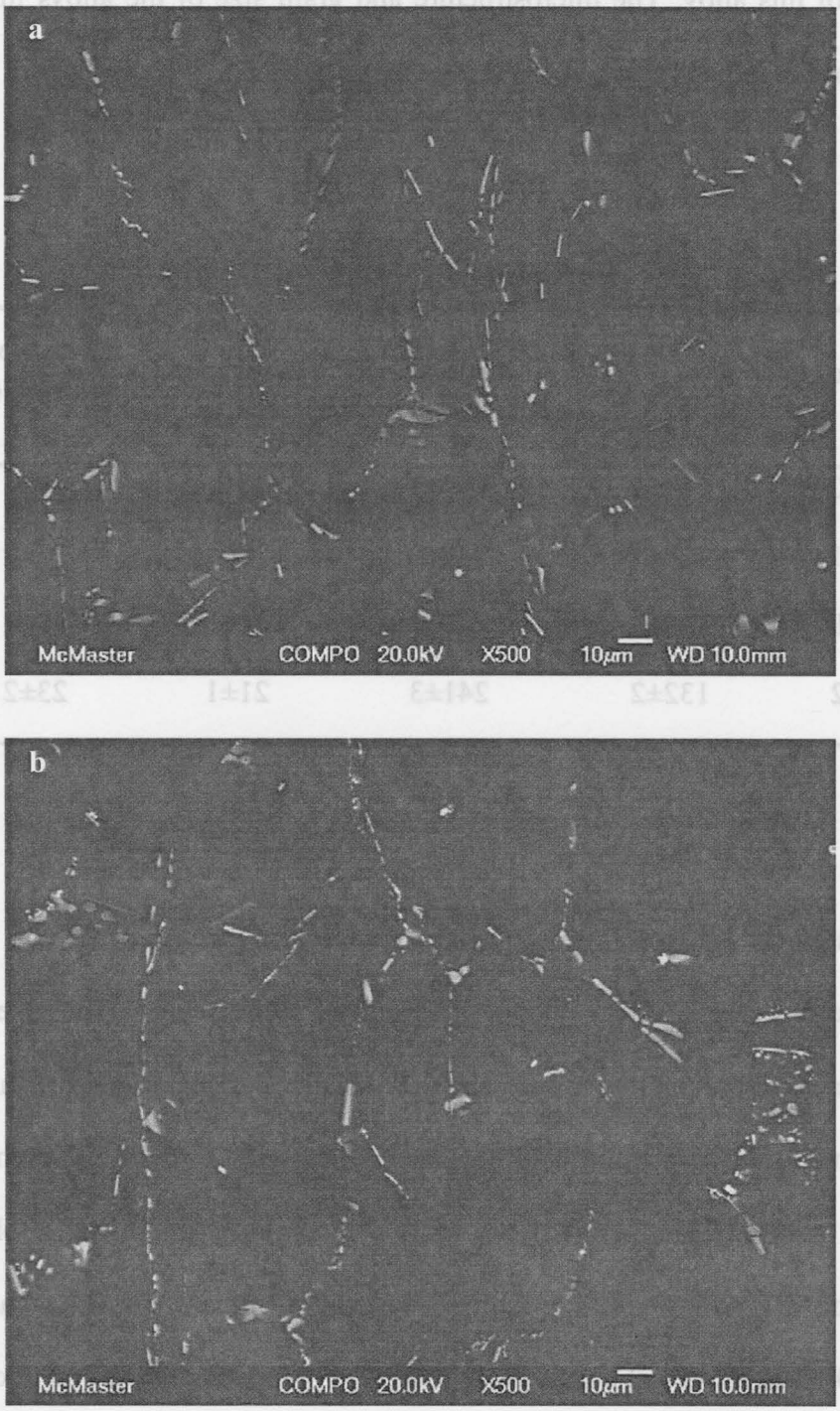

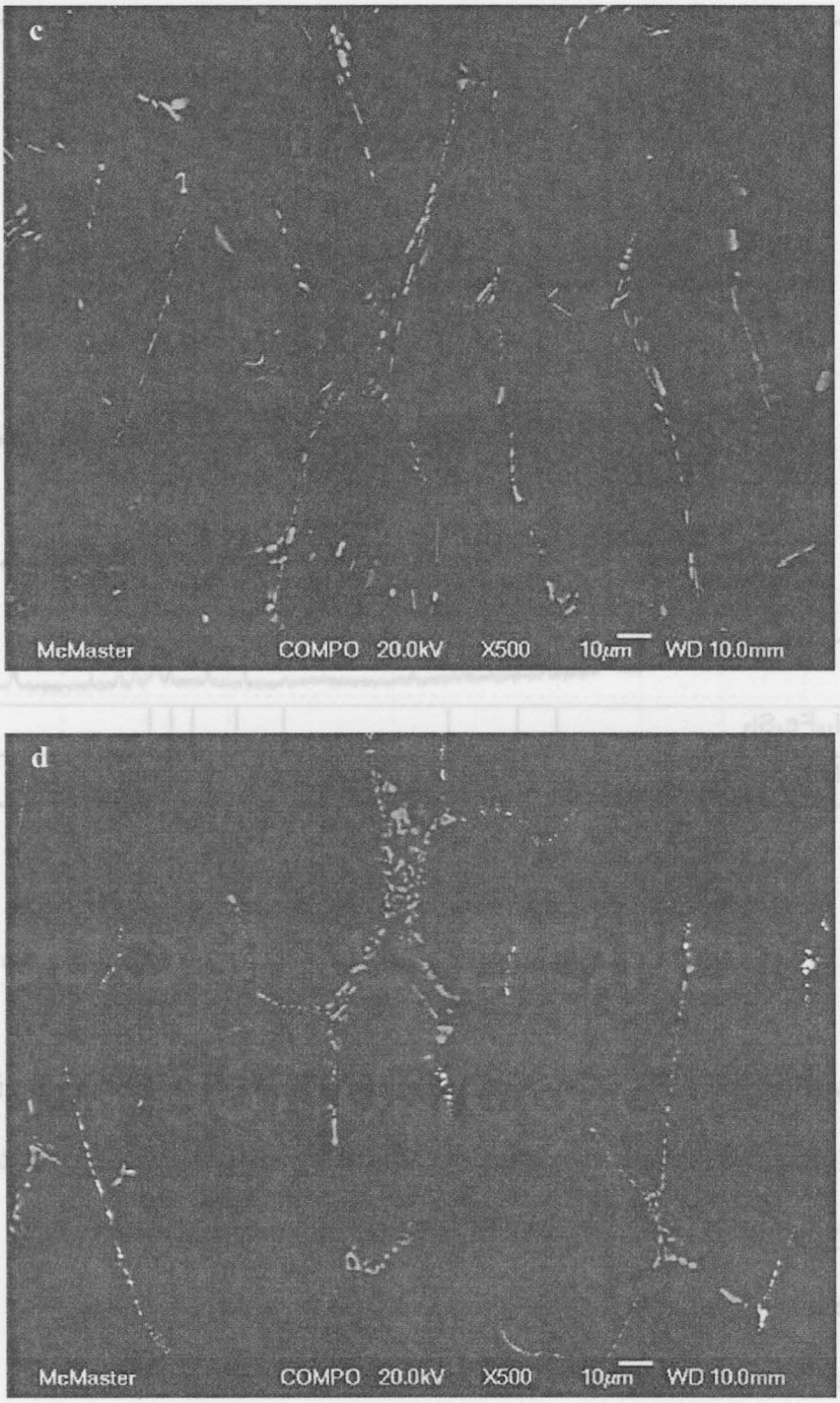

Figure 3-19 Backscattered image of a) RC, b) C1, c) RL and d) L2 alloys in T4 temper

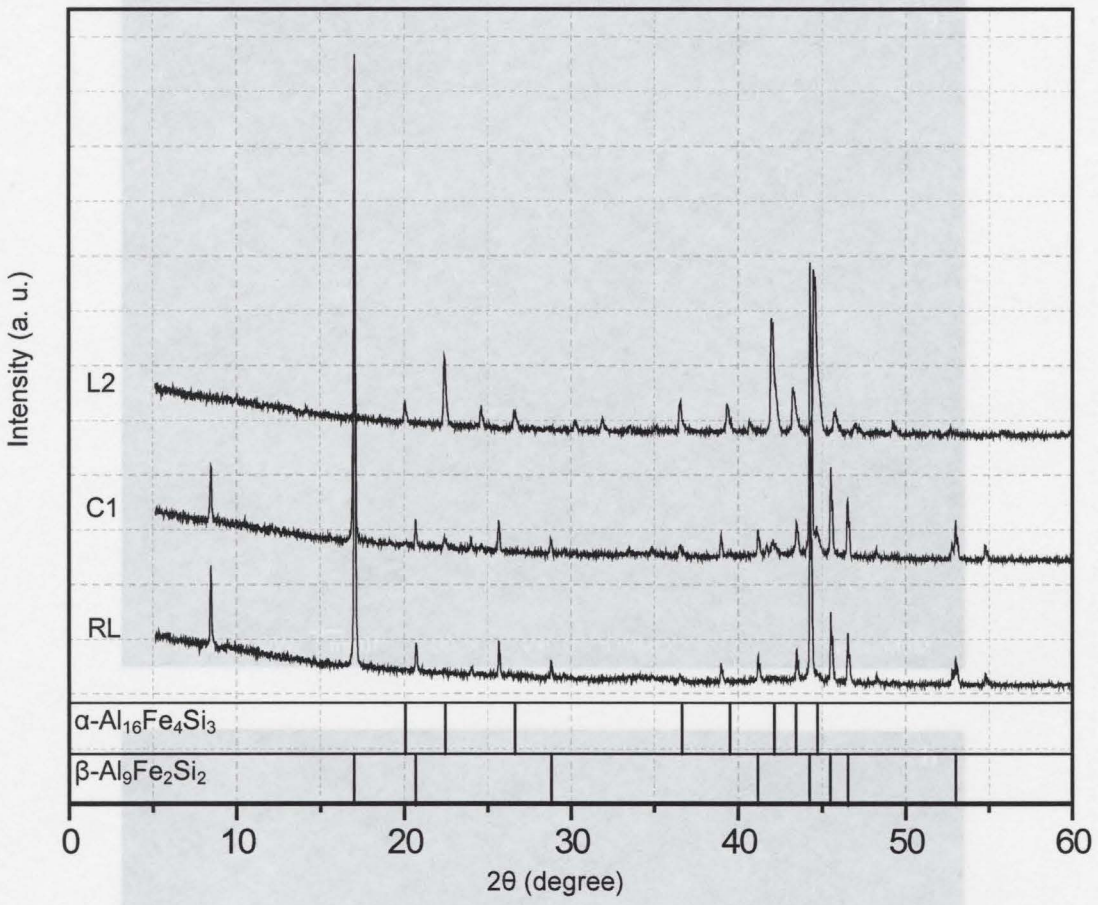

Figure 3-20 XRD patterns of intermetallic phases extracted from RC, C1, and L2 alloy samples in T4 temper

It was explained in section 3.2.1 that the adverse ability of brittle intermetallic phases to initiate voids and consequently induce damage is proportional to their size. Image analysis investigation of particles after thermo-mechanical processing showed that the average size of particles is about 2 μm in all alloys. This can explain why the L2 alloy does not have superior bendability over reference and C1 alloys.

The grain size measurement of the samples in T4 temper also showed no difference between the reference and La-added samples (Table 3-10). It is apparent that

dynamic recrystallization accompanying hot rolling followed by grain growth during solutionizing has eliminated the grain refinement caused by La addition seen in the as-cast case. This observation provides further explanation for the same bendability observed for all alloys.

Table 3-10 Grain size of the alloys in T4 temper measured in transverse plane

Alloy	Grain Size (mm) Transverse Plane t(0°)	t(90°)
RC	0.76±0.07	0.26±0.03
C04	0.56±0.05	0.23±0.02
C07	0.59±0.03	0.26±0.01
C1	0.60±0.05	0.26±0.02
C2	0.72±0.09	0.27±0.02
RL	0.65±0.05	0.28±0.02
L04	0.59±0.04	0.27±0.03
L07	0.74±0.03	0.26±0.02
L1	0.69±0.04	0.24±0.02
L2	0.64±0.05	0.25±0.02

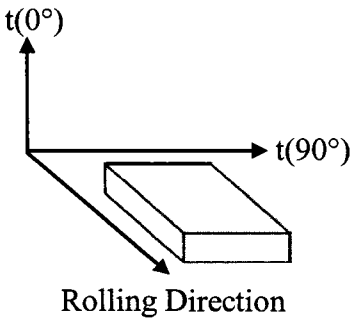

The fact that the deformed and solutionized alloy samples did not show improved bendabilities does not mean that such additions are completely fruitless. For instance, the

effect of microstructural changes in the as-cast stage on the intermediate processes should not be underestimated. Paray *et al.* [1996] examined the addition of Sr to 6061 alloy. They arrived at the same conclusion that there was no difference between modified and Sr-free alloys after thermo-mechanical processing. However, it was possible to extrude Sr-modified alloys at higher rates and the homogenization time prior to extrusion was reduced. It is expected that La addition also leads to improvements in the thermo-mechanical processing and heat treatment of the alloy. This issue needs to be clarified by further investigation.

Considering the importance of microstructural changes in the as-cast stage, it is important to answer two questions:

1- What is the mechanism of modification by La?
2- What prevented cerium from modifying the Fe-bearing intermetallics in the as-cast alloys?

The next chapter is devoted to an attempt to answer these questions.

4 Solidification sequence

4.1 Introduction

In the previous chapter, it was established that the addition of 0.2 wt.% La modifies the Fe-bearing intermetallics from a plate-like shape to the less harmful Chinese script morphology. Based on a hypothesis proposed for the same effect that Sr has, it is speculated that the adsorption of La on the interface of Chinese script particles and liquid inhibits the diffusion of Si into them which, in turn, preserves them from transforming to plate-like particles according to the following reaction [Backerud 1986]:

$$L + Al_8Fe_2Si\ (\alpha) \rightarrow Al + Al_5FeSi\ (\beta)$$

Samuel *et al.* [2001] examined the solidification path of an Al-0.5 wt.% Si-0.15 wt.% Fe alloy with and without Sr addition employing a direct thermal analysis technique similar to that performed by Backerud [1986]. In this method, a thermocouple is simply inserted into the melt and temperature is measured during cooling. Since the formation of solid phases is accompanied by heat release, a change in the tangent of the T-t curve is expected corresponding to the formation of different phases. The first derivative of the temperature over time is used to enhance these thermal effects. The results obtained by

Samuel *et al.* [2001] are shown in Figure 4-1. In these graphs, the first peak (653°C in reference alloy and 652°C in Sr-modified alloy) is associated with the formation of Al dendrites. They associated the next two peaks (628°C and 607°C in the reference alloy and 638°C and 624°C for the alloy containing 0.08 wt.% Sr) to the formation of Chinese script particles and their transformation to plate-like particles respectively. In their interpretation, the second peak is less pronounced in the Sr-added alloy which corroborates the modification mechanism of Sr mentioned above.

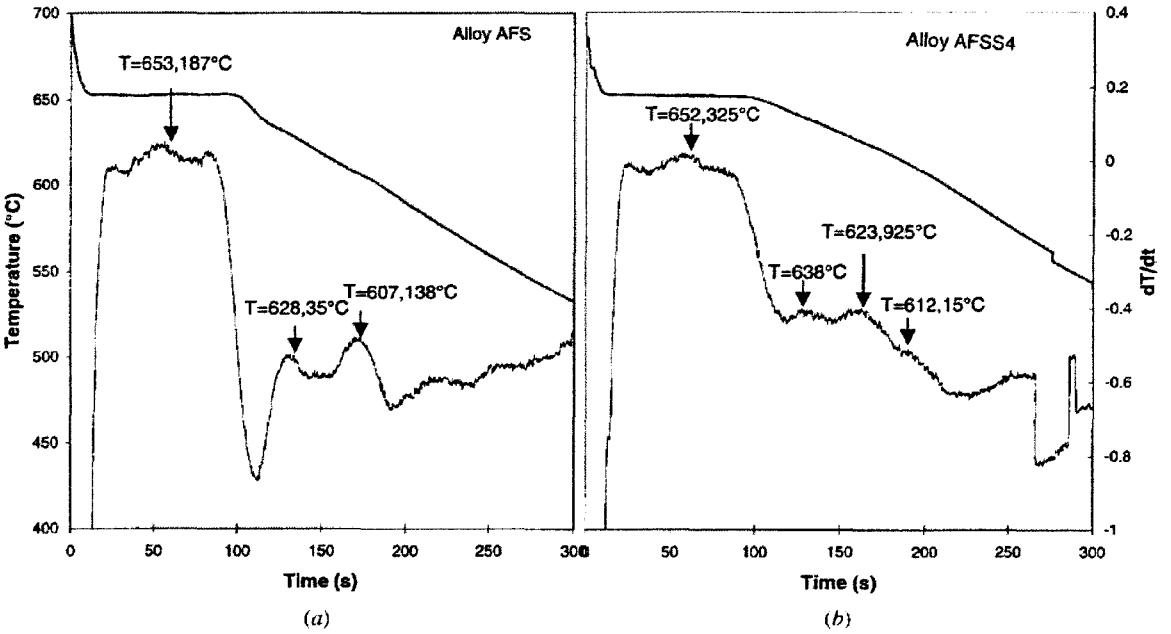

Figure 4-1 Cooling curve and its first derivative of a) reference and b) Sr-containing alloys examined by Samuel *et al.* [2001]

Such a direct thermal analysis technique is used in the present investigation in order to verify whether the surface adsorption is the mechanism by which La modifies the Fe-bearing intermetallics.

4.2 Experimental procedure

The same reference alloy mentioned in the previous chapter (Al - 0.7 wt.% Si - 0.7 wt.% Mg - 0.45 wt.% Fe - 0.2 wt.% Cu) was chosen. Weighted amounts of 99.9 wt.% pure Al, Mg, Si, Fe, and Cu were melted in a graphite crucible using induction heating to prepare 240 grams of the reference alloy. In the same manner, La-treated alloys were prepared containing 0.2 wt.% La. La was also added to the melt in the form of 99.9 wt.% pure metal. The choice of La concentration was based on the observed results presented in the previous chapter. The melt was heated up to 750°C and held at this temperature for 15 minutes. During this time, the melt was stirred several times with a graphite rod to ensure the dissolution of alloying elements and achieve homogeneity throughout the melt.

Three solidification modes were employed in order to achieve different cooling rates. They were:

1. In a graphite crucible
2. In a graphite crucible wrapped in 20 mm thick alumina blanket
3. In a clay mold pre-heated to 400°C

In the first two modes, the melt was prepared in the graphite crucible and cooled in the same crucible after turning off the furnace. In the third mode, first the melt was prepared in the graphite crucible and then poured into the clay mold. No special measures (water chill, compressed air flow, etc.) were employed to cool down the melt. The sizes and shapes of the clay and graphite crucibles are shown in Figure 4-2.

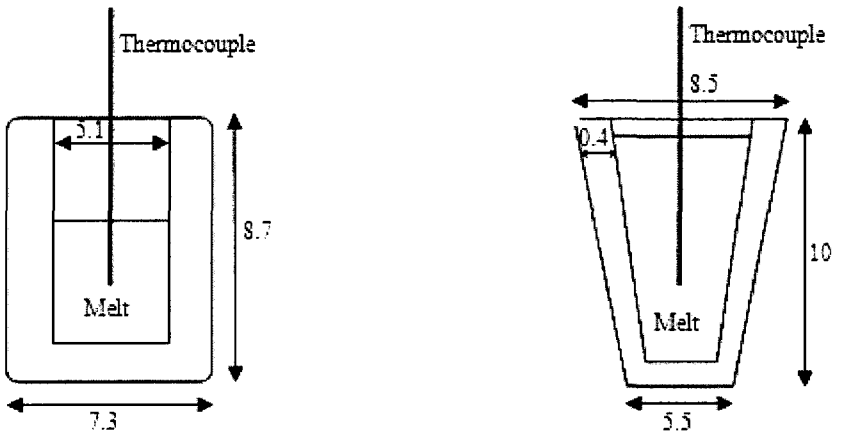

Figure 4-2 Schematic depiction of thermocouple configuration in a) graphite crucible and b) clay crucible used to cast alloys (sizes in cm)

The secondary dendrite arm spacing (SDAS) can be used as a measure of the local cooling rate during solidification, the smaller the SDAS the higher the cooling rate. The results of the SDAS measurement presented in Table 4-1 indicate that the cooling rate is similar in the second and third mode while a higher cooling rate is achieved in the first mode. The details of this measurement are provided in appendix III.

Table 4-1 chemical compositions (wt.%) and SDAS of investigated alloys

Mode		Mg	Si	Fe	Cu	La	Al	SDAS (μm)
1	R	0.724	0.751	0.51	0.2	-	Rem.	115±5
	L	0.7	0.84	0.5	0.2	0.2		117±3
2	R	0.78	0.95	0.56	0.24	-		180±2
	L	0.8	0.9	0.62	0.24	0.21		182±2
3	R	0.77	0.81	0.6	0.2	-		177±5
	L	0.79	0.88	0.58	0.22	0.21		179±3
Water-chilled copper mold		0.8	0.95	0.5	0.2	0.2		24±1

To verify a hypothesis that will be explained in 4.4.2, a La-containing alloy was prepared using the water-chilled copper mold previously described in section 3.5.1. The direct thermal analysis was not performed for this alloy since very high cooling rates achieved in this experiment prevents an efficient data acquisition. The composition of the alloys verified by glow discharge optical emission spectroscopy is presented in Table 4-1.

The temperature variation during solidification was measured by a K type thermocouple. As shown in Figure 4-2, the thermocouple was inserted in the centre line of the crucible half way into the melt. Data were recorded by a data acquisition system at 100 s^{-1} sampling rate. The recorded temperature-time data were differentiated using the Origin software. The data were smoothed by adjacent averaging prior to differentiation so that an acceptable peak/noise ratio is achieved.

Samples for metallographic investigation were cut from the vicinity of the thermocouple tip. The samples were hot mounted in Lucite and ground with SiC papers. The final polishing steps were carried out using water-free diamond solutions to preserve Mg_2Si particles from being etched away. The intermetallic particles were characterized using optical and scanning electron microscopy (SEM) equipped with an energy dispersive spectroscopy (EDS) detector. The intermetallic particles of alloys solidified in the insulated graphite crucible were extracted by phenol dissolution technique mentioned in section 3.5.2. The extracted particles were examined using X-ray diffraction analysis.

4.3 Results

The first derivative of the cooling curves of the reference and La-added alloys solidified in the insulated graphite crucible is shown in Figure 4-3. There are five peaks that are common between both alloys, namely a, b, c, d and e. The major difference between the reference and La-treated alloys is manifested in the presence of a peak dubbed "x" in the graph of the La-containing alloy which is not seen in the curve of the reference alloy. From the duration of the peak "a" in the temperature-time curves (not shown here), it is obvious that it corresponds to the formation of Al dendrites. The temperature of this peak, 648°C, very well coincides with the predictions of Scheil calculations. The occurrence of the other peaks is connected with the formation of the intermetallic particles. A careful characterization of the phases in the cast microstructure

is needed in order to associate these peaks with the formation of intermetallic phases and derive the solidification sequence of each alloy.

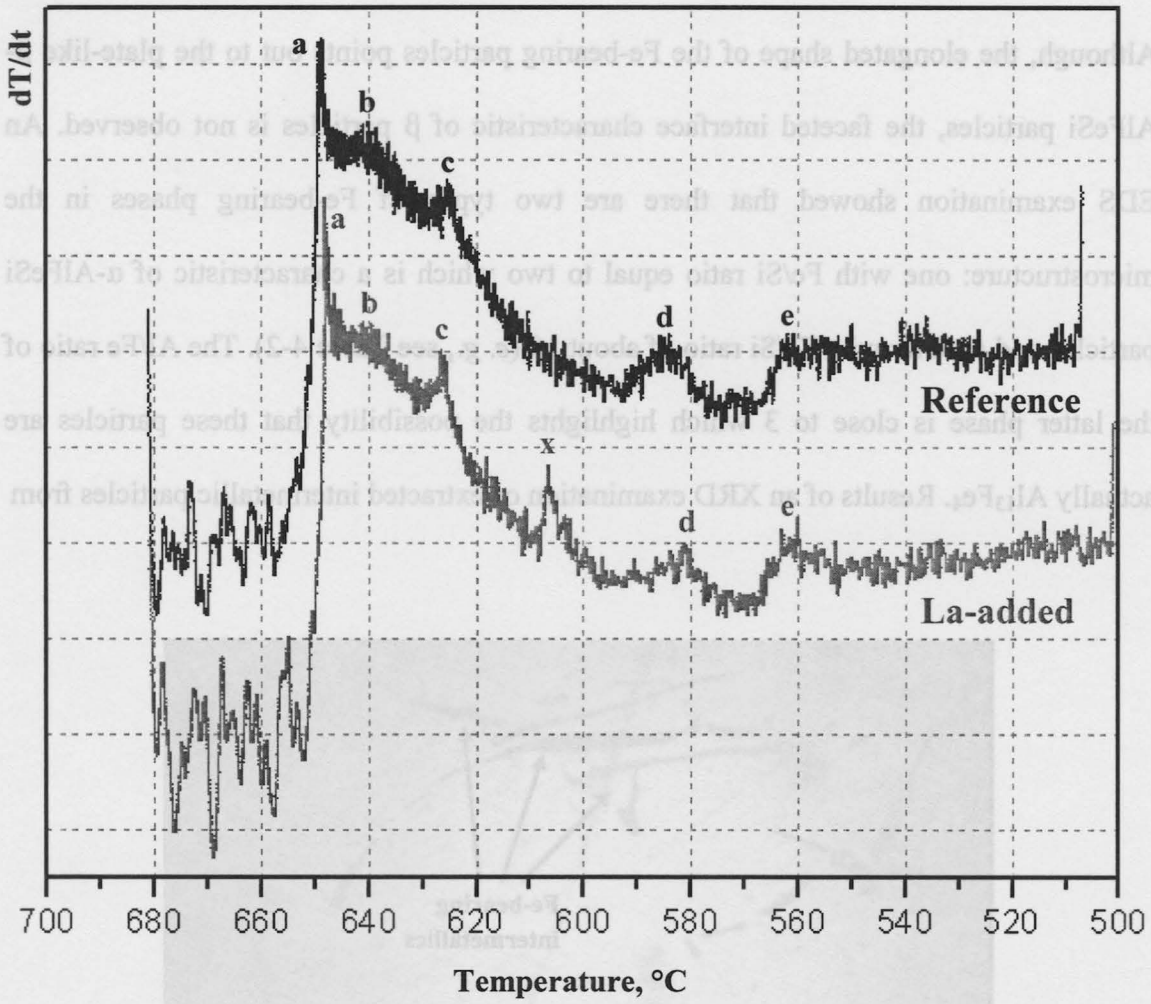

Figure 4-3 First derivatives of cooling curves of alloys solidified in insulated graphite crucible. The curve for La-added alloy is shifted down for clarity

It must be mentioned that the number and position of the mentioned peaks are not affected by the solidification mode. The results of the mode 2 solidification are shown as a representative of all recorded curves.

A typical microstructure of the reference alloy revealed by optical microscopy is shown in Figure 4-4. It consists of elongated grey particles which are Fe-bearing intermetallics, Mg_2Si particles which have a dark blue color, and eutectic regions. Although, the elongated shape of the Fe-bearing particles points out to the plate-like β-AlFeSi particles, the faceted interface characteristic of β particles is not observed. An EDS examination showed that there are two types of Fe-bearing phases in the microstructure: one with Fe/Si ratio equal to two which is a characteristic of α-AlFeSi particles and another with Fe/Si ratio of about 10 (*e. g.*, see Table 4-2). The Al/Fe ratio of the latter phase is close to 3 which highlights the possibility that these particles are actually $Al_{13}Fe_4$. Results of an XRD examination of extracted intermetallic particles from

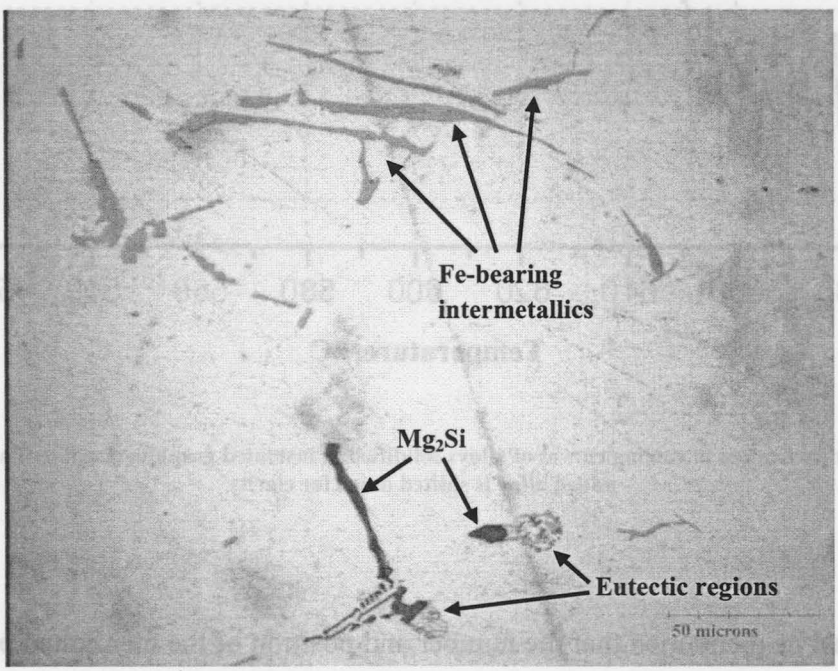

Figure 4-4 An optical micrograph of the reference sample solidified in the insulated graphite crucible

this sample confirmed the presence of $Al_{13}Fe_4$ phase (Figure 4-5). The results of the EDS analysis suggest that Si dissolves in this phase to some extent. The ability of this phase to accommodate Si is reported by Khalifa *et al.* [2003].

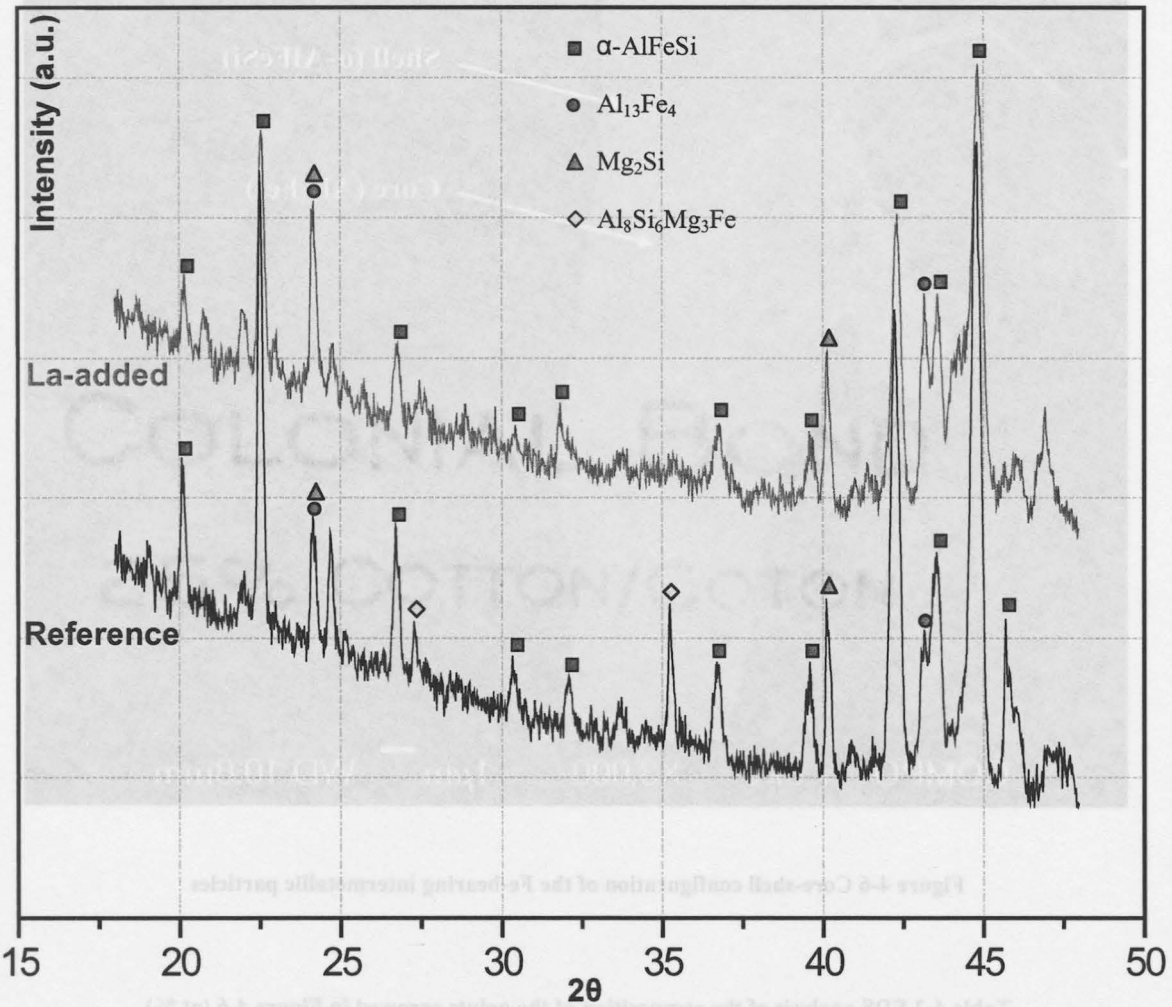

Figure 4-5 XRD patterns of intermetallic phases extracted from the reference and La-containing alloy samples solidified in insulated graphite crucible

Both types of Fe-bearing phases were seen to exist as separate particles. However, in a majority of cases the α-AlFeSi particles existed as an extension to the $Al_{13}Fe_4$

particles or formed an envelope around them (Figure 4-6). Such a "core-shell" microstructure is a characteristic of peritectic reactions. From this observation it can be concluded that the $Al_{13}Fe_4$ forms first, and later, transforms to α-AlFeSi through a peritectic reaction.

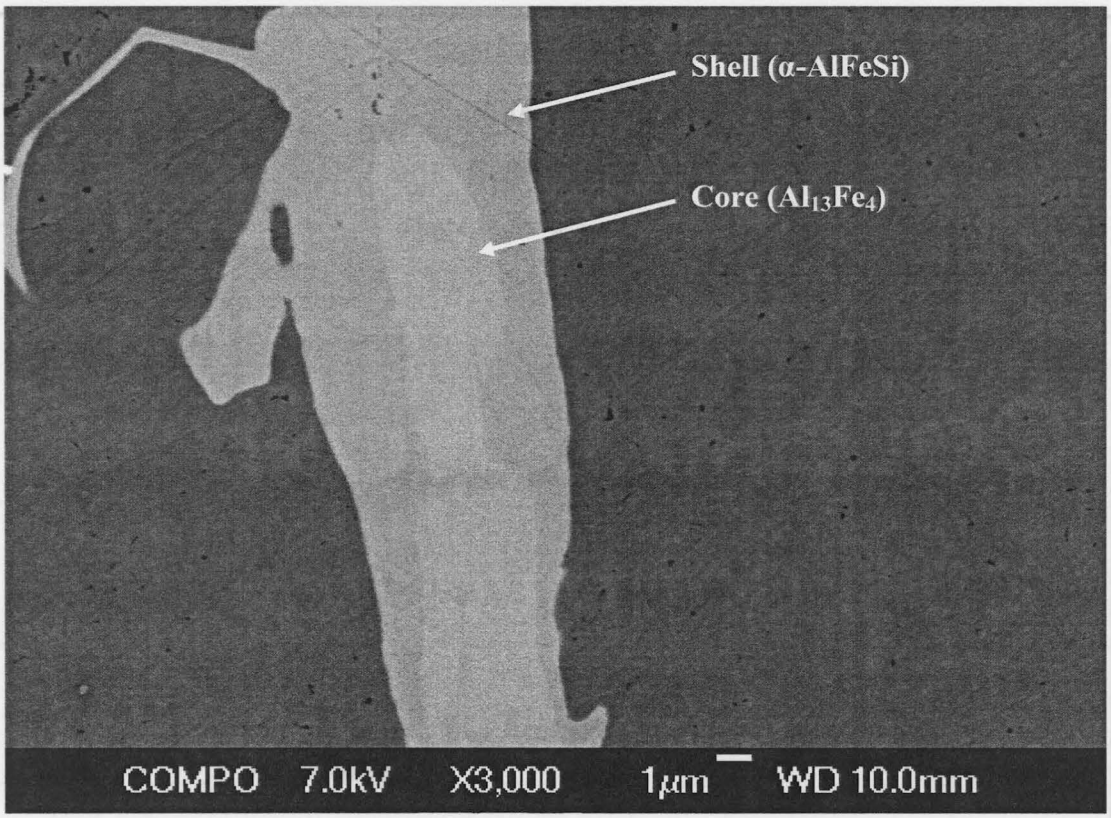

Figure 4-6 Core-shell configuration of the Fe-bearing intermetallic particles

Table 4-2 EDS analysis of the composition of the points arrowed in Figure 4-6 (at.%)

	Al	Si	Fe	Mg	Cu
Core	70	10.3	18.1	-	1.6
Shell	75.6	1.8	22.6	-	-

An example of the multi-phase regions is shown at high magnification in Figure 4-7. The presence of several phases in these regions resembles the final stage of solidification where the last pockets of liquid solidify by a eutectic reaction. The compositions of the phases present in this region are given in Table 4-3. They are likely quaternary π-$Al_8Si_6Mg_3Fe$ (elongated gray particles), pure Si (dark spherical particles), and two unknown AlSiMgCu phases (bright particles). The EDS examination of the dark spherical particles suggests the presence of Al; however, this cannot be true since no binary intermetallic phases exist in the Al-Si phase diagram. The Al signal is detected from the matrix below the particles.

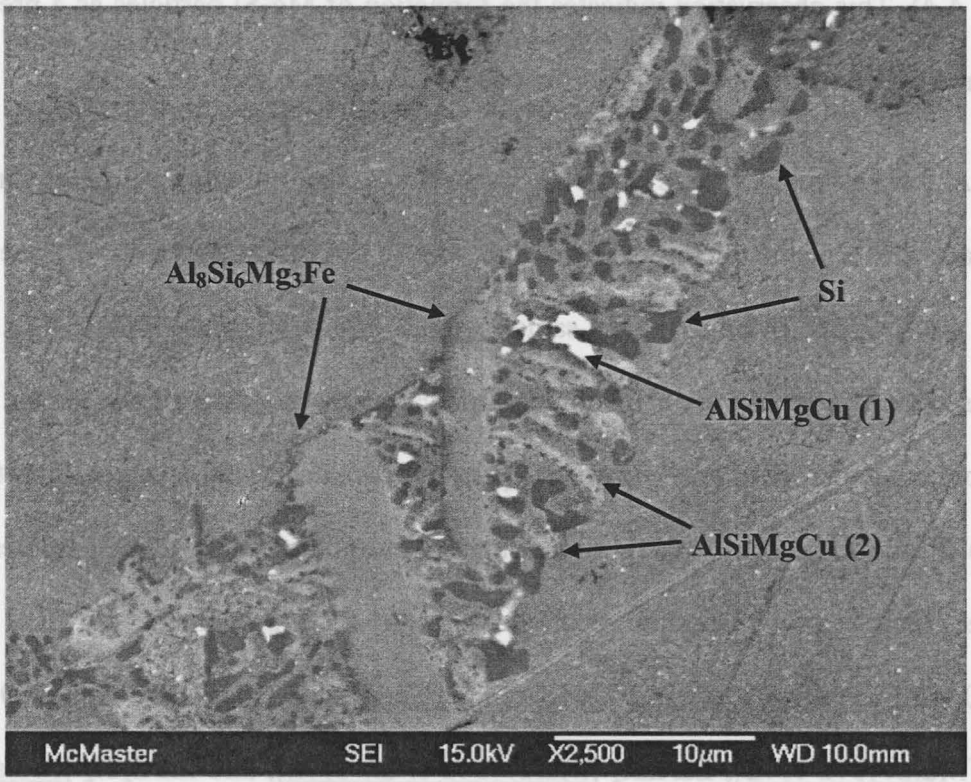

Figure 4-7 Secondary electron image of a eutectic region in the reference alloy at higher magnification containing

Table 4-3 EDS analysis of the composition of the particles composing the eutectic region in the reference alloy (at.%)

	Al	Si	Mg	Fe	Cu
π- $Al_8Si_6Mg_3Fe$	48.8	29.9	15.9	5.4	-
Si	37.7	61.4	0.6	-	0.3
AlSiMgCu (1)	71	11.5	4.8	-	12.7
AlSiMgCu (2)	56.9	22.4	16.4	-	4.3

The Mg_2Si particles were seen to assume different shapes. Bulky, elongated and Chinese script morphology of these particles existed throughout the microstructure. In most cases, the eutectic regions were observed to be adjacent to the Mg_2Si particles (Figure 4-4). This observation indicates the formation of Mg_2Si particles as a preceding reaction to the completion of the solidification by the eutectic reaction.

A few differences were observed in the La-containing alloy samples. Firstly, a new phase with a distinctive brown color appeared in optical micrographs of these alloys (Figure 4-8a). An SEM image of the same region is shown in figure Figure 4-8b. These particles are now seen as very bright objects indicating the presence of an element with a high atomic number. EDS analysis of such particles revealed that they are AlSiLa ternary paricles (Table 4-4). Both bulky and elongated morphologies of these particles were observed. Four ternary phases are reported for the Al-La-Si system: $La(Al_{1-x}Si_x)_2$ ($0.075 < x < 0.18$) [Muravyova *et al.* 1972, Raman & Steinfink 1967], $La(Al_xSi_{1-x})_2$ ($0 \leq x \leq 0.69$) [Muravyova 1972], $LaAlSi_2$ [Muravyova *et al.* 1972], and $LaAl_2Si_2$ [Muravyova 1971, Muravyova *et al.* 1972, Muravyova 1972]. The composition of these particles measured by EDS seems to comply best with the tetragonal $La(Al_{1-x}Si_x)_2$ phase.

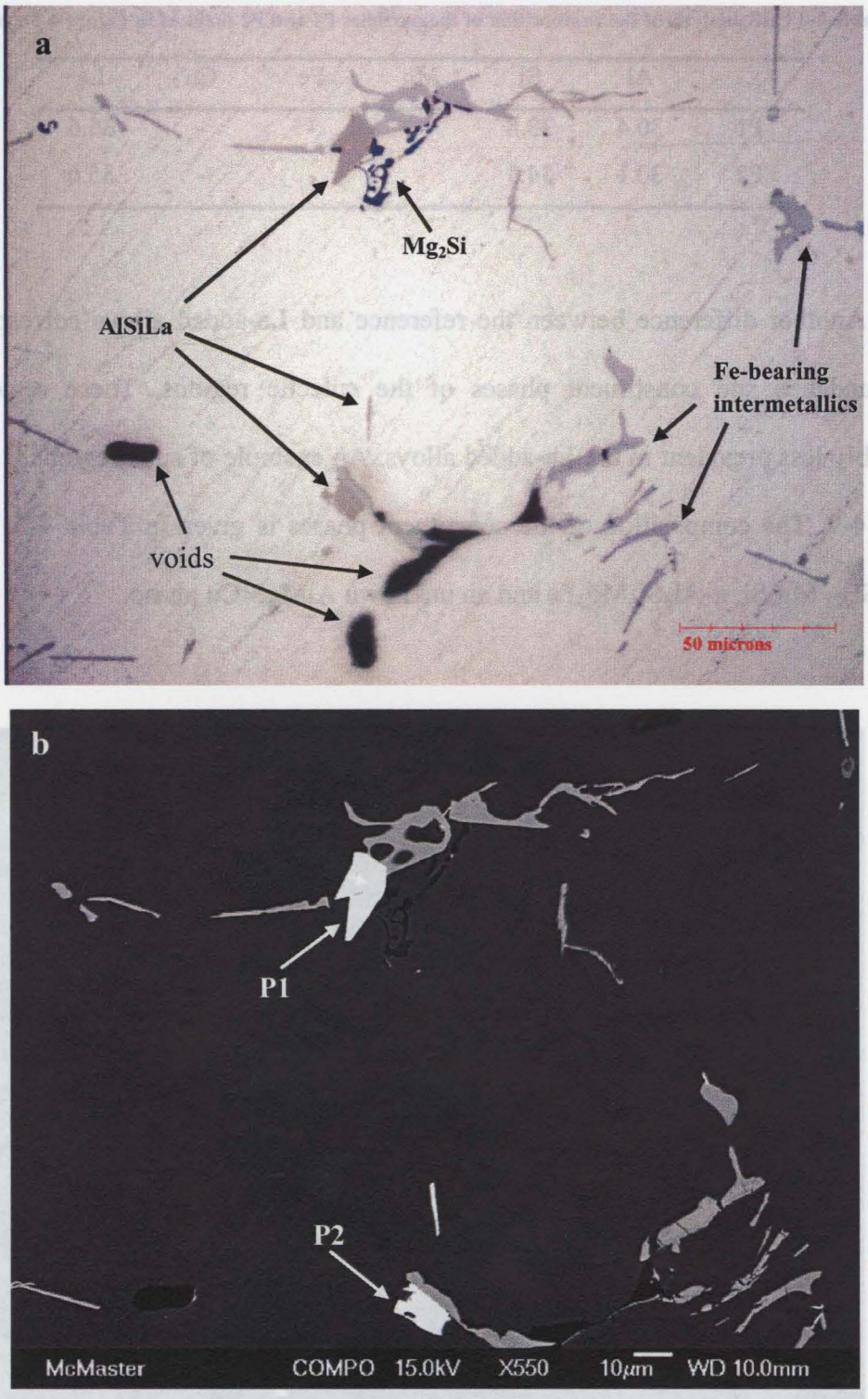

Figure 4-8 a) An optical micrograph of the La-added sample solidified in the insulated graphite crucible b) Backscattered image of the same region as (a).

Table 4-4 EDS analysis of the composition of the particles P1 and P2 marked in Figure 4-8b (at.%)

	Al	Si	Mg	Fe	Cu	La
P1	30.4	33.8	-	-	-	35.6
P2	30.1	34.3	-	-	-	35.6

Another difference between the reference and La-added alloys corresponded to the abundance and constituent phases of the eutectic regions. These regions were noticeably less prevalent in the La-added alloys. An example of such regions is shown in Figure 4-9. The composition of the constituent phases is given in Table 4-5. They are $La(Al,Si)_2$, Mg_2Si, π-$Al_8Si_6Mg_3Fe$ and an unknown AlMgSiCu phase.

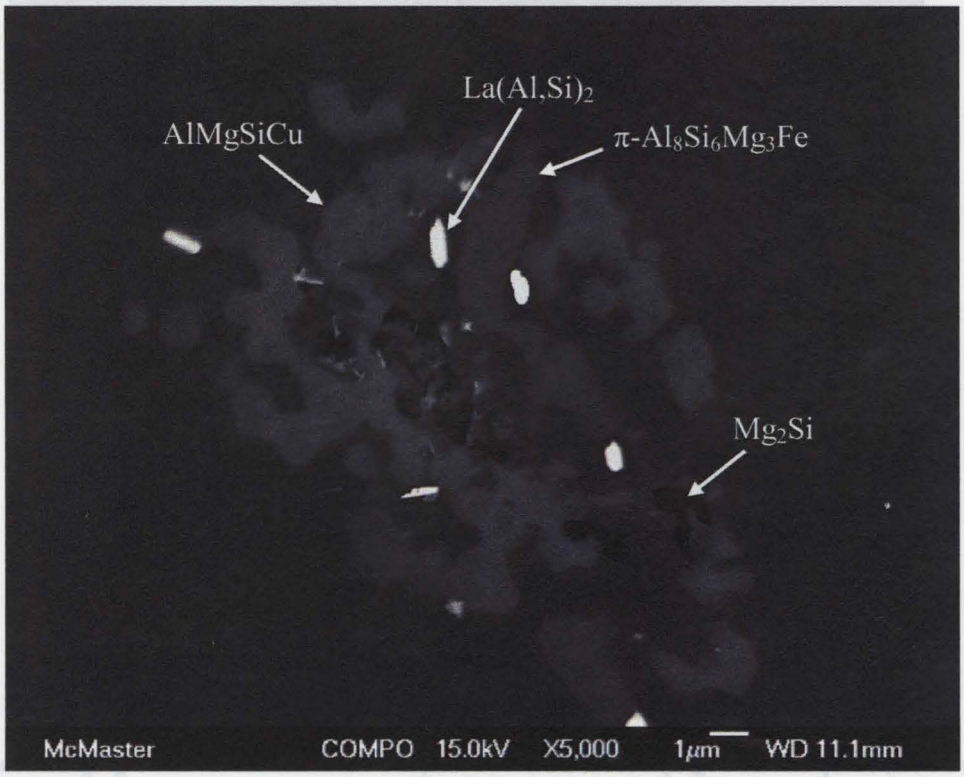

Figure 4-9 Backscattered image of a eutectic region of a La-containing alloy solidified in a clay crucible

Table 4-5 EDS analysis of the particles in the eutectic region of the La-added alloy (at.%)

	Al	Si	Mg	Fe	Cu	La
π- $Al_8Si_6Mg_3Fe$	59.5	23.9	13.8	3.8	-	-
Mg_2Si	6.4	32.8	60.8	-	-	-
$La(Al,Si)_2$	31.8	36.6	2.4	-	-	29.2
AlMgSiCu	29.7	30.7	32.4	-	7.2	-

No difference was observed between the reference and La-containing alloys in terms of the Fe-bearing intermetallic compounds. Both $Al_{13}Fe_4$ and α-AlFeSi particles existed in the microstructure mostly in the form of the core-shell configuration shown in Figure 4-6.

4.4 Discussion

4.4.1 Solidification path

4.4.1.1 Reference alloy

In addition to the Al matrix, three kinds of particles and a eutectic region were found in the microstructure of the reference alloy. It is already discussed that the first peak (a) is associated with the formation of the Al dendrites. The eutectic regions are formed at the final stage of the solidification. This means that the last peak (e) is caused by the formation of these regions. Although the fraction of the eutectic regions is small, the simultaneous formation of several phases releases enough heat to cause such an

intense peak. Microstructural observations provided three hints that can be used to identify the remaining peaks. They are:

1- $Al_{13}Fe_4$ forms prior to the α-AlFeSi phase,

2- $Al_{13}Fe_4$ transforms to α by a peritectic reaction, and

3- Mg_2Si forms in the later stages of the solidification prior to the final eutectic reaction.

Coupling these observations with the remaining peaks, it can be deduced that peak "d" is caused by the formation of the Mg_2Si particles and peaks 'b" and "c" are associated with the formation of the $Al_{13}Fe_4$ phase and its transformation to the α-AlFeSi phase respectively. To verify these conclusions, the results of the Scheil-Gulliver calculations and previous experimental investigations are taken into account. The experimental investigations on the solidification paths of alloys belonging to the 6xxx series family are summarized in Table 4-6. The predictions of the Scheil-Gulliver method for the reference alloy are already given in section 3.1 (page 65).

Both calculated and experimentally derived paths (except for Backerud [1986]) indicate that the $Al_{13}Fe_4$ is the first intermetallic phase to form during solidification. The peritetic transformation of this phase to the α-AlFeSi phase is also commonly mentioned as the next reaction. The formation of the Mg_2Si is predicted to start at 573°C based on the Scheil calculations. All the experimental observations agree that this phase begins to solidify at temperatures around 580°C. These results confirm the conclusions drawn for peak b, c, and d.

Table 4-6 Experimental investigations of the solidification sequence of 6xxx series Al alloys

Composition (wt.%)	Reaction	Temperature (°C)	Reference
AA 6063: 0.4 Si-0.43 Mg - 0.2 Fe	$L \rightarrow Al$ (dendrites)	655	[Backerud 1986]
	$L \rightarrow Al + \alpha\text{-AlFeSi}$	618 - 615	
	$L + \alpha\text{-AlFeSi} \rightarrow Al + \beta\text{-AlFeSi}$	612	
	$L \rightarrow Al + \beta\text{-AlFeSi}$	612 - 576	
	$L \rightarrow Al + \beta\text{-AlFeSi} + Mg_2Si$	576	
0.6 Si - 0.8 Mg - 0.3 Fe	$L \rightarrow Al$ (dendrites)	651	[Hsu *et al.* 2001]
	$L \rightarrow Al + Al_{13}Fe_4$	631	
	$L + Al_{13}Fe_4 \rightarrow Al + \alpha\text{-AlFeSi}$	627	
	$L \rightarrow Al + \alpha\text{-AlFeSi}$	627-586	
	$L \rightarrow Al + \alpha\text{-AlFeSi} + Mg_2Si$	586	
Comercial AA 6111: exact composition is not given	$L \rightarrow Al$ (dendrites)	650	[Chen & Langlais 2000]
	$L \rightarrow Al + Al_6Fe$ (or Al_3Fe)	642	
	$L + Al_6Fe$ (or Al_3Fe) $\rightarrow Al + \alpha\text{-Al(FeMn)Si}$	633	
	$L \rightarrow Al + \alpha\text{-AlFeSi}$	633 – 606	
	$L + \alpha\text{-Al(FeMn)Si} \rightarrow Al + \beta\text{-Al(FeMn)Si}$	606	
	$L \rightarrow Al + Mg_2Si$	580	
	$L \rightarrow Al + Mg_2Si + Si$	557	
	$L + Mg_2Si + Si \rightarrow Al + AlMgSiCu$	536	
	$L + Mg_2Si \rightarrow Al + AlMgSiCu + Al_2Cu$	529	
	$L \rightarrow Al + Mg_2Si + Al_2Cu$	508	
	$L \rightarrow Al + AlMgSiCu + Al_2Cu + Si$	478	

The complete solidification path of the reference alloy is:

1. $L \rightarrow Al$ (dendrites) 648°C
2. $L \rightarrow Al + Al_{13}Fe_4$ 643°C
3. $L + Al_{13}Fe_4 \rightarrow Al + \alpha\text{-AlFeSi}$ 628°C
4. $L \rightarrow Al + \alpha\text{-AlFeSi} + Mg_2Si$ 588°C
5. $L \rightarrow Al + \pi\text{-}Al_8Si_6Mg_3Fe + Si + AlSiMgCu(1) + AlSiMgCu(2)$ 565°C

The temperature at which a peak begins to rise is chosen as the temperature of the corresponding reaction. For each peak, the three solidification modes are considered and the average temperature is reported here.

It was noted that the formation of the $Al_{13}Fe_4$ phase was not reported by Backerud [1986], instead, he proposed that the formation α-AlFeSi phase by a eutectic reaction is the first step. Such a displacement of $Al_{13}Fe_4$ with the α-AlFeSi phase is quite possible at high cooling rates. Westengen [1982] mentioned that the $Al_{13}Fe_4$ phase only formed at cooling rates below 1 K/s. Griger *et al.* [1989] examined intermetallic phases in an Al-0.5 wt.% Fe- 0.2 wt.% Si alloy semi-continuously cast with different cooling rates. They observed the displacement of $Al_{13}Fe_4$ with the α-AlFeSi phase at cooling rates higher than 2.3 K/s. The growth mechanism of these two phases is taken into account to explain this phenomenon. The growth of the faceted $Al_{13}Fe_4$ phase is governed by the attachment of the atoms to the particle while the diffusion of solutes is the rate controlling step in the growth of the α-AlFeSi phase. At high cooling rates, the atomic attachment barrier

becomes harder to overcome which favors the formation of α-AlFeSi instead of $Al_{13}Fe_4$ [Griger *et al.* 1989].

A simple thermodynamic calculation of the driving forces of the onset of precipitation (DGM) of the intermetallic phases illustrated in Figure 4-10 shows that at very high supercoolings (corresponding to high cooling rates) the precipitation of the α phase from melt is favored over the formation of $Al_{13}Fe_4$ phase.

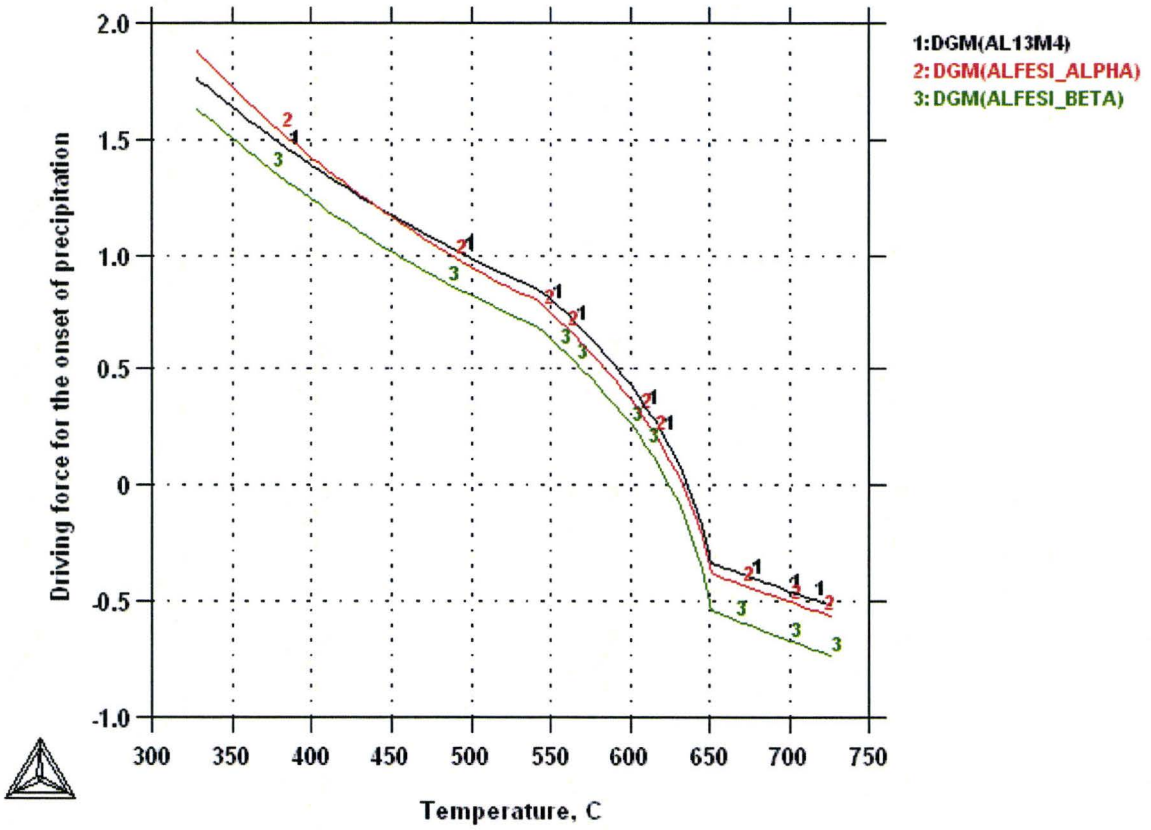

Figure 4-10 Driving forces of the onset of precipitation of Fe-bearing intermetallics at different temperatures

A surprising difference is observed between the results of this experiment and those presented in chapter 3 regarding the cast microstructure of the reference alloy. While the plate-like β-AlFeSi particles are the dominant Fe-bearing intermetallics in the reference alloys cast into the water-chilled copper mold, this phase is not seen in any of the reference alloys prepared for the thermal analysis. As mentioned earlier, β is believed to form via a peritectic reaction between the liquid and the α phase (*e.g.* see [Backerud 1986] in

Table 4-6 and Scheil-Gulliver calculations). However, if this was the case then very low cooling rates utilized in the present investigation should have favored its formation. Alternatively, it is possible that at higher cooling rates the β particles form from the melt by a eutectic type reaction (Liquid→ Al + β -AlFeSi). Hsu *et al.* [2001] investigated the solidification sequence of an Al - 0.8 wt.% Mg - 0.6 wt.% Si - 0.3 wt.% Fe alloy with DSC at a cooling rate of 5 K/min (Table 4-6). A TEM investigation of the solidified samples revealed that the β-AlFeSi particles were not a constituent of the microstructure. Meredith *et al.* [2002] examined directional solidification of the same alloy and reported that β was not formed at growth velocities slower than 80 mm/min while it was the dominant phase at higher velocities (80-120 mm/min). Based on these observations and the results of the present investigation it can be concluded that α is the stable AlFeSi phase in this alloy and β is actually a metastable phase which forms preferentially at high cooling rates. This explains why most of the reported instances of existence of β correspond to the DC cast alloys that are characterized with cooling rates of about 10 K/s.

4.4.1.2 La-added alloy

All the reactions mentioned for the reference alloy seem to take place in the alloy containing 0.2 wt.% La. Even the temperatures for these reactions almost coincide (± 2°C). The major disparity between the reference and the La-added alloys is the presence of a peak at 607°C for the La-treated alloy which does not occur in the curve of the reference alloy. From the microstructural viewpoint, the presence of La-bearing particles is the major difference between the reference and the La-added alloys. It can be concluded that the peak at 607°C is attributed to the formation of the $La(Al,Si)_2$ compound. The following solidification path is proposed for the La-added alloy.

1. $L \rightarrow Al$ (dendrites) 648°C
2. $L \rightarrow Al + Al_{13}Fe_4$ 642°C
3. $L + Al_{13}Fe_4 \rightarrow Al + \alpha\text{-AlFeSi}$ 627°C
4. $L \rightarrow Al + \alpha\text{-AlFeSi} + La(Al,Si)_2$ 607°C
5. $L \rightarrow Al + La(Al,Si)_2 + \alpha\text{-AlFeSi} + Mg_2Si$ 586°C
6. $L \rightarrow Al + La(Al,Si)_2 + \pi\text{-}Al_8Si_6Mg_3Fe + Mg_2Si + AlMgSiCu$ 566°C

4.4.2 Mechanism of modification by La addition

The thermal analysis experiment in this investigation was performed on the basis that the α-AlFeSi particles transformed to the β-AlFeSi particles as a result of a pretectic

reaction and the effect of La on this pretectic reaction was expected to be caught. However, it turned out that the β-AlFeSi particles were not a constituent of the microstructure of either the reference or the La-added alloys solidified in graphite or clay crucibles (characterized with very slow cooling rates). It was concluded that the above peritectic reaction is highly improbable to occur in this alloy. Consequently, the surface adsorption mechanism cannot be validated as the modification mechanism of La.

Nevertheless, it is a fact that β does form in processes involving higher cooling rates such as DC casting. The presence of β in the reference alloys cast into the water-chilled copper mold confirms the promotion of β by high cooling rates. An important factor that should not be overlooked here is the composition of the alloy. It is observed that even in the case of DC casting, low ratios of Si content/Fe content of the melt will result in the formation of the α-AlFeSi particles [Dons 1985, Langsrud 1990, Griger & Stefaniay 1996, Tanihata *et al.* 1999, Khalifa *et al.* 2003]. Combining this information with the results of the thermal analysis experiment provides a different insight into the mechanism of modification by lanthanum addition. The most significant difference between reference and La-added alloys in the thermal analysis experiment was the formation of $La(Al,Si)_2$ particles in the presence of La. Such particles were also seen in the La-containing alloys cast into the water-chilled copper mold. This compound contains 14 wt.% Si and the temperature at which it starts to form (607°C) is very close to the temperature of the formation of β suggested by Backerud [1986] (612°C) and sits above the temperature of the β formation predicted by Scheil-Gulliver (598°C). It can be hypothesized that the formation of $La(Al,Si)_2$ locks in a fraction of Si atoms and changes

the Si/Fe content of the remaining melt to smaller values which is in favor the α-AlFeSi formation. Pure Si particles seen as a constituent of eutectic regions in the reference alloy were not present in the eutectic regions of the La-added alloy. Moreover, a smaller fraction of eutectic regions in La-added alloy was observed. These results support the consumption of Si by the formation of La-bearing particles.

The inability of Ce to modify Fe-bearing intermetallics may be explained according to this proposed mechanism. Si content of the Ce-added alloys cast into the water-chilled copper mold were at least 0.2 wt.% higher than that in the alloys modified by La (Table 3-3). Despite the fact that Ce-bearing intermetallics existed in the microstructure of these alloys, it is deemed that Si surplus has been enough to induce the formation of β particles. In other words, it is not intrinsic capability of Ce or La but Si content which determines the ability of these elements to modify Fe-bearing intermetallics.

As an attempt to test this hypothesis, a La-added alloy with high silicon content (0.9 wt.%) is cast into the water-chilled copper mold. If Si content is the controlling factor then the β-AlFeSi phase is expected to become the dominant intermetallic particle even in the presence of La. An optical micrograph of this alloy is shown in Figure 4-11. It is apparent that despite the increased Si content, Chinese script particles are still the dominant Fe-bearing phase in the microstructure. Clearly, there is something intrinsically special about La which makes it capable of modifying the AlFeSi particles.

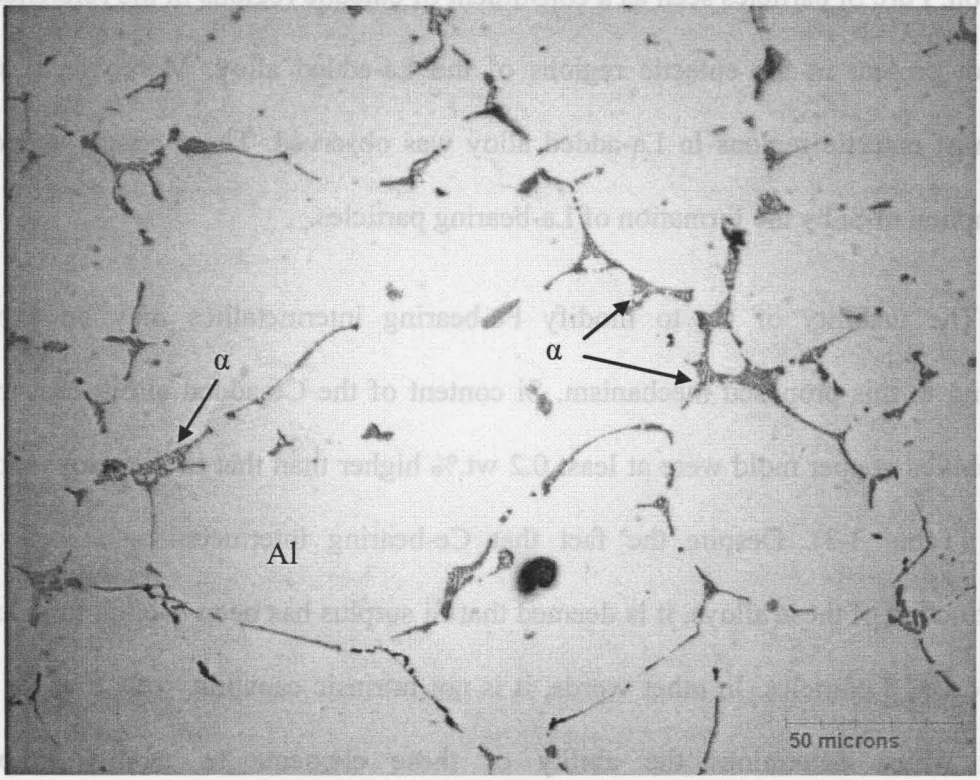

Figure 4-11 An optical micrograph of the La-added alloy containing high concentration of Si

Despite the efforts carried out in the present investigation, the modification mechanism of La remained unknown. The reasons behind the inability of Ce to modify intermetallic compounds were also left unresolved. It was intended to employ first principle calculations to examine the interaction between La and Ce atoms and the surface of the Fe-containing intermetallics. However, a private communication with J. Hoyt[3] clarified that such attempts will fail since these calculations are not suited to

[3] Associate Professor, Dept. of Materials Sci. & Eng, McMaster Univ. Hamilton, ON.

handle elements that have electrons in their f orbital. Exploring the above unresolved mysteries remains an open field for further investigations.

5 Conclusions

The objective of the present investigation was twofold: to evaluate the possibility of fabricating a two-phase material containing aluminum and equally ductile RM intermetallic phases and to improve the bendability of the 6xxx series Al alloys by small additions of rare-earth elements.

For the first part, the Al-La-Mg system was chosen. The objective was to predict whether the binary ductile phase LaMg is formed during casting. This could be done if a thermodynamic database containing the Gibbs energies of all phases in the system existed. The CALPHAD method was utilized to construct such a database. The main contributions are described below:

1. The ternary system Al-La-Mg was optimized for the first time. A good agreement between calculated and experimental results was achieved.
2. A DTA analysis was performed on the Al - 15wt.% La – 15 wt.% Mg and Al - 20wt.% La – 20 wt.% alloys to address an inconsistency between the liquidus temperatures reported in the literature and those resulting from the thermodynamic assessment. This investigation confirmed the liquidus temperatures predicted by our description of the Al-La-Mg system.

3. An approach was proposed to change the sublattice model of a phase after the system is optimized. This method addresses the problem of incompatibility between the models proposed for the same phase in different systems. This approach was successfully employed to make the model of the Laves_C15 and BCC_B2 phases in the La-Mg system compatible with those adopted in other systems.
4. By compiling solidification paths for low and high cooling rates it is demonstrated that it is impossible to fabricate a two-phase material consisting of Al and RMg ductile intermetallic.

For the second part, two series of alloys were prepared by adding varying amount of Ce and La. The effect of these additions on the microstructure and mechanical properties of the alloy was examined in the as-cast and T4 conditions. The following results were achieved:

1. An addition of 0.1 – 0.2 wt. % of lanthanum to the reference alloy showed to have two beneficial effects in the as-cast condition. Firstly, it promotes the formation of Chinese script α-AlFeSi phase at the expense of harmful β platelets. Secondly, the grain size of the alloy uniformly decreased with increase in La content.
2. It was anticipated that Ce and La would demonstrate slightly dissimilar modifying abilities due to existing yet non-crucial differences in their chemical and physical properties. In spite of that expectation, these two rare-earth metals demonstrate disparate modifying potency: while lanthanum suppresses the formation of the β

phase in as-cast alloys and reduces the grain size, cerium additions are totally ineffective in this respect.

3. Ce-containing and La-containing particles were seen in Ce-added and La-added alloys, respectively. EDS examination showed that iron was not a constituent of these phases.
4. Despite favorable changes that La addition had on the as-cast alloy, no improvement in their bendability after thermo-mechanical processing. It was found that the breakdown of intermetallics during rolling and solutionizing processes eliminated the differences between the microstructure of the reference and La-added alloy samples. Furthermore, the dynamic recrystallization accompanying hot rolling and grain growth during solutionizing resulted in the same grain size in all alloys. The similarities of microstructures and grain sizes were reflected in the similar bendability of reference and La-treated alloys

To reveal the mechanism of modification by La addition a thermal analysis experiment was performed. Such analysis would show the sequence of formation of Fe-bearing intermetallics. The effect of La on this sequence would shed light on the modification mechanism of La. The following results were obtained:

1. The solidification paths of the reference and La-containing alloys were deduced from a careful characterization of phases in the cast microstructure. These paths were quite similar except for the formation of $La(Al,Si)_2$ phase in the alloy containing 0.2 wt.% La.

2. Contrary to expectations, the β-AlFeSi phase was not the dominant intermetallic phase in the alloys slowly cooled in this experiment. It is concluded that the β-AlFeSi is a metastable phase formed as a result of higher cooling rates.
3. The established solidification paths did not support a popular theory relying on the suppression of the peritectic reaction to promote the formation of β from α. This reaction did not happen in either reference or La-containing alloys.
4. The formation of $La(Al,Si)_2$ phase in La-treated alloys provoked the idea that it was not the intrinsic ability of La but the consumption of Si by this phase which favored the formation of α-AlFeSi phase in alloys solidified at higher cooling rates. This would explain the inability of Ce to modify the Fe-bearing intermetallics where the Si concentration was high. This hypothesis was proved incorrect since La was able to modify the intermetallics of a high Si containing alloy.

References

Abu Khatwa, M. K., Malakhov, D. V., (2006) CALPHAD, 30, 159:170.

Aldebert, P., Traverse, J. P., (1979) Materials Research Bulletin, 14(3), 303-323.

Allen, C. M., O'Reilly, K. A. Q., Cantor, B., Evans, P. V., (1998) Progress in Materials Science, 43, 89-170.

Andersson, J.-O., Fernández Guillermet, A., Hillert, M., Jansson B., & Sundman, B., (1986) Acta Metallurgica, 34, 437-445.

Anderson, J. -O., Helander, T., Höglund, L., Shi, P., & Sundman, B. (2002) Calphad, 26(2), 273-312.

Ansara, I., Sundman, B., Willemin, P., (1988) Acta Metallurgica, 36(4), 977-982.

Ansara, I., Dupin, N., Lukas, H.L., and Sundman, B., (1997) Journal of Alloys and Compounds, 247, 20-30.

Ansara, I., Chart, T. G., Guillermet, A., Fernández, Hayes, F. H., Kattner, U. R., Pettifor, D. G., Saunders, N., and Zeng, K. (1997), CALPHAD, 21(2), 171-218.

Ansara, I., Dupin, N., Sundman, B., (1988) CALPHAD, 21(4), 535-542.

Ashby, M. F., (1966) Philosophical Magazine, 14, 1157-1178.

Ashtari, P., Tezuka, H., & Sato, T., (2004) Scripta Materialia, 51, 43-46.

Ashtari, P., Tezuka, H., & Sato, T., (2005) Scripta Materialia, 2005, 53, 937-942.

Babout, A., Maire,E., Buffiere, J., and Fougeres, R., (2001) Acta Materialia, 49(11), 2055-2063.

Backerud, L., Krol, E., Tamminen, J., (1986) "Solidification Characteristics of Aluminum alloys Vol 1: Wrought Alloys" SkanAluminum, Sweden.

Bakke, P., Pettersen, K., Westengen, H., (2003) Journal of Materials, 55, 46-51.

Bale, C. W., Chartrand, P., Degterov, S. A., Eriksson, G., Hack, K., Ben Mahfoud, R., Melançon, J., Pelton, A. D., & Petersen, S., (2002) Calphad, 26(2), 189-228.

Barlock, J., Mondolfo, L., (1975) Zeitschrift fur Metallkunde, 66, 605-611.

Bevk, J., Harbison, J. P., & Bell, J. L., (1978) Journal of Applied Physics, 49, 6031-6038.

Birol, Y., (2004) Journal of Materials Processing Technology, 148, 250-258.

Boettinger, W. J., Kattner, U. R., Moon, K.,and Perepezko, J. H. (2007) in "Methods for Phase Diagram Determination", Zhao, J. C. Ed., Elsevier.

Brechet, Y., Embury, J. D., Tao, S., and Luo, L., (1991) Acta Metallurgica et Materialia, 39, 1781-1786.

Brody, H. D., & Flemings, M. C., (1966) Transactions of AIME, 1966, 236, 615-624.

Broek, D., (1973) Engineering Fracture Mechanics, 5(1), 55-56.

Brown, L. M. and Embury, J. D., (1973) Institute of Metals, Monograph and Report Series, 1, 164-169.

Bryant, J.D., (1999) Metallurgical and Materials Transactions A, 30A, 1999-2006.

Cacciamani, G. and Ferro, R. (2001), Calphad, 25(4), 583-597.

Cacciamani, G., Saccone, A., De Negri, S., & Ferro, R. (2002) Journal of Phase Equilibria, 23(1), 38-50.

Cacciamani, G., De Negri, S., Saccone, A., & Ferro, R. (2003) Intermetallics, 11(11-12), 1135-1151.

Caceres, C. H. and Griffiths, J. R., (1996) Acta Materialia, 44, 25-33.

Caddell, R. M., Hosford, W. D., (1993) "Metal Forming: Mechanics and Metallurgy", 2nd ed., Prentice Hall, NJ.

Cao, Z., Sun, D., Du, W., & Zheng, Z., (1990) Aluminum Alloys '90. Second International Conference on Aluminum Alloys-Their Physical and Mechanical Properties, 312-314.

Chen, X. –G., Langlais, J., (2000) Materials Science Forum, 331-337, 215-222.

Chen, S. L., Daniel, S., Zhang, F., Chang, Y. A., Yan, X. Y., Xie, F. Y., Schmid-Fetzer, R., & Oates, W. A., (2002) Calphad, 26(2), 175-188.

Chen, M., Hallstedt, B., and Gauckler L. J., (2003) Journal of Phase Equilibria, 24(3), 212-227.

Clode, M. P., Sheppard, T., (1990) Materials Science and Technology, 6, 755-763.

Clyne, T. W., and Kurz, W., (1981) Metallurgical Transactions A, 12A, 965-971.

Couto, K. B. S., Claves, S. R., Van Geertruyden, W. H., Misiolek, W. Z., Goncalves, M., (2005) Materials Science and Technology, 21, 263:268.

Cox, T. B. and Low, J. R., (1974) Metallurgical Transactions A, 5A, 1457-1470.

Datsko, J., Yang, C.T., (1960) Journal of Engineering for Industry 82, 309-314.

Davies, G., (2003) "Materials for Automobile Bodies" Butterworth-Heinemann, Oxford, UK.

Davies, R. H., Dinsdale, A. T., Gisby, J. A., Robinson, J. A. J., & Martin, S. M., (2002) Calphad, 26(2), 229-271.

Dieter, G. E., (1986) "Mechanical Metallurgy", 3rd edition, McGraw-Hill, New York, p. 374.

Dinsdale, A. T., (1991) Calphad, 15, 317-425.

Dons, A. L., (1984) Zeitschrift fur Metallkunde, 75, 170-174.

Dons, A. L., (1985) Zeitschrift fur Metallkunde, 76, 609-612.

Duppin, N., Ansara, I., (1999) Zeitschrift fur Metallkunde, 90, 76-85.

Embury, J. D., Fisher, R. M., (1966) Acta Metallurgica, 14, 147-159.

Embury, J. D. & Duncan, J. L., (1981) Annual Review of Materials Science, 11, 505-521.

Engler, O. & Hirsch, J., (2002) Materials science & engineering A, A336, 249-262.

Fabrichnaya, O. B., Lukas, H. L., Effenberg, G., & Aldinger, F. (2003) Intermetallics, 11(11-12), 1183-1188.

Faleskog J. & Shih, C. F., (1997) Journal of the Mechanics and Physics of Solids, 45(1), 21-25.

Ferro,R., Cacciamani,G., (2002) CALPHAD 26(3) 439-458.

Fu, H., Xiao, Q., Li, Y., (2005) Materials science & engineering A, A395, 281:287.

Gammage,J. J., Wilkinson, D. S., Brechet, Y., Embury, J. D., (2004) Acta Materialia, 52, 5255-5263.

Gammage,J. J., Wilkinson, D. S., Embury, J. D., and Maire, E., (2005) Philosophical Magazine, 85(26–27), 11–21, 3191–3206.

Glover, G., Duncan, J. L., & Embury, J. D., (1977) Metals Technology, 4, 153-159.

Griger, A., Stefaniay, S., Lendvai, A., & Turmezey, T., (1989) Aluminium, 10, 1049-1056.

Griger, A., Stefaniay, S., (1996) Journal of Materials Science, 31, 6645-6652.

Grobner, J, Schmid-Fetzer, R, Pisch, A, Cacciamani, G, Riani, P, Ferro, R. (1999) Zeitschrift fur Metallkunde, 90, 872–880.

Grobner, J., Kevorkov, D., and Schmid-Fetzer, R. (2002) Intermetallics, 10(5), 415-422.

Grundy, A. N., Hallstedt, B., and Gauckler, L. J., (2003) Journal of Phase Equilibria, 24(1), 21-39.

Gschneidner, K. G., Russell, A., Pecharsky, A., Morris, J., Zhang, Z., Lograsso, T., Hsu, D., Lo, C. H. C., Ye, Y., & Slager, A., (2003) Nature Materials, 2(9), 587-590.

Gulliver, G.H., (1913) The Journal of the Institute of Metals, 9, 120-157.

Guo, C. and Du, Z. (2004), Journal of Alloys and Compounds, 385(1-2), 109-113.

Gupta, A.K., Marois, P.H., Lloyd, D.J., (1996) Materials Characterization, 37(2-3), 61–80.

Gurland, J., Plateau, J., (1963) ASM Transactions, 56, 442.

Hallstedt, B., Balitchev, E., Shimaharm, H., and Neuschutz, D., (2006) ISIJ International, 46(12), 1852–1857.

Hansen, V., Hauback, B., Sundberg, M., Rumming, C., Gjùnnes, J., (1998) Acta Crystallographica B, B54 351-357.

Hecker, S. S., (1975) Journal of Engineering Materials and Technology, 97, 66-73.

Hertzberg, R. W., (1989) "Deformation and Fracture Mechanics of Engineering Materials", 3rd edition, John Wiley & Sons Inc., New York, pp. 392-396.

Hillert, M., and Staffanson, L. –I., Acta Chimica Scandinavica, 24, 3618-3626.

Hillert, M., Jansson, B., Sundman, B., & Agren, J., (1985) Metallurgical Transactions A, 16A, 261-266.

Hillert, M., (1999) in "Lectures on the Theory of Phase Transformations", Aaronson H. I., ed. TMS, Warrendale, 1-33.

Hillert, M., Hoglund, L., and Schalin, M., (1999) Metallurgical and Materials Transactions A, 30A, 1635-1641.

Hillert, M., (2001) Journal of Alloys and Compounds, 320, 161-176.

Hsu, C., O'Reilly, K. A. Q., Cantor, B., Hamerton, R., (2001) Materials Science and Engineering A, A304–306, 119–124.

Jansson, B., Schalin, M., & Sundman, B., (1993) Journal of Phase Equilibria, 14, 557-562.

Jansson, B., in Evaluation of parameters in thermochemical models using different types of experimental data simultaneously, TRITA-MAC-0234, Royal institute of technology, Sweden, 1984.

Joubert, J. -M., (2008) Progress in Materials Science, 53, 528-583.

Kang, J., Wilkinson, D. S., Malakhov, D. V., Halim, H., Jain, M., Embury, J. D., & Mishra, R. K., (2007) Materials Science and Engineering A, A456, 85–92.

Kelly, A., Tyson, W. R., (1965) in "High strength materials", Zackay, V. F., ed., Wiley, New York, 578-602.

Khalifa, W., Samuel, F. H., & Gruzlaski, J. E., (2003) Metallurgical and Materials Transactions A, 34A, 807-825.

Kohler, F., (1960) Monatshefte für Chemie, 91(4), 738-740.

Kral, M. V., (2005) Materials Letters, 59(18), 2271-2276.

Kral, M. V., Nakashima, P. N. H., and Mitchell, D. R. G. (2006) Metallurgical and Materials Transactions A, 37A, 1987-1997.

Kuemmerle, E. A., & Heger, G., (1999) Journal of Solid State Chemistry, 147, 485-500.

Kumar, K. C. H., Ansara, I., Wollants, P., (1998) CALPHAD, 22, 323-334.

Langsrud, Y., (1990) Key Engineering materials, 44-45, 95-116.

Larouche, D., (2007) CALPHAD, 31, 490–504.

Lawrence, C. M., Wu, C. M. L., Yu, D. Q., Law, C. M. T., Wang, L., (2002) Journal of Electronic Materials, 3, 921-927.

Liang, P., Su, H. L., Donnadieu, P., Harmelin, M. G., Quivy, A., Ochin, P., Effenberg, G., Seifert, H. J., Lukas, H. L., and Aldinger, F. (1998), Zeitschrift fur Metallkunde, 89(8), 536-540.

Lievers, W. B., Pilkey, A. K., & Lloyd, D. J., (2003) Materials Science & Engineering A, A361, 312-320.

Lilholt, H., (1993) in "Mechanical properties of metallic composites", Ochiai, H., ed, Marcel Decker Inc., New York, 389-471.

Liu, Z., Chang, Y. A. (1999) Metallurgical and Materials Transactions A, 30A, 1081-1095.

Llorca, J., Martin, A., Ruiz, J., and Elices, M., (1993) Metallurgical Transactions A, 24A(7), 1577-1588.

Lukas, H. L., Henig, E. T., & Zimmermann, B., (1977) CALPHAD, 1(3), 225-236.

Lukas, H.L., & Fries, S.G., (1992) Journal of Phase Equilibria, 13(5), 532-541.

Meredith, W. M., Worth, J., Hamerton, R. J., (2002) Materials Science Forum, 396-402, 107-112.

Maire,E., Verdu, C., Lormand G., and Buffiere, J., (1995) Materials Science and Engineering A, A199(1-2), 135-144.

McClintock, F. A., (1968) in "Ductility", American Society for Metals, Metals Park, 255-277.

Miller, W. S., Zhuang, L., Bottema, J., Wittebrood, A. J., De Smet, P., Haszler, A., & Vieregge, A., (2000) Materials Science & Engineering A, A280, 37-49.

Morris, L. R., Iricibar, R., Embury, J. D., and Duncan, J. L., (1982) Aluminum Transformation Technology and Applications, 549-582.

Morris, D. G., Chao, J., Garcia, Oca, C., Munoz-Morris, M. A., (2003) Materials Science and Engineering A, A339, 232-240.

Morris, J. R., Ye, Y., Lee, Y., Harmon, B. N., Gschneidner, K. A., & Russell, A. M., (2004) Acta Materialia, 52, 4849-4857.

Muggianu, Y. M., Gambino, M., Bros J. P., (1975) Journal of Chemical Physics, 72(1), 83-88.

Mulazimoglu, M. H., Zaluska, A., Gruzleski, J. E., Paray, F., (1996) Metallurgical and Materials Transactions A, 27A, 929-936.

Muravyova, A. O., (1971) Vestn. L'viv Univ. Ser. Khim., 12, 8-9.

Muravyova, A. O., (1972) Atoreferat Dis. Kand. Khim. Nuak. Lvov, 1-18.

Muravyova, A. O., Zarechnyuk, O. S., & Gladyshevskij, E. I., (1972) Visn. L'viv Univ. Ser. Khim., 13, 14-16.

Murty, B. S., Kori, S. A., and Chakraborty, M., (2002) International Materials Reviews, 47(1), 3-29.

Musulin, I., Celliers, O. C., (1990) Light Metals, 951-954.

Nakano, J., Malakhov, D. V., Purdy, G. R., (2005) CALPHAD, 29(4), 276-288.

Odinaev, K. H. O., Ganiev, I. N., Kinzhibalo, V. V., and Tyvanchuk, A. T. (1988) Izvestiya Vysshikh Uchebnykh Zavedenii, Tsvetnaya Metallurgia, (2), 81-85.

Odinaev, K. & Ganiev, I. N., Vakhobov, A. V., (1991), Russian Metallurgy, (4), 200-203.

Odinaev, K. & Ganiev, I. N., (1995), Russian Metallurgy, (2), 146-150.

Odinaev, K. & Ganiev, I. N., Ikromov, A. Z.,(1996), Russian Metallurgy, (3), 122-125.

Onurlu, S., Tekin, A., (1994) Journal of Materials Science, 29, 1652-1655.

Paray, F., Kulunk, B., Gruzleski, J., (1996) Materials Science and Technology, 12, 315-322.

Parker, B. A., (1989) in "Aluminum alloys - contemprary research and applications", Vasudevan, A. K., and Doherty, R. D., Eds., Academic press Inc., 539-562.

Pekguleryuz, M. O., Kaya, A. A., (2003) Advanced Engineering Materials, 5, 866-878.

Poruks, P., Wilkinson,,D. S., and Embury, J. D., (1998) Microstructural Sciences, 26, 491-496.

Purdy, G. R., Malakhov, D. V., Zurob, H., (2004) in "Phase Diagram in Materials Science" Velikanova, T. Y., ed., Materials Science International, Stuttgart, 20-41.

Quested, T. E., (2004) Materials Science and Technology, 20, 1357-1369.

Raman, A., Steinfink, H., (1967) Inorganic chemistry, 6(10), 1789-1791.

Ravi, M., Pillai, U. T. S., Pai, B. C., Damodaran, A. D., & Dwarakadasa, E. S., (2002) Metallurgical and Materials Transactions A, 33A, 391-400.

Redlich, O. & Kister, A.T., (1948) Industrial and Engineering Chemistry, 40, 345-348.

Rogl, P., (1988) in "Ternary alloys: a comprehensive compendium of evaluated constitutional data and phase diagrams" Petzow, G., Effenberg, G., Eds., Weinheim, New York.

Russell, A. M., (2003) Advanced Engineering Materials, 5(9), 629-639.

Russell, A. M., Zhang, Z., Lograsso, T. A., Lo, C. C. H., Pecharsky, A. O., Morris, J. R., Ye, Y., Gschneidner Jr., K. A., & Slager, A. J., (2004) Acta Materialia, 52, 4033-4040.

Russell, A. M., Zhang, Z., Gschneidner, K. A., Lograsso, T. A., Pecharsky, A. O., Slager, A. J., & Kesse, D. C., (2005) Intermetallics, 13, 565-571.

Salazar, M., Perez, R., Rosas, G., (2003) Materials Science Forum, 426-432, 1837:1842.

Samuel, F. H., Samuel, A. M., Doty, H. W., Valtierra, S., (2001) Metallurgical and Materials Transactions A, 32A, 2061-2075.

Sarkar, J., Kutty, T. R. G., Wilkinson, D. S., Embury, J. D., & Lloyd, D. J., (2000) Materials Science Forum, 331-337, 583-588.

Sarkar, J., Kutty, T. R. G., Conlon, K. T., Wilkinson, D. S., Embury, J. D., & Lloyd, D. (2001) Materials Science and Engineering A, A316, 52–59.

Saunders, N. & Miodownik, A.P., (1998) "CALPHAD, calculation of phase diagrams: a comprehensive guide", Pergamon Press, New York.

Saunders, N., (1996) CALPHAD, 20(4), 491-499.

Scheil, E., (1942) Zeitschrift fur Metallkunde, 34, 70-72.

Sha, G., O'Reilly, K. A. Q., Cantor, B., (2006) Materials Science Forum, 519-521, 1721-1726.

Shabestari, S. G., Gruzleski, J. E., (1995) Transactions of the American Foundrymen's Society, 26, 285-293.

Sinclair, C. W., Embury, J. D., & Weatherly, G. C. (1999). Materials Science & Engineering A, A272, 90-98.

Sinclair, C. W., (2001) Ph.D. Thesis, McMaster University, Canada.

Skjerpe, P., (1987) Metallurgical Transactions A, 18A, 189-200.

Spencer, K., Corbin, S. F., & Lloyd, D. J., (2002) Materials Science and Engineering A, A325, 394-404.

Spitzig, W. A., Krotz, P. D., (1988) Acta Metallurgica, 36, 1709-1715.

Sun, C. Y., Mondolfo, L. F., (1967) Journal of Institute of Metals, 95, 384.

Sundman, B., & Ågren, J., (1981) Journal of Physics and Chemistry of Solids, 42(4), 297-301.

Sundman, B., (1991), Thermo-Calc newsletter, 12, Stockholm, Sweden.

Suzuki, K., Kumai, S., Saito, Y., and Haga, T., (2005) Materials Transactions, 46(12), 2602-2608.

Tanaka, K., Mori, T., and Nakamura, T., (1970) Philosophical Magazine, 21, 267-279.

Tanihata, H., Sugawara, T., Matsuda, K., and Ikeno, S., (1999) Journal of Materials Science, 34, 1205-1210.

Tancret, F., (2007) Computational Materials Science, 41, 13–19.

Toop, G. W., (1965) Transactions of the Metallurgical Society of American Institute of Mining Engineers, 233(5), 850-855.

Turmezey, T., Stefaniay, S., & Griger, A., (1990) Key Engineering materials, 44-45, 57-68.

Villars, P. Calvert, L. D., (1991) Pearson's Handbook of Crystallographic Data for Intermetallic Phases, ASM international, Ohio.

Walter, C., Hallstedta, B., and Warnken, N., (2005) Materials Science and Engineering A, A397, 385–390

Weck, A., Wilkinson, D. S., and Maire, E., (2008) Materials Science & Engineering A, A488(1-2), 435-445

Westengen, H., (1982) Zeitschrift fur Metallkunde, 73, 360-368.

Wollmershauser, J. A., Kabra, S., Agnew, S. R. (2009) Acta Materialia 57(1) 213-223.

Xia, Z., Chen, Z., Shi, A., Mu, N., Sun, N., (2002) Journal of Electronic Materials, 31, 564-567.

Xie, S., Gschneidner, K. A., Russell, A. M. (2008) Scripta Materialia, 59(8), 810-813.

Yan, X., (2007) Mater of Science Thesis, McMaster University, Canada.

Ye, B. J., Loper, C. R., Lu, D. Y., Kang, C. S., (1985) Transactions of the American Foundrymen's Society, 93, 533-544.

Yin, F., Su, X., Li, Z., Huang, M., and Shi, Y. (2000), Journal of Alloys and Compounds, 302(1-2), 169-172.

Zajac, S., Hutchinson, B., Johansson, A., Gullman, L. O., (1994) Materials Science and Technology, 10, 323-333.

Zakharov, A. M., Gul'din, I. T., Arnol'd, A. A., Matsenko, Yu. A., (1989) Russian Metallurgy, 4, 209-213

Zhang, Z., Russell, A. M., Biner, S. B., Gschneidner, K. A., Lo, C. C. H., (2005) Intermetallics, 13(5), 559-564.

Zheng, C., Xing, Y., Qian, J., and Ye, Y. (1983), Acta Metallurgica Sinica, 19(6), 515-520.

Zhou, S. H. and Napolitano, R. E. (2006), Acta Materialia, 54(3), 831-840

APPENDIX I

Al-Mg system

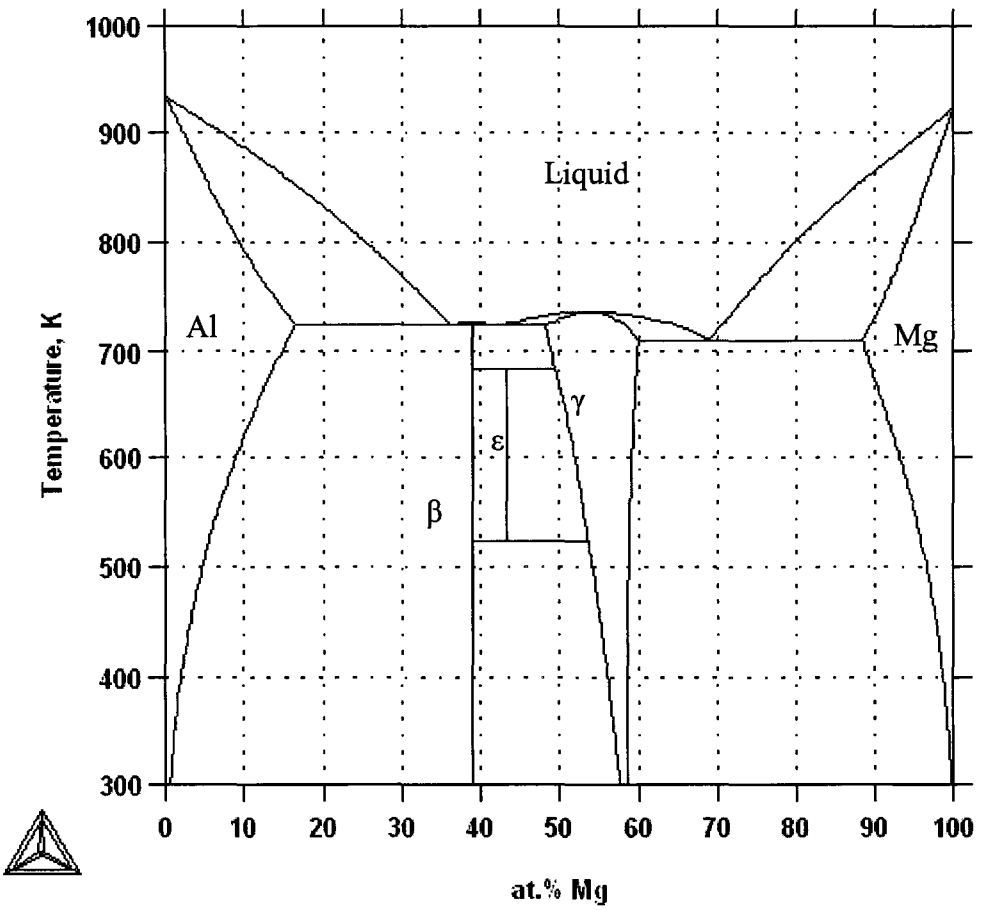

Figure I-1 Equilibrium phase diagram of Al-Mg calculated using optimized data of Liang *et al.* [1998]

Table I-1 Crystal structure and models of phases in the Al-Mg system

Phase	Pearson symbol	Prototype	Space group	Model	Name in the database
Al	cF4	Cu	$Fm\bar{3}m$	$(Al,Mg)_1$	FCC_A1
Mg	hP2	Mg	$P6_3/mmc$	$(Al,Mg)_1$	HCP_A3
β	cF112	Cd_2Na	$Fd\bar{3}m$	$(Al)_{140}(Mg)_{89}$	AL140MG89
ε	hR53	$Co_5Cr_2Mo_3$	R3	$(Al)_{30}(Mg)_{23}$	AL30MG23
γ	cI58	αMn	$I\bar{4}3m$	$(Mg)_{10}(Al,Mg)_{24}(Al,Mg)_{24}$	AL12MG17

Table I-2 Invariant reactions in the Al-Mg system

Reaction	T (K)	Compositions (at.% Mg)		
Liquid → γ	736.6	53.8	53.8	
Liquid → β	724.8	38.9	38.9	
Liquid → Al + β	723.6	36.2	16.6	38.9
Liquid → β + γ	722.7	42.4	38.9	48
Liquid → γ + Mg	709.4	69	60.1	88.4
γ + β → ε	682.9	49.4	38.9	43.4
ε → γ + β	523.2	43.4	53.6	38.9

AL-La

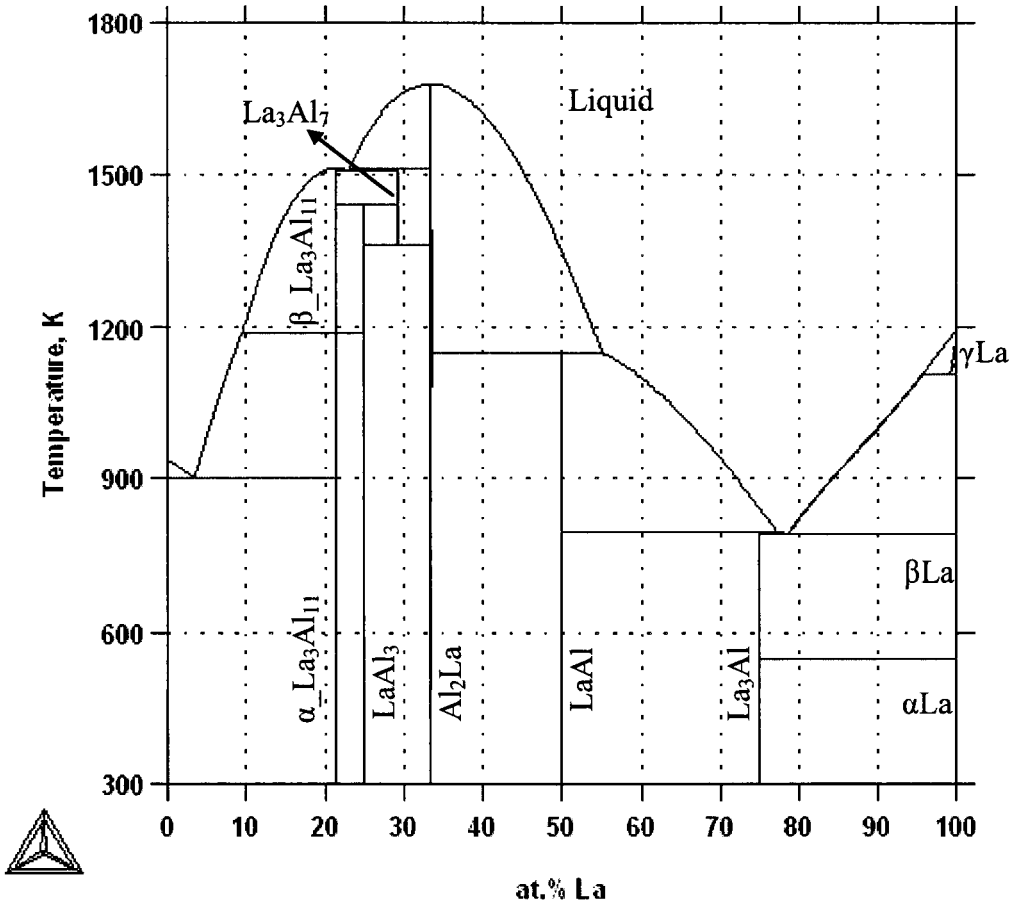

Figure I-2 Equilibrium phase diagram of Al-Mg calculated using optimized data of Zhou and Napolitano [2006]

Table I-3 Crystal structure and models of phases in the Al-La system

Phase	Pearson symbol	Prototype	Space group	Model	Name in the database
Al & βLa	cF4	Cu	$Fm\bar{3}m$	$(Al,La)_1$	FCC_A1
αLa	hP4	αLa	$P6_3/mmc$	$(Al,La)_1$	DHCP
γLa	cI2	W	$Im\bar{3}m$	$(Al,La)_1$	BCC_A2
α_La_3Al_{11}	oI28	α_La_3Al_{11}	Immm	$(La)_3(Al)_{11}$	A_R3AL11
β_La_3Al_{11}	tI10	Al_4Ba	I_4/mmm	$(Al,La)_3(Al,La)_{11}$	B_R3AL11
La_3Al & $LaAl_3$	hP8	Ni_3Sn	$P6_3/mmc$	$(Al,La)_3(Al,La)_1$	LA3AL
La_3Al_7	hP3	AlB_2	$P6_3/mmc$	$(La)_{0.707}(Al)_{0.293}$	AL7LA3
Al_2La	cF24	Cu_2Mg	$Fd\bar{3}m$	$(Al,La)_2(Al,La)_1$	LAVES_C15
LaAl	oC16	AlCe	Cmc2 or Cmcm	$(La)_1(Al)_1$	LAAL

Table I-4 Invariant reactions in the Al-La system

Reaction	T (K)	Compositions (at.% La)		
Liquid → Al_2La	1678.3	33.3	33.3	–
Liquid → β_La_3Al_{11}	1513.2	21.4	21.4	–
Liquid + Al_2La → La_3Al_7	1512.8	23.5	33.3	29.3
Liquid → β_La_3Al_{11} + La_3Al_7	1505.7	23.2	21.4	29.3
β_La_3Al_{11} + La_3Al_7 → $LaAl_3$	1442.4	21.4	29.3	25
La_3Al_7 → $LaAl_3$ + Al_2La	1363.8	29.3	25	33.3
β_La_3Al_{11} → α_La_3Al_{11}	1187.9	21.4	21.4	-
Liquid + Al_2La → LaAl	1146	54.4	33.6	50
γLa → Liquid + βLa	1105.2	95.6	99.2	100
Liquid → βLa + α_La_3Al_{11}	901.1	3.5	100	21.4
Liquid + LaAl → La_3Al	795.5	76.5	50	75
Liquid + La_3Al → βLa	794.5	77.2	75	100
βLa + La_3Al → αLa	550	100	75	100

La-Mg

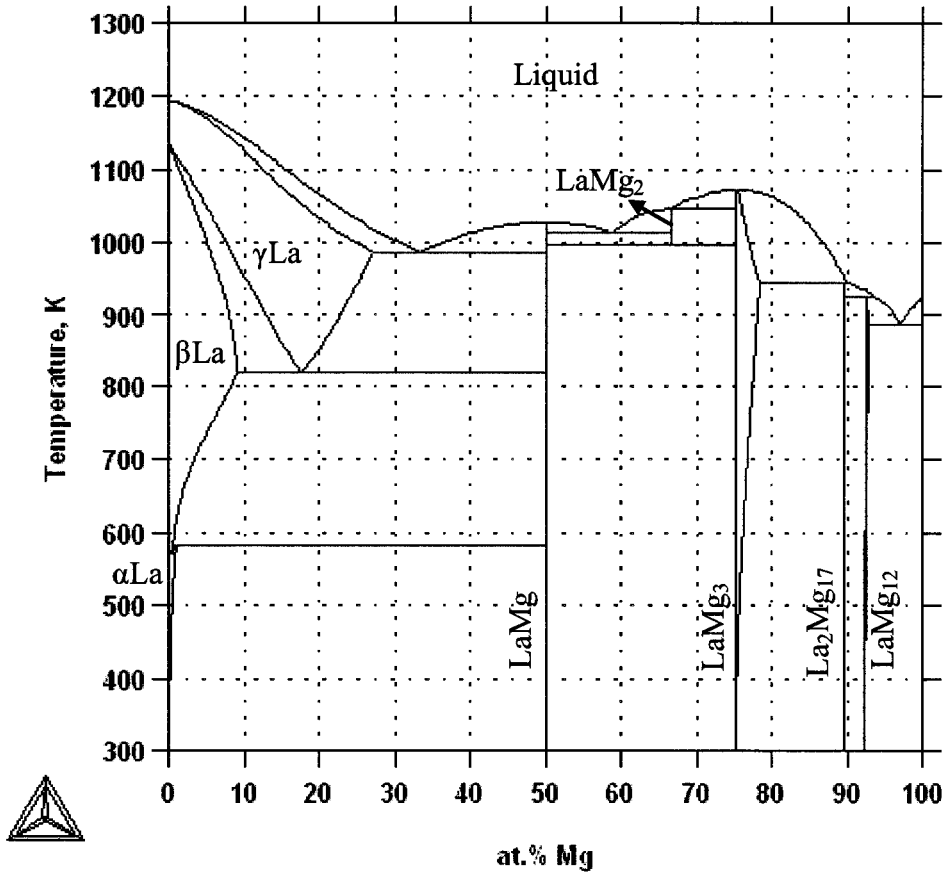

Figure I-3 Equilibrium phase diagram of Al-Mg calculated using optimized data of Guo *et al.* [2004]

Table I-5 Crystal structure and models of phases in the La-Mg system

Phase	Pearson symbol	Prototype	Space group	Model	Name in the database
αLa	hP4	αLa	$P6_3/mmc$	$(La,Mg)_1$	DHCP
βLa	cF4	Cu	$Fm\bar{3}m$	$(La,Mg)_1$	FCC_A1
γLa	cI2	W	$Im\bar{3}m$	$(La,Mg)_1$	BCC_A2
Mg	hP2	Mg	$P6_3/mmc$	$(La,Mg)_1$	HCP_A3
LaMg	cP2	CsCl	$Pm\bar{3}m$	$(La)_1(Mg)_1$	BCC_B2
$LaMg_2$	cF24	Cu_2Mg	$Fd\bar{3}m$	$(La)_1(Mg)_2$	LAVES_C15
$LaMg_3$	cF16	BiF_3	$Fm\bar{3}m$	$(La,Mg)_1(Mg)_3$	LAMG3
La_2Mg_{17}	hP38	Th_2Ni_{17}	$P6_3/mmc$	$(La)_2(Mg)_{17}$	LA2MG17
$LaMg_{12}$	oI338	$CeMg_{12}$	Immm	$(La,Mg)_1(La,Mg)_{12}$	LAMG12

Table I-6 Invariant reactions in the La-Mg system

Reaction	T (K)	Compositions (at.% Mg)		
Liquid → γLa +LaMg	988	33.2	27.1	50
γLa → LaMg + βLa	819	17.6	50	9.1
βLa + LaMg → αLa	583	0.55	50	0.96
Liquid → LaMg	1028	50	50	–
Liquid → LaMg + $LaMg_2$	1014	58.7	50	66.6
Liquid + $LaMg_3$ → $LaMg_2$	1048	66.5	75.1	66.6
$LaMg_2$ → LaMg + $LaMg_3$	998	66.6	50	75
Liquid → $LaMg_3$	1071	75.3	75.3	–
Liquid + $LaMg_3$ → La_2Mg_{17}	945	89.9	78.4	89.5
Liquid + La_2Mg_{17} → $LaMg_{12}$	923	93.5	89.5	92.4
Liquid → Mg + $LaMg_{12}$	886	96.9	99.9	92.7

APPENDIX II

Image analysis technique is employed in this investigation to quantify the area percent and aspect ratio of constituent intermetallic particles. This analysis is performed using the free UTHSCSA ImageTool program (developed at the University of Texas Health Science Center at San Antonio, Texas) which distinguishes the intermetallic particles from the Al matrix depending on their gray level.

The analysis starts with taking several images in the backscattered mode of SEM. The mechanism of contrast formation using backscattered electrons is based on the average atomic number of the region under the electron beam, the higher the average atomic number the higher the brightness. The intermetallic particles are seen brighter than Al matrix in backscattered images due to the presence of heavy Fe, Ce and La elements. Examples of these images are shown in Figure 3-14a-d and Figure 3-15a-d. Each image is imported to the software interface after the information bar at the bottom of it is discarded. An 8-bit gray scale image is then produced by the software. In this image a level of gray is assigned to each pixel. The levels are positive integer values which vary from 0 (black) to 255 (white).

An important step in an image analysis investigation is thresholding which refers to the process of choosing a range of gray levels represented by the objects of interest.

Finding the right threshold is not an easy task. Different types of particles show different gray level. Even if all particles are of the same type, different gray level results from the

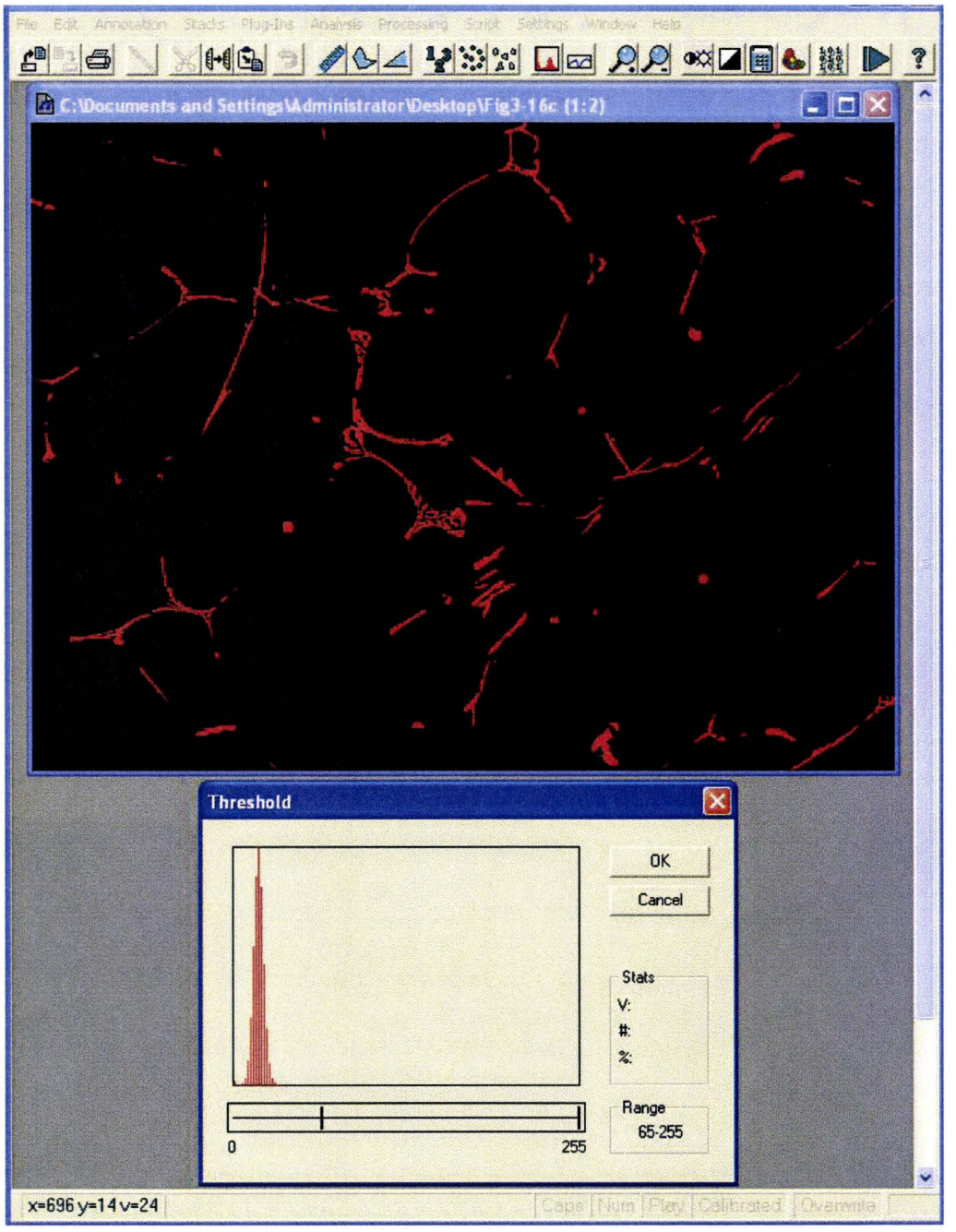

Figure II-1 Thresholding

fact that the particles are cut at different thicknesses by the metallograohic surface. The gray level of particles also depends on the conditions at which the SEM is set and the picture is captured, and hence, it varies from image to image. A manual thresholding is employed in the present study. The software allows the user to choose a range of gray levels and it simultaneously highlights the areas of the picture that fall into the chosen range (Figure II-1).

To find a proper threshold, the range is varied and the changes in the highlighted regions were followed visually until a reasonable match between the highlighted regions and the intermetallic particles is found. It cannot be denied that such procedure is subjective. To reduce this effect, a scheme is designed and followed. The scheme is constituted of thresholding all images and recording the range. Once all the images are examined, the operator would start thresholding once again from the first image without remembering the range found in previous tryout. Such repetition is done three times and the average of three thresholds of an image is chosen for the quantification of intermetallics in that image. The acquired range of gray levels represented by all intermetallic particles is typically between 55 to 65 and 255 for different images.

Ce and La containing intermetallics are characterized by a higher brightness than the Fe-bearing intermetallics which makes it easy to recognize them by choosing a range which starts with a higher gray level. The same practice mentioned earlier is carried out to find the proper range for these particles. Different morphologies of Fe-bearing intermetallics cannot be differentiated by thresholding since they are characterized by

similar range of gray levels. Fe/Si ratio can be used to distinguish these particles, however, it is impractical to characterize all particles in an image by EDS. As a practical way, the peculiar shape of Chinese script particles can be employed to quantify their fraction. An experienced person can reliably decide whether a particle is Chinese script only by examining the image visually. The particles with faceted interfaces and elongated shape are painted black using an image processing software and the remaining particles are quantified by the image analysis technique. This procedure is adopted in the present investigation. Figure II-2 shows the same SEM micrograph as Figure 3-15c with plate-like particles blackened out. The same threshold set previously for characterizing all intermetallic particles is then used to measure the area percent of Chinese script particles.

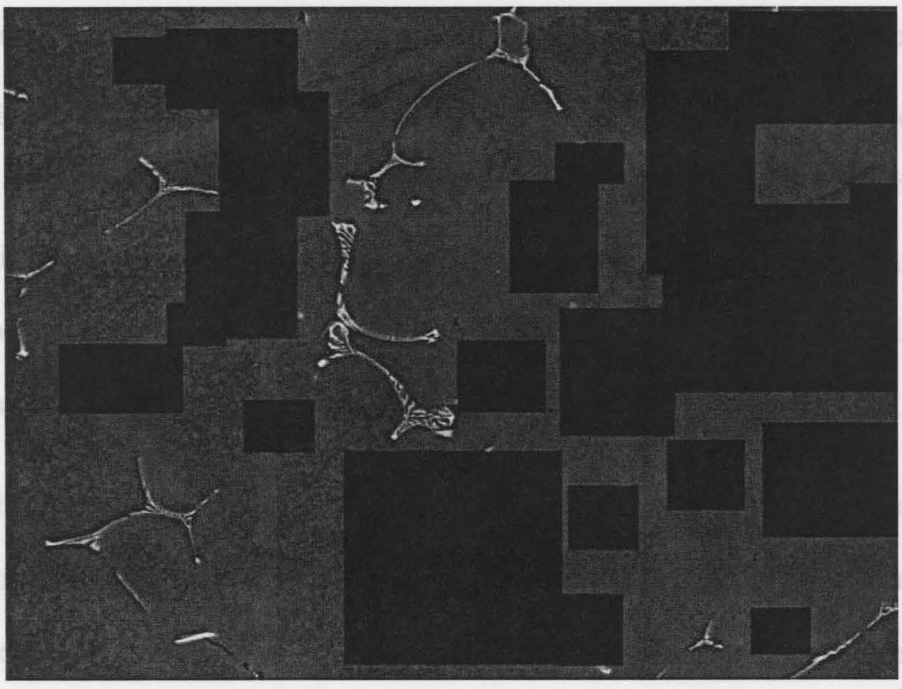

Figure II-2 The same image as Figure 3-15c where elongated particles are masked manually in order to estimate the area % of Chinese script particles

The regions highlighted by the chosen threshold (*i. e.* intermetallic particles) are analyzed by the software and such information as area, length, width, etc. for each particle is extracted. As an example, part of the data obtained by analyzing all intermetallic particles in Figure 3-15c is represented in Table II-1. It is seen that the software recognizes several objects with very small areas. It is apparent that objects such as # 28 and # 29 with areas equal to one pixel×pixel are not intermetallic particles. A criterion is needed to decide what objects are in fact intermetallic particles. This criterion is chosen based on the smallest particle discernable in the image. An examination of several small particles showed that they are at least 1 μm (4 pixels) long. Based on these observations, objects with axis lengths less than 4 pixels are disregarded in the quantification of intermetallic particles.

The area percent of intermetallic particles is calculated by dividing the sum of areas of objects by the area of the image. The "elongation" column in Table II-1 represents the aspect ratio of particles. Since it is only meaningful to define an aspect ratio for elongated particles, the Chinese script particles were masked by black color in the same manner explained above prior to performing aspect ratio measurements. The particles' area percent and aspect ratio are measured by averaging the extracted data from all images of an alloy. The student's t-distribution is used to find the population standard deviation of the calculated averages.

Table II-1 An example of the results of image analysis

Object	Area (Pixel×Pixel)	Perimeter	Major Axis Length (Pixel)	Minor Axis Length (Pixel)	Elongation
#1	27	28.04	13.45	1	13.45
#2	455	262.63	117.35	7.21	16.27
#3	20	23.14	9.9	1.41	7
#4	824	207.69	56.09	27.46	2.04
#5	1	4	1.41	1.41	1
#6	1	4	1.41	1.41	1
#7	1	4	1.41	1.41	1
#8	3	4.41	1.41	1.41	1
#9	1	4	1.41	1.41	1
#10	80	55.7	23.02	4.47	5.15
#11	48	27.9	11.18	5.1	2.19
#12	297	118.67	45.88	8.25	5.56
#13	172	111.98	35.36	12.17	2.91
#14	1	4	1.41	1.41	1
#15	19	15.66	4.47	3.61	1.24
#16	402	168.84	61	8.25	7.4
#17	81	52.21	17.2	5	3.44
#18	94	41.63	15.13	7.07	2.14
#19	340	204.92	74.33	14.32	5.19
#20	1	4	1.41	1.41	1
#21	1	4	1.41	1.41	1
#22	1	4	1.41	1.41	1
#23	4	4.83	2.24	1	2.24
#24	154	137.17	61.22	3.61	16.98
#25	5	9.66	2	2	1
#26	2	2	1	0	1
#27	2	2	1	0	1
#28	1	4	1.41	1.41	1
#29	1	4	1.41	1.41	1
#30	2	2	1	0	1

Before closing this section two points must be made on analyzing images taken in backscattered mode. First, the Mg_2Si particles cannot be quantified using this method. The average atomic number of Mg_2Si compound is 12.66 slightly lesser than that of Al which is 13. As a result, these particles are seen darker than the Al matrix and very similar to voids and porosity sites. Moreover, these particles are not characterized by a distinctive shape which distinguishes them from voids. For these reasons Mg_2Si particles are not accounted for in the present investigation.

Second, an image analysis of backscattered micrographs results in an overestimation of the area percent of intermetallics. This is because the signal recorded in such micrographs does not come exclusively from the surface but a finite volume near the surface. Depending on the material under investigation and the SEM settings, the backscattered signal can be detected from up to one micrometer below the surface. If for example a configuration shown in Figure II-3 is considered, and if it is supposed that the backscattered electrons are able to escape from depth t of the sample, then, the area of the circular object seen in the backscattered image ($\pi D^2/4$) will be greater than the area of the circle cut by the surface of the specimen ($\pi d^2/4$).

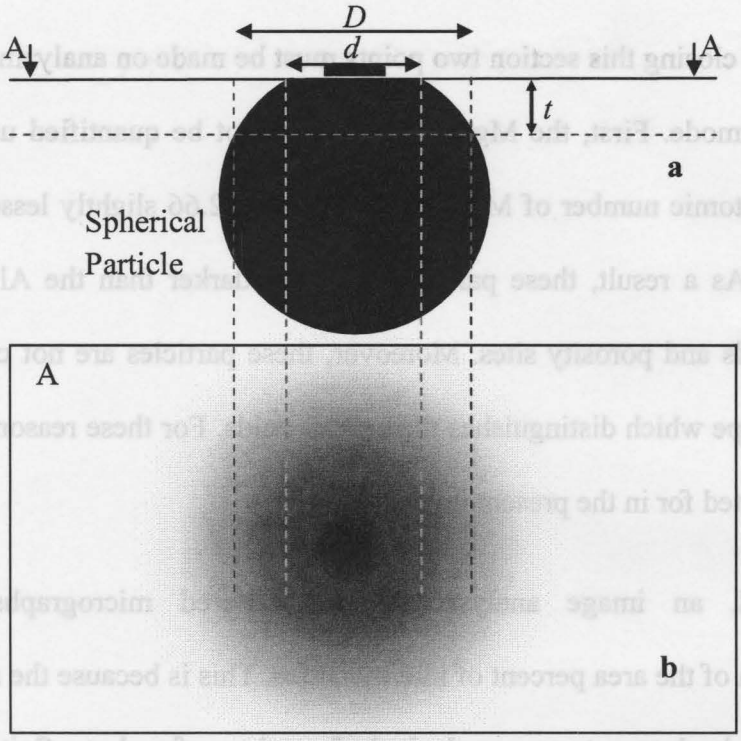

Figure II-3 Schematic representation of a) a particle under electron beam in SEM and b) its image in a backscattered micrograph

APPENDIX III

The intercept procedure is used to measure the average grain size of the alloy samples in the as-cast and T4 conditions. Two optical micrographs were taken for each sample in the lowest possible magnification using ZEISS microscope under polarized light. The two pictures together were covering more than 70 percent of the area of metallographically prepared as-cast samples and about 100 percent of the samples in T4 condition.

As-cast samples were consisted of equiaxed grains. For these samples, a line pattern recommended by the ASTM standard (Figure III-1) was drawn on the images and the number of times that a line intercepted by grain boundaries was counted manually. The length of the line was divided by the number of intercept and the result was considered as the grain size. The average grain size of an alloy is reported as the mean of the eight grain sizes measured for each sample. The standard deviation of the average is calculated using student's t-distribution.

A distinctive non-equiaxed grain structure is observed in samples in T4 condition as a result of the hot rolling step. An example of these structures is seen in Figure III-2. This image shows the transverse plane (perpendicular to the rolling direction) of the specimen which coincides with the same plane examined in the measurement of grain

sizes of as-cast samples. It is clearly seen that the grains are compressed in vertical direction (t(0°)) and elongated in the horizontal direction (t(90°)). For such structures, a line pattern similar to Figure III-1 must not be used since it undermines the anisotropy of the grain size. A meaningful practice for these structures is to make separate grain size measurements along parallel lines that coincide with the two principle directions of the sample. The pattern utilized for T4 samples consisted of four 5 mm horizontal lines and four 2.5 mm vertical lines distributed evenly through the width and length of the image respectively.

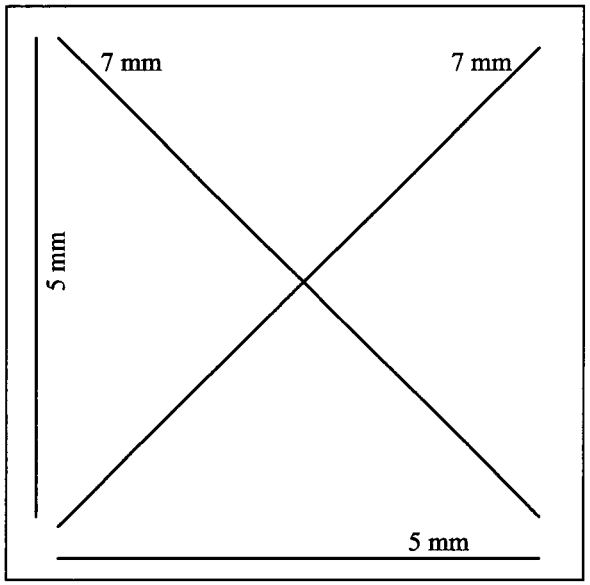

Figure III-1 The line pattern used to estimate grain size of as-cast alloys

Figure III-2 Grain structure of the C2 alloy sample in T4 condition

The intercept method is also employed to measure the secondary dendrite arm spacing (SDAS) of samples investigated by thermal analysis technique. The dendritic structure of the specimens was revealed by etching the samples with an aqueous solution containing 0.5 % concentrated hydrofluoric acid for several minutes. The HF attacks the Al dendrite while intermetallic particles at the interdendritic spaces remain intact and become highlighted. An example of images taken for SDAS measurement is shown in Figure III-3. Each picture is searched for locations that resemble dendrite branches. A region containing n consecutive secondary arms is considered and a line is drawn from the center of the first arm to the center of the last. The length of the line is divided by (n-1) to find the value of SDAS. Such a measurement was carried out at least ten times for each sample.

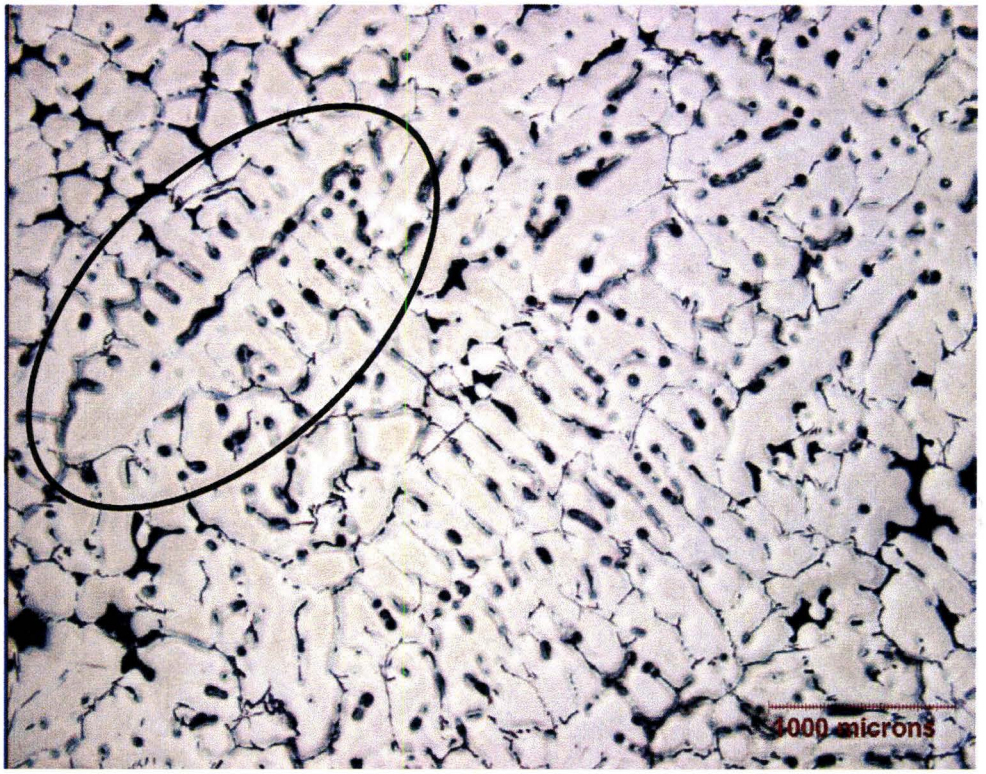

Figure III-3 Dendritic structure of an alloy containing 0.2 wt.% La solidified in a clay crucible